Manipulation of Dirac Points in Graphene Superlattices

A thesis presented by

Shahd Abdulrahman A Alfadhli

to
The Department of Physics
in partial fulfilment of the requirements for the degree of
Doctor of Philosophy
in the subject of

Physics

Loughborough University

Loughborough, United Kingdom

February 2019

Abstract

This study theoretically investigates the changes in the energy spectrum of the graphene monolayer subjected to different periodic potential to allow manipulation of the energy spectrum. Floquet theory and the resonance approximation are used to analyse the energy spectrum. Thus, we reviewed the application of single laser potential; linearly polarised and circularly polarised and concluded that the gap opening in the spectrum is determined by the polarisation of the laser field. Then we apply a time periodic electric filed and found that such single potential is not enough to break the topological symmetry.

We investigate the manipulation of the spectrum in 1- spatial periodic magnetic field and 2- linearly polarised laser beam with an external periodically modulated static magnetic/electric field. We investigated in particular, the creation and the destruction of the Dirac-Weyl points. We found that at certain conditions the graphene is transformed into the two-dimensional Weyl metals, where each of the two original graphene Dirac cones is split into pairs of the Weyl cones. We also show that altering the laser's beam incidence (tilting) angle may lead to appearing and disappearing of the pairs of Weyl points, the opening gap in the spectrum, and its efficient manipulation. Deformation and symmetry breaking can be achieved via different laser's frequencies and amplitudes, hence the anisotropy can be controlled.

Acknowledgment

First, I would like to thank **Allah** Almighty for blessing me with this opportunity and the strength to carry it.

I would like to deeply thank my supervisors Prof. **Sergey Saveliev** and Prof. **Fedor Kusmartsev** for their help and continuous support as I owe them all the knowledge and academic growth I acquired these past years. During my study at Loughborough University I worked with academic and non-academic members in the physics department who were always of great of help, therefor I thank them all.

My deepest gratitude to my friends who were the fuel of this journey, **Tahani Aledwani**, **Hind Albalawi**, **Nora Alsaffar**, **Fatimah Albalawi**, **Munairah Aldwosari**, **Tagreed Faqih**, **Halimah Shanaishah**, **Zuhra Alhubaishi**, **Amjad Almunif**, **Amani Hasubah**, **Arwa Alshubily**, **Samira Alshukaili** and **Ibtisam Raziqy**.

Special gratitude to the teacher who motivated my passion for physics, **Ruba Hasubah**, and to my cousin and friend who was the encouraged me into postgraduate study, **Suad Alghamdi**.

To the souls of my grandmothers, **Salma Alghamdi** and **Jamilah Imam**, may they rest in peace, I am blessed because of their love and prayers.

My thanks and love to all my aunties and uncles. A special gratitude to my uncle **Abdullah Bahumran**, my spiritual father who has always been there for me. My love and appreciation to my dearest aunt **Zakia Bahumran**, thank you for all the joy and the care you give. I also would like to thank my uncle **Hatim Alfadhli**, who has been calling me Dr. for 4 years now. To my aunt **Moudhy Alfadhli**, I never forgot that you were the first person to encourage me to study PhD, and for that and many more I love you.

I would like to thank my father **Abdulrahman Alfadhli**, for his endless love and help. I thank my brothers; **Fahad**, **Muhanned**, **Mohammed**, **Hatim** and **Salman** and my sisters; **Shaimaa**, **Shatha**, **Jamilah**, **Sara** and **Salwa**.

My appreciation for my loving husband **Mohammed Alshehri**, and my little baby **Musk** for being my peace and comfort in the UK.

I owe my two eldest kids, **Thamer** & **Jood** great thanks and love, for their understanding and support through the years of my absence. I love beyond love.

I would like to dedicate this thesis to my mother **Ameerah Bahumran**, who is my role model in life, my motive to be greater than myself, and the real reason for my success.

Shahd, 2019

Table of Content

List of Figures

List of Tables

1 Introduction

1.1 Introduction to graphene

New materials have always been the key to new technologies. Just when scientists draw the boundaries to materials' dimensions and structures, a new material appears and becomes potentially promising. In 2004, a material "does not resemble any known material" [1] was listed as one of the new man maid materials that will shape the future [2][3][4]. It was a two-dimensional Carbon sheet, or a monolayer of graphite, or what is called Graphene.

Theorists believed that thermal fluctuations forbid the stability of two-dimensional structures as Landau and Peierls argued [5]. Thus, 2D materials where built on top of 3D matching crystals to avoid the displacement of atoms due to temperature fluctuation. However, in 2004 the Manchester research group led by Geim and Novoselov proved that a monolayer of Graphite can exist in a free state [6][7]. Such a discovery led to new chapters marked with Graphene, which actually was invented 440 years before it was proven.

Graphene crystal is worthwhile, not just for its amazing properties but also because it allowed the demonstration of other 2D crystals like silicene and germanene [8]. These crystals became obtainable as suspended films, in liquid

suspension, and on top of non-crystalline substrates. The ability to be able to design such materials, atom by atom, attracted a huge amount of research. However, this is not the only reason of the huge interest in graphene. A number of motivations can be listed. First, Graphene has promising technological applications, because it allows the control of carrier densities by application of gate voltages, which is essential in designing electronic devices. Furthermore, the silicon-based electronics becomes limited in terms of reduction; so graphene-based electronics could exceed that limitation. A second factor to the huge interest in the graphene field study is that it is connecting the condensed-matter physics and the high-energy physics. Graphene has shown exotic quantum behaviour at room temperature, and a relativistic behaviour, which can help in investigating quantum-field theoretical models [2][9]. Moreover, graphene gained a lot of interest outside the scientific community being the material best in everything. It is only one atom thick/thin, harder than diamond, stronger than steel, more flexible than rubber, and a better conductor than copper[10][11][12][13]. Therefore, graphene discovery is only a beginning to a rich knowledge and applications.

1.2 Thesis objectives and motivation

Since this gapless material has been demonstrated, the main problem that has been investigated is the gap band opening and controlling in the energy spectrum of graphene. A variety of methods have been established to open a gap in graphene's band, some are based on deforming the honeycomb structure of graphene, where other maintain it. All the methods that include functionalization processes, physical or chemical, allow gap opening even though they reduce the mobility and the on-state current of the charge carriers (such as covalent modifications of the graphene lattice, graphene nanomeshes and graphene nanoribbons …etc.)[14][15][16][17][18]. The deformation of the honeycomb structure can be realized to introduce scattering centres, producing non-controllable band gaps and enhancing electrons' effective mass[19].

2

In order to maintain the carriers' high mobility in graphene, its honeycomb structure has to be preserved. Substrate-induced bandgap opening is an example for a structure preserving method, however, the gap induced is non-tuneable [20][21]. Another method that preserve the hexagonal crystal is Graphene superlattices, which is not only simply modelled but also offers practical possibilities and applications[22][23][24][25][26]. As the thin layers of alternating crystals in a graphene superlattice have different band structures, a periodic potential will be created with a tuneable periodicity [27]. As result, the transition from valence to conduction will be allowed through minibands with a gap that can be controlled by the superlattice period[24]. A gap opening can also be obtained by applying a strain on graphene, which has shown stability with large strains[21][27][28]. One of the most effective methods is the application of an external field[29][30][31], which creates atomic sites with different electric potentials. However, this modification is only valid of multi-layered graphene. In a single layer graphene (SLG), applying a vertical field is will not introduce a gap in the band structure as the two sublattices in the crystal structure remains equivalent[19][24]. Hence, there is a demand for effective gap opening and electronic zone manipulation methods in SLG that will maintain the high carrier mobility and allow manipulation of Dirac points[32][33].

To control and to manipulate electron spectrum of graphene, periodic electric or magnetic fields can be applied in the existence of periodic electrostatic potentials (so-called graphene superlattices). Yet, the nanofabrication is required for graphene superlattices and this is of a high cost and does not provide a perfect tunability in modifying electron spectra. Recently, an analogy was found between electron spectrum in graphene superlattices and the spectrum in externally applied laser fields[32]. The application of laser fields to graphene creates a band gap structure in electron spectra (so-called Stark effect, causing the gap in the graphene spectrum). Moreover, such an effect can be easily controlled by changing the laser field amplitude and frequency. Applying different laser frequencies or amplitudes changes the size and location of the gap in the spectrum. Moreover, it was proven that, by applying laser fields, new Dirac points can be formed [32] and can be easily manipulated[33]. Nevertheless, the question remains if the laser-generated Dirac points in the

SLG electronic structure can be treated in the same manner as the usual graphene Dirac point and if and how the laser-induced Dirac cones is distorted/squeezed near these their Dirac points?

1.3 Aims

In this thesis we consider in details modification of the electron spectrum of graphene superlattices to control and manipulate Dirac cones.

The purpose of this study is to provide a theoretical analogy to superlattices graphene, by applying different periodic potentials to a single layer of graphene. The analogy is based on preserving the honeycomb structure of graphene and apply adjustable potentials. The aim of the approach is to investigate the gap opening in different periodicities and different polarisations. Then, the study focuses on duality between periodic potentials that are adjustable to allow Dirac points destruction/creation, Dirac cone symmetry and deformation, and energy gap opening/closing. The manipulation and tuning of the energy spectrum is based on parameters changing

The proposed theatrical model is promising in term of controlling Dirac cone structure in graphene spectrum.

1.4 Thesis outlines

Chapter 1 introduces graphene as the first stable 2D crystal and the research gap in the topic of graphene. Then **Chapter 2** and **Chapter 3** offer literature review of graphene's discovery, properties, fabrication, band structure theories, and applications.

Chapter 4, explains the theory of the used model using Floquet theory and resonance approximation to solve the 2D Dirac equation for electrons in graphene superlattices.

In **Chapter 5**, we introduce the problem of graphene in a single periodic potential by considering the case of time periodic laser with different polarisation and static electric/magnetic field.

Chapter 6, gives the detailed investigation of the graphene spectrum in the application of laser field and static electric/magnetic field. We show how the spectrum behaves in different sittings of the applied potentials.

Chapter 7 summarises the findings of the research.

2 Background

2.1 Demonstration of graphene

Graphene has been an academic material for more than sixty years, used to describe physical properties of carbon materials and a model for one and two-dimensional quantum electrodynamics [5]. There were many successful attempts to produce some forms of Graphene compounds before 2004, and it was used to study the carriers' dynamics in Graphite.

The band structure of graphene was first introduced by Wallace 1947 using tight binding model[34]. Then, a thin layer of graphene oxide was recognized, using transmission electron microscopy by Ruess and Vogt 1948 [35][36][37]. After that, in 1960s, Boehm et al demonstrated a sample of graphene oxide, and they were the first to actually call it "Graphene"[35][38][39].

The late illustration of Graphene can be related to two main reasons. The first is that it was believed that graphene couldn't be produced in a free state form as temperature prevents the crystal stability. Secondly, even if such believe was not considered true, there were no experimental tools to construct a one atom thin sheet of graphite[1][40].

In 2004, Geim and his research group demonstrated graphene sheets off a graphite substrate by using a scotch tape. Then, their sample was placed on a

SiO2 substrate and identified as being a one layer crystal using simple optical microscopy[5]. A more recent tool was using Raman spectroscopy, which allows faster selection. Consequently, graphene sheets can be produced freely, without resting on a substrate. Additionally, multilayer flakes of graphene became selectable[40]. Graphene plays a master role in understanding the carriers' behavior of other carbon allotropes.

2.2 Graphene as carbon atoms/crystal

2.2.1 Bonding in graphene

Carbon is considered the element of life, as it is the basis of organic components. Carbon systems and allotropes show a variety of properties, which can be regarded to the flexible bonds of carbon. Graphene is an allotrope of carbon, arranged in a hexagonal honeycomb lattice of a one atomic layer (Figure 2.1). In quantum information process, graphene structure is referred to as chicken wire[41].
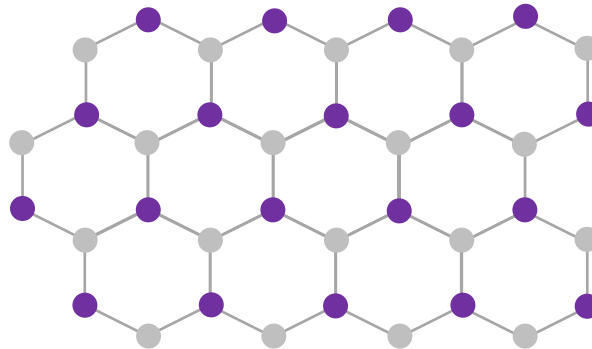
Figure 2.1 Hexagonal honeycomb lattice for SLG

Carbon has four valence electrons in the electronic structure is $(1s)^2 (2s)^2 (2p)^4$. It is possible that these electrons form four sp^3 orbitals, in the case of diamond. In graphene though, the electrons form one π bond (p_z orbital) and three sp^2 orbitals, a mixture of orbitals (s, p_x & p_y). These orbitals are all mixed together roughly equally and rearrange themselves in a plane at 120° angles

forming σ bonds (Figure 2.2). The superposition mixing of s, p_x& p_y states have the significant electron probability in the xy plane and they are called "sp²" hybridization as one s orbital is mixed two p orbitals. The p_z atomic orbital is left separated and unhybridized.

The sp² states form $3\,\sigma-$ bondig bands and $3\,\sigma^*-$ antibonding bands, while the p_z states forms $1\,\pi-$ band and $1\,\pi^*-$ band. Consequently, forming 8 bands in total.

The three $\sigma-$ bondig bands are the hybrid covalent bonds between the three nearest neighboring atoms between the atoms sites in the xy plane. These bonds hold the honeycomb structure together and have the lowest energy being all below Fermi level. In the ground state, the $\sigma-$ bondig bands are completely filled, thus they play no role in electronic conduction in graphene. The σ^*- antibonding bands are all above the Fermi level. Therefore, in ground state they are all empty. Since there is a finite gap between the minimum energy of the σ^* bands and Fermi level, these bands are neglected.

a) Top view   b) Side view

c) hexagonal configuration
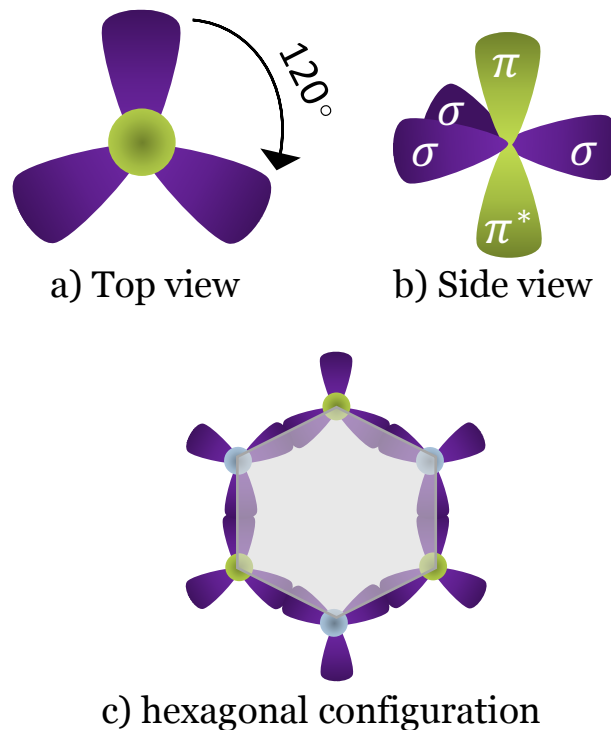
Figure 2.2 Atomic orbitals in graphene made up of σ hybridized bonds and π bonds in the hexagonal configuration

The unhybridized p_z orbital forms a delocalized π bond, by overlapping with a p_z from the next neighboring atom. The formed p band is perpendicular to the plane containing the three σ bonds (xy plane). The π states and $π^*$ states are at close energy levels, allowing the π electron to move freely between the atoms in the crystal. This electron is responsible for the high conductivity of graphene and also high light absorption. The movement of the delocalized π electron is discussed in the tight binding section.

2.2.2 Crystal structure of graphene
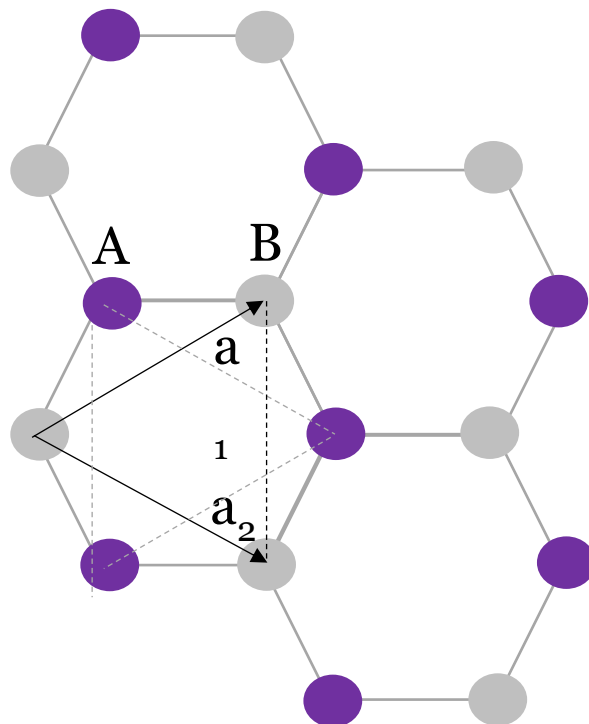
Figure 2.3 Graphene honeycomb lattice, showing the two triangular Bravais sublattices (A and B) each having the two basis vectors $\vec{a}_1 = a/2\left(3, \sqrt{3}\right)$ and $\vec{a}_2 = a/2\left(3, -\sqrt{3}\right)$ with a lattice spacing a = 0.142 nm = 1.42 A°

The hexagonal lattice of graphite is not a Bravais lattice, because atoms in the next unit cell are not equivalent. Therefore, graphene lattice can be looked at as two triangular sublattices (A and B) with two atoms basis (A and B) (FIG 2.1). The basis vectors for each triangular lattice are[42]:

$$\vec{a}_1 = \frac{a}{2}(3, \sqrt{3}), \quad and \quad \vec{a}_2 = \frac{a}{2}(3, -\sqrt{3}) \qquad\qquad (2.1)$$

With lattice spacing (the nearest neighbor distance) $a \approx 1.42\ A°$, and a unit cell of an area $A_{uc} = \frac{3\sqrt{3}a^2}{2} = 0.051\ nm^2$. In such lattice, the density of carbon atoms is $n_c = \frac{2}{A_{uc}} = 39\ nm^{-2} = 3.9 \times 10^{15} cm^{-2}$. It is worth emphasizing that the density of the π electrons is equal to the density of carbon atoms. However, this is not the density of charge carriers, which has to be measured under the application of electric field.

The primitive cell of graphene is chosen to contain 1 atom from each sublattice as the Bravais lattice is considered a two atoms basis A and B. The primitive cell is represented by the vectors a and a2 as the following diagram shows.
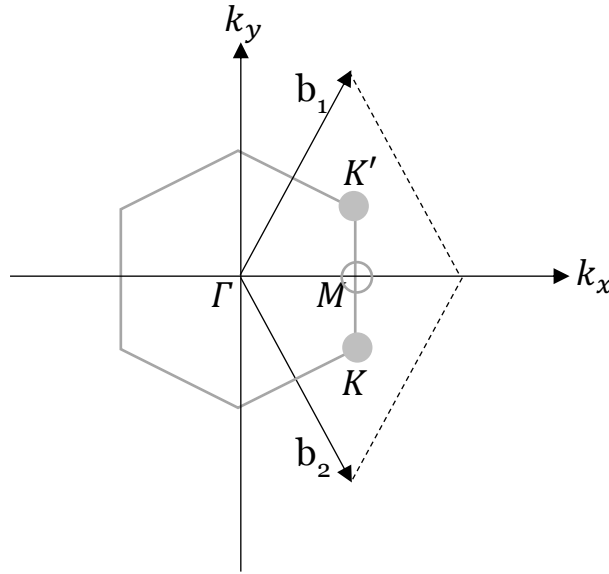
Figure 2.4 The reciprocal lattice for graphene showing the first Brillioun zone with primitive vectors $\vec{b}_1 = 2\pi/3a\ (1, \sqrt{3})$ and $\vec{b}_2 = 2\pi/3a\ (1, -\sqrt{3})$. The first Brillioun zone is the hexagonal grey lattice within the reciprocal lattice. The conical points K and K' at the corners of the first Brillioun zone are connected to the remaining four corners by the translational vectors in the reciprocal lattice.

To define the reciprocal lattice in graphene, we consider the triangular sublattices. Thus, the reciprocal vectors are[42]:

$$\vec{b_1} = \frac{2\pi}{3a}\left(1, \sqrt{3}\right) \text{ and } \vec{b_2} = \frac{2\pi}{3a}\left(1, -\sqrt{3}\right)$$ (2.2)

The first Brillouin can be drawn in the reciprocal space by connecting six inequivalent points. It consists of two point, K and K', which are special high-symmetry points including M. The points are represented by wave vectors [42]:

$$\vec{K'} = \frac{2\pi}{3a}\left(1, \frac{1}{\sqrt{3}}\right) \text{ and } \vec{K} = \frac{2\pi}{3a}\left(1, -\frac{1}{\sqrt{3}}\right)$$ (2.3)

where,
$$\vec{M} = \left(\frac{2\pi}{3a}, 0\right)$$ (2.4)

The remaining four corners can be connected to the point K and K' by the translational vectors in the reciprocal lattice[42][43].

2.3 Properties of graphene

2.3.1 Graphene electrical properties

The electrical properties of graphene are determined by its structure. Being a monolayer of carbon atoms indicates a certain bonding type as described before in previous sections. The three strong σ bonds are responsible for the tightly binding structure, which is why graphene is useful in electronics as it has high elasticity and strong resistance against destruction. Yet, it can be stretched and bent easily due to its monolayer structure. So, the flexibility of graphene can be related to the σ bond, which is responsible for the robustness property in all carbon allotropes. Each of the three σ bonds in will form a covalent bond with the neighboring atom and that is the reason for, making graphene crystal 100 times stronger than steel. On the other hand, the π bond is formed by one p orbital leaving the conduction band half filled, thus giving metallic properties to graphene. So, this bond is responsible for the heat and electricity carry of

graphene[44][45]. The single π bond is responsible for electrical conductivity as it leaves one electron free to move above or below the graphene sheet. Furthermore, the atom-atom bonds are enhanced in graphene by the overlapping of the neighboring π orbitals.

The electrical properties of a material can be explained by looking at its behavior under the application of an electrical field. In a metal or a semiconductor, carriers (electrons and holes) response to electric field by moving through the material. The measure of how quickly carriers propagate is called mobility and it is usually specified in units of $cm^2\ V^{-1}\ s^{-1}$. Each material shows different mobility, therefore, it can be used to identify the conductivity in different materials.

The mobility of graphene varies as the fabrication method produces different structure quality. It has been suggested that in perfect crystal of an exfoliated graphene can reach a mobility of 200,000 $cm^2\ V^{-1}\ s^{-1}$[46]. Taking into consideration the concentration of the carriers in graphene with such high motilities, graphene has a very high electrical conductivity. Because of the linearity of low energies near the 6 corners of the Brillouin zone (Dirac points) in graphene (the energy-momentum relation), electrons and holes have zero effective mass. Electronic conductivity can be enhanced by doping, as at the Dirac points the density of states is zero, and doping will change the Fermi level and will create better conducting material.

Regardless of the concentration of carriers in graphene at Dirac points (which is zero), graphene experiments indicated that the minimum conductivity in graphene has been found to be double the mobility observed in quantum wires ($\sigma_O \sim 4e^2/h$)[2]. Ballistic transport can be performed by the charge carriers, with no scattering, in graphene at room temperature[47]. Large Coulomb energies are responsible for magnetism and collective effects in graphene.

2.3.2 Graphene thermal properties

The study of the phonon dispersion of graphene or the lattice vibrational modes leads to understanding of the thermal properties of graphene. The ability

of conducting heat in suspended graphene is allowed by ballistic phonons, which has been illustrated by the use of high-resolution vacuum scanning thermal microscopy[48]. On the other hand, if graphene is placed on a substrate, the number of scattering will increase, hence, the thermal conductivity will decreases. So, due to the scattering heat will be lost in the substrate[29]. The thermal conductivity decreases furthermore if the number of layers in graphene was increased. The mean free path of thermal phonons in many layers graphene is larger than the mean free path in graphene on substrate[30]. Any additional disorder due to fabrication for example will reduce the thermal conductivity even more.

It has been reported that in freely suspended sample of graphene, thermal conductivity of at room temperature can reach about 2000–4000 W m^{-1} K^{-1} [31]. Which is one of the highest thermal conductivity of any known materials. The thermal conductivity of graphene on substrate (silicon-dioxide for example), can reach a value of about 600 W m^{-1} K^{-1}[49]. In both cases, the thermal conductivity of graphene is very high, however, it is strongly affected by environment (interaction, defects, edged...etc).

Considering an almost pure sample of suspended graphene, the electrical transport in the sample changes with temperature. In low temperature, the electrical resistivity can be negligible due to low scattering. Therefore, the carrier can be ascribed a mean free path. As the temperature increases, the electrical resistivity changes in dependence of the carriers' density. In the case of high density, graphene shows a metallic behavior. The conductivity decreases with the increasing temperature, due to electron-phonon scattering. However, it is still considerably small scattering as the observed mobility still high (~120,000 cm^2/Vs at T≈240 K). On the other hand, in low carrier density, graphene exhibit a non-metallic behavior, thus the conductivity decreases with the decreasing temperature[50].

2.3.3 Graphene photonic properties

Graphene is a material of high transparency, as it is an atom thin with a single π bond. It has been shown that a single layer of graphene transmits ~97% of the incident light, absorbs ≈ 2.3% (regardless of its wavelength) and reflects <0.1%, which is very low reflection[11]. Nevertheless, the wide range of absorption indicates there is a strong graphene-light interaction. Graphene does not produce resonant fluorescence, as relaxation in graphene is fast. Even in strong electromagnetic filed, as graphene atoms are in a single quantum state.

Thus, graphene is promising for the use in photonic devices as it makes an excellent conductive electrode. Being highly conductive with high light transmission makes graphene a candidate for solar cells, flat panel displays, touch screens, OLEDs, and it has been suggested for the use of small screens [1]. So, the usage of graphene in such electronic and photonic applications is actually dependent on the full control over the band structure of graphene. This includes: "lateral size, layer thickness homogeneity, and purity"[11].

2.4   Fabricating graphene

Graphene is a one layer of graphite, it is a 2D crystal, and it takes more than one layer to build up a 3D crystal. It will take up to 11 layers of graphene to reach 3D structures, so any 10 layers or less is still a 2D crystal. This number of layers was specified based on the electronic structure, which evolves with the number of layers and at 10 layers the structure approaches the 3D limit of graphite. Then, a more distinguishable feature of a graphene and its bilayer is that they are both gapless semiconductors having simple electronic spectra, with only one type of holes and one types of electrons. The electronic spectra become complicated in the three layers graphene (or more), the conduction and valence band overlaps, and appears a number of charge carriers' types[5].

Graphene is extracted from graphite using three methods, which can produce samples of graphene with full preservation of the hexagonal structure.

The physical properties' of graphene depends on its quality which depends on the fabrication method. The three methods are (in order of producing the best quality graphene):

1. The mechanical exfoliation technique (from bulk graphite).
2. The vacuum epitaxial growth technique (on SiC substates).
3. The chemical vapor deposition (on metals).

2.4.1 The mechanical exfoliation or cleavage

This exfoliation technique, elaborated mainly by the Manchester group, is one of the simplest methods of fabricating graphene. The process is mainly peeling a bulk of graphite, by exfoliating the bulk with a scratching substrate (scotch tape). Mainly by folding and unfolding the sticky substrate on the bulk, a thinner sample of graphite will be produces on the substrate. The first sample could contain tens or hundreds of graphene layers. Thus, by repeating the same process one can reaches a single layer of graphene (FIG 2.2). Then, by looking at the simple optical interference patterns, or Raman spectroscopy, a single layer of graphene can be identified.

Few problems with the exfoliated graphene: 1. The monolayer graphene will be distributed on the substrate. 2. Only small quantities of graphene can be produced each time. However, the produced samples have a high quality structure (in term of defects) and a very high mobility that at room temperature can excess 15,000 $cm^2 V^{-1} s^{-1}$ [51].
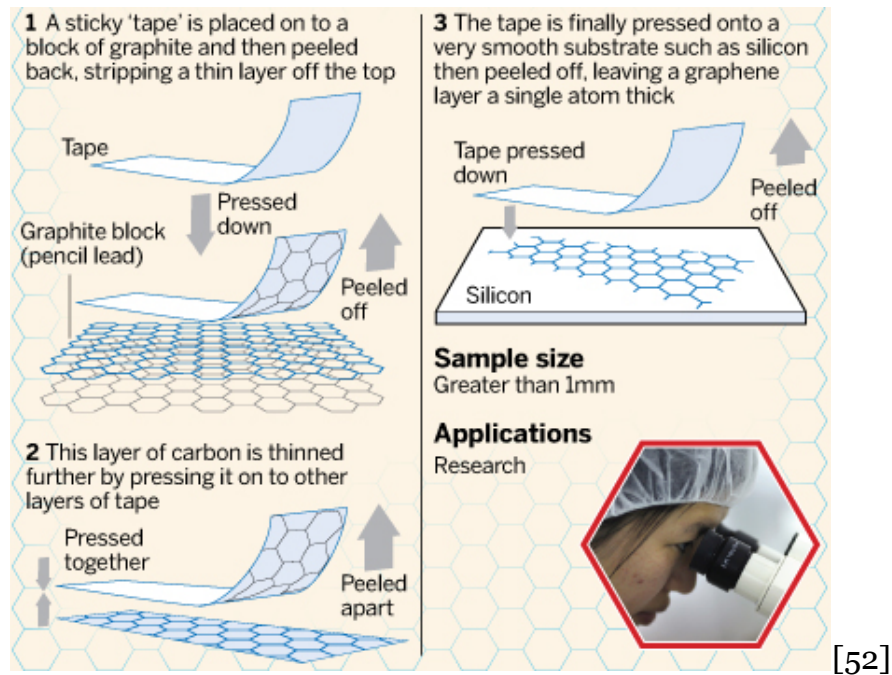
Figure 2.5 Mechanical exfoliation method

2.4.2 The vacuum epitaxial growth technique

The epitaxial growth technique, developed by the Atlanta group[53], is an alternative method to the mechanical cleavage. This process basically consists of evaporating silicon carbide (SiC), which will be plated on a silicon wafer, to form graphene. In SiC (4H or 6H) hexagonal crystal, silicon is less tightly bonded. At a temperature of about 1300° C, silicon atoms start evaporating and only carbon atoms remain on the surface forming graphitic layers as the process continues (FIG 2.3).

The number of these layers can be controlled if one uses Si-terminated (0001) surface, which graphitize slowly, allowing the formation of a single layer of graphite (graphene) or two as aimed[43]. If C-terminated (0001) surface was used in the vacuum epitaxial growth, then larger numbers of graphene layers will be formed as this type of surface allows a very fast graphitization process[43].

The analysis of the epitaxial graphene shows that this type has a quality less than the one of the exfoliated graphene. First, the epitaxial-grown graphene

usually has some structural defects, due to the high temperature some carbon atoms burns during the process[54]. The structural defects can be spotted by the use of Raman topography[55][56][57]. Second, the layers in epitaxial graphene are less tightly bonded than the exfoliated graphene layers, due to the large distances between the layers in the formation process. These distances can be determined by X-ray measurements[58].

As a consequence of these characteristics, epitaxial graphene is less chosen as sample in transport measurements (in contrast to the exfoliated graphene). Also, the mobility of the epitaxial graphene is smaller than the mobility of the exfoliated graphene; however, it is better than the mobility of the CVD graphene. The study of epitaxial graphene by Raman topography has shown that: the thickness, the stacking and the homogeneity of the graphene layers, all affect its mobility[56]. In room temperature, the mobility of epitaxial grown graphene can reach 5,000 cm^{2}V^{-1}s^{-1} (in the case C-terminated (0001) surface)[51].

[52]
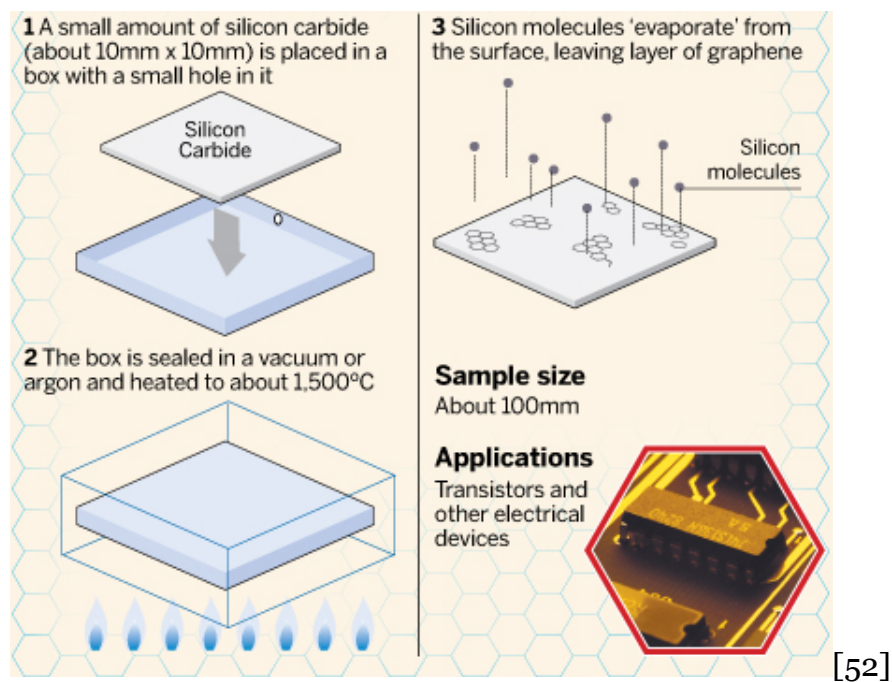
Figure 2.6 Epitaxial growth method

2.4.3 The chemical vapor deposition (CVD)

This approach was first reported in 2008/2009 [CVD+1CVD]. Its potential is the easily mass production of graphene with low cost; therefore, this method is usually used for industrial purpose [55][59]. In this method, a sample of carbon atoms abides to a metallic surface, which helps decomposing the chemical bonds in carbon aside with the high temperature involved in the process. The easiest substrate to transfer graphene from is copper-foil, thus it is mostly chosen in the CVD method.

The carbon atoms reaction to the high temperature on the metallic substrate is basically is a repositioning behavior. Each carbon atom starts occupying a position on the surface, pushing the neighboring atom to the sides of the substrate. The process simply continues until a one layer of carbon is formed or at the edge of the metallic substrate (FIG 2.4). Hence, the larger the surface is, the larger production results. In the meanwhile, carbon atoms start an order of a hexagonal (honeycomb) lattice in some places on the surface before the whole sample is crystallized to form graphene. This means that at each initial spot of crystallization, the lattice produced can be differently oriented from the other layers.

1 A substrate (usually copper) is heated in a furnace at low pressure to about 1,000°C. This anneals the copper

Heated copper substrate

2 Methane and hydrogen gases flow through the furnace

3 Carbon atoms from the methane are deposited on to the copper. They crystallise as a continous graphene sheet

Sample size
About 1m

Applications
Photonics, nanoelectronics, transparent conductive layer sensors and bioapplications

[52]

Figure 2.7 Chemical Vapor Deposition

As these different oriented crystallizations spread and meet, line defects will occur causing what is called grain boundaries[60]. These boundaries are, aside from other defects, the main reason of the low mobility of CVD graphene (in comparison to the exfoliated and epitaxial graphene)[60]. The transmission electron microscopy (TEM) and scanning electron microscopy (SEM) can be both used in defects determination of CVD graphene[49]. In short perfectly structured CVD graphene (no grain boundaries), the mobility can reach 2, 700 $cm^2V^{-1}s^{-1}$[60].

2.5   Quantum behavior of graphene

Graphene exhibits a fast motion of charge carriers, due to their zero effective mass, hence providing a very useful model to examine electrodynamics phenomena without the need to costly acceleration equipment [29]. Furthermore, graphene shows quantum behaviours at room temperature. This is also another factor making graphene a recommended candidate for studying such behaviours with no need to cooling mechanisms [2].

2.5.1 Anomalous quantum Hall effect (QHE)

In an electrical conductor and under the application of magnetic field, a voltage difference is created in the conductor, which is called Hall effect. At low temperatures and very strong magnetic field, the Hall effect (or Hall resistance) becomes quantised. This is called Integer QHE, however, in the case of quasiparticles the QHE becomes fractional [50][11].

QHE has been reported in graphene experiments within a SLG at room temperature [36][2]. Although the samples showed quantised resistance, the integer QHE is not exactly the same as in 2D semiconductors. The quantum conductivity is shifted in graphene by $\frac{1}{2}\ \sigma_0$, which is the minimum conductivity). This shift can be controlled by doping [5]. On the other hand, the fractional QHE

in graphene is, similarly in semiconductor devices, correlated to the electron-electron interaction.

2.5.2 Perfect Klein tunnelling

In quantum mechanics, a particle can pass through a barrier regardless of the classical condition, where the kinetic energy of the particle K has to be larger than the potential U, in a phenomenon known as tunnelling. In 1929, Klein dealt at the electron scattering from a barrier with the application of Dirac equation. He showed that if the potential is of some order of the electron mass, then the electron will always tunnels through the barrier [5].

This quantum behaviour can occur in graphene and electron exhibits a perfect transmission through the potential barrier [29] [54]. However, the perfect tunnelling occurs only under several conditions. The shape of the potential barrier is essential factor in the behaviour of the tunnelling, also the energy of the tunnelling electron in respect to the potential height [55]. Moreover, the angle of the incident electron also contributed to the smoothness of the tunnelling in graphene [53][51].

2.6 Graphene devices

2.6.1 Graphene sensors

The need of high sensing in small dimensional devices and circuits is never limited. Graphene-based sensors is a well preforming high precision detectors due to the high mobility, low scattering and noise of graphene sheets [61]. Consequently, the graphene-based sensors are time resolving due to graphene properties [29]. The fabrication of such devices is based on simple structuring knowledge, as a quantum dot with two Nanoribbons on either side will act as a charge sensor [37]. The high sensitivity in these devices is influenced by the conductivity of graphene stripes, which is sensitive to defecting and importing [29].

The use of graphene ribbons and graphene meshes in these devices can be regarded to their role in creating a gap band in the energy of graphene [62]. The difficulty in the application of graphene-based devices in general is the gapless feature and the Klein tunnelling in graphene, which makes controlling the transportation of electrons a challenging task [61].

2.6.2 Graphene transistors

Semiconductors devices has reached a limited speed and dimensional reduction. Thus, emphasising the need to a new material such as graphene, with new possibilities in terms of scaling and mobility [14]. Implying and controlling of devices and circuits is based on transistors, which is about to be "reborn" with the application of graphene transistors [29]. The main challenge in the transit process is the zero gap structure of graphene. Transistors can be used as a logical controlling element if it can switch from a state to another (from ON state to OFF state). Therefore, the task in graphene transistor making is to create and control a gap band in the energy spectrum. The use of carbon nanotubes and graphene Nanoribbons is a method of producing the required gap. Furthermore, other methods can be applied to obtain the same aim with the use of channels of bilayer graphene (BLG), graphene oxide or graphene with impurity [5]. Hence, changing the band structure of graphene creates an energy gap.

Several graphene transistors designs have been proposed recently. For example, graphene oxide transistor provides a simple application and can result in channel mobility up to 100 $cm^2 V^{-1} s^{-1}$ [59]. Also, carbon nanotubes transistors were designed, and it promises to produce high mobility transistors due to the ballistic transport in carbon nanotubes [34].

2.6.3 Graphene photonic devices

The transparency of the thin graphene sheets makes them ideal for photonic devices. The monolayer structure allows a small light absorption [60]. Many proposed application is graphene based such as small touching screens, solar photonic devices and photonic transistors. The principle of photo-

conduction increases the number of charge carries in graphene, due to the excitation caused by the photons absorption. Therefore, the conduction is a subject of increase [29].

2.7 Summary

The demonstration of graphene has led to many possibilities due its unique structure and properties. Graphene is a single layer of graphite sheet, which is made of carbon atoms arranged in a hexagonal lattice structure. The hexagonal structure is usually looked at as two sublattices with two atomic cites A and B. Such configuration allows the valence electrons in carbon to be arranged into forming one π bond and three σ bonds. The π states are in lose energy levels allowing the electron to move freely (massless) from an atom to another. This bond is responsible of graphene electronic properties such as: high mobility, heat and electrical conductivity, and light transmission. The properties of graphene depend on the quality of its fabrication method, where mechanical exfoliation producing best graphene quality, while vacuum epitaxial growth and chemical vapor deposition provide less quality. Graphene shows anomalous quantum behaviors such as fractional Hall effect and perfect Klein tunneling. Thus, graphene is promising in studying quantum behaviors and for new quantum applications such as in sensors, transistors and photonic devices.

3 Graphene Energy Band

3.1 Band theory

Wallace introduced the band structure of graphene in 1946 [32]. His aim at that time was to study the structure of graphite. He considered one layer of graphite, which is graphene now, to explain some of the physical properties through the band theory. Wallace showed that the σ bonds do not play part in conductivity, whereas the π bond leaves the conduction band half-filled. That is why he concluded that Graphite can be treated as having one conduction electron, and that the electrical conductivity in the 2D crystal of graphite theoretically exists. Wallace also concluded that at six points of the Brillouin zones (which is called Dirac points), the electronic spectrum in graphene is gapless and has the form of a canonical Dirac spectrum. Later on (after 2004), it was proven by experiments that the charge carriers in graphene were actually Dirac fermions[5].

When studying the electronic band structure of graphene, one is considering the energy bands of π electrons. As discussed before in chapter 2, the π electrons are the responsible for the electronic properties in graphene. Furthermore, the σ electrons have energies too low than the Fermi level[23].

The π energy bands in graphene can be described through Bloch's theorem, tight binding model, and Dirac equations.

3.2 Bloch's theorem

The best way to describe Bloch's theorem is by saying that it represents the periodicity of a wavefunction ψ over a periodic crystal structure with a lattice vector R_i [23]:

$$\psi(r) = e^{ik.r}u(r) \qquad (3.1)$$

where, ψ is the electron's wavefunction in a crystal (usually refered to as Bloch's wavefunction), r is the position, k is the crystal wave vector, and u is a periodic wavefunction which has the same periodicity as the crystal, hence [23]:

$$u(r + R_i) = u(r) \qquad (3.2)$$

The concept of the electronic band structure is based on representing the energy eigenstate of an electron as Bloch's wave $\psi_{n,k}$. The index n refers to the discrete bands, which may share the same wave vector k. Because k is periodic, hence $\psi_{n,k} = \psi_{n,k+R_i}$, then one can describe all the n Bloch's waves within the first Brillouin zone.

Although electron transport in graphene is determined by Dirac equation, the need to solve Schrodinger equation is essential if a periodic potential is applied. Thus, it is needed to distinguish semiconducting properties.

Finding a solution to Schrodinger equation in 2D crystals could be obtained using a number of methods. Nevertheless, there are some general characteristics to the solution no matter how it was gained.

These properties could make the calculation easier, or it could allow some approximation to obtain a general understanding of the Block wave. Basically, if a periodic potential is applied to a periodic function (periodic with respect to the crystal), then all Schrodinger equation solution of the electron wave should be of the form of a Bloch's wave with the same periodicity equation (3.1).

It is rather useful to expand the potential and the electron wave function into Fourier series and represent the Schrodinger equation to obtain specific solutions [46][47].

Each atom has four atomic orbitals to be considered in the Bloch wave function as an 8 terms function [62]:

$$\psi_{\vec{k}} = \sum_{R} e^{i\vec{k}.\vec{R}} \{ b_{AS}\varphi_{AS} + b_{Ap_x}\varphi_{Ap_x} + b_{Ap_y}\varphi_{Ap_y} + b_{Ap_z}\varphi_{Ap_z}$$
$$+ b_{BS}\varphi_{BS} + b_{Bp_x}\varphi_{Bp_x} + b_{Bp_y}\varphi_{Bp_y} + b_{Bp_z}\varphi_{Bp_z} \} \quad (3.3)$$

where $\varphi_{AS}, \varphi_{Ap_x}, \varphi_{Ap_y} \& \varphi_{Ap_z}$ are the $s, p_x, p_y \& p_z$ atomic orbital wavefunctions for atomic site A, and $\varphi_{BS}, \varphi_{Bp_x}, \varphi_{Bp_y} \& \varphi_{Bp_z}$ are the $s, p_x, p_y \& p_z$ atomic orbital wavefunctions for atomic site B. Therefore, for each value of wave vector $\vec{k}$ in the 1stBZ, there are eight bonds and hence eight energy spectrums $\varepsilon_n(\vec{k})$.

3.3 The tight binding model for electrons in hexagonal lattice

Tight binding model is a method uses a set of wave functions to calculate the electronic band structure. The basic assumption made in this approach is that the ionic potentials (or the crystal potential) are strong. Due to that, when an electron passes on while moving through the lattice, the electron is captured by the ion for a period of time, before the electron tunnels to another ion. During the capturing time, the electron orbits around the ion. As a result, the wave function of the electron becomes the same as the orbital function of the atom [23].

In the case of honeycomb lattices, the tight binding model is based on constructing a wavefunction as a superposition of the atoms' orbital wavefunctions. The atoms considered are the atoms in the Bravais lattice described by the lattice vectors [22]:

$$R_i = m_i a_1 + n_i a_2 \qquad (3.4)$$

where, m_j and $n_j \epsilon \ \mathbb{Z}$.

The produced wavefunction is called "trail wavefunction", and it is symmetrical under the translation of the lattice vector. The simplest case in approaching the tight binding model is to consider a Bravais lattice with one atom, and hence one electron, per unit cell. The tight binding Hamiltonian for an electron ℓ is[23]:

$$H_\ell = -\frac{\hbar^2}{2m} \Delta_\ell + \sum_{j=1}^{N} V(r_\ell - R_j), \qquad (3.5)$$

where, ℓ is an integer for any arbitrary electron, $\Delta_\ell = \nabla_\ell^2 = \left(\frac{\partial}{\partial x} + \frac{\partial}{\partial y}\right)^2$ is the two dimensional Laplacian operator, $r_\ell = (x_\ell, y_\ell)$ is the electron's position, m is the mass of the electron, R_j is the ion's site, V is the potential energy felt by the electron because of the ions, and N is the number of the lattice points.

So, the total Hamiltonian of the lattice is[23]:

$$H = \sum_{\ell}^{N} H_\ell \qquad (3.6)$$

Electrons' motion in graphene is controlled by the nearest-neighbor approximation. The moving electrons are the π electrons only, and they motion with a hopping parameter t [49]. This hopping process only occur within one sublattice atom to another, such that there is no electron hopping from the sublattice A site to another A site.

The tight binding Hamiltonian in term of the wave vector $\vec{k}$, is a 2 by 2 matrix [22]:

$$\hat{H}(\vec{k}) = \begin{pmatrix} 0 & t\, S(\vec{k}) \\ t\, S^*(\vec{k}) & 0 \end{pmatrix} \qquad (3.7)$$

where, t is the first hopping parameter and $S(\vec{k})$ is given by:

$$S(\vec{k}) = \sum_{\vec{\delta}} e^{i\vec{k}\vec{\delta}} = 2\exp\left(\frac{ik_x a}{2}\right)\cos\left(\frac{k_y a \sqrt{3}}{2}\right) + \exp(-ik_x a) \quad (3.8)$$

Therefore, the energy can be defined as:

$$E(\vec{k}) = \pm t|S(\vec{k})| = \pm t\sqrt{3 + f(\vec{k})} \qquad (3.9)$$

where

$$f(\vec{k}) = 2\cos(\sqrt{3}k_y a) + 4\cos\left(\frac{\sqrt{3}}{2}k_y a\right)\cos\left(\frac{3}{2}k_x a\right) \qquad (3.10)$$

Because of band crossing, $S(\vec{K}) = S(\vec{K}')$[41]. Therefore, when calculating the Hamiltonian, only next-nearest-neighbor hopping should be taken into account and all other hopping parameters can be neglected (hence, we include the two first hopping parameters t & t' and neglect t'' and higher). The energy can then be found to be [22]:

$$E(\vec{k}) = \pm t|S(\vec{k})| + t'f(\vec{k}) = \pm t\sqrt{3 + f(\vec{k})} + t'f(\vec{k}) \qquad (3.11)$$

The second term is responsible of breaking the electron-hole symmetry. It shifts K points from $E = 0$ to $E = -3t'$ without changing the symmetrical nature of the Hamiltonian near the conical points. The symmetrical behaviour of the electron and hole Hamiltonian is topologically protected within the BZ.

3.4 Energy spectrum in graphene

3.4.1 Dirac points

The energy spectrum in graphene can be explained by understanding the crystalline structure in figure (3.1). Looking at the energy spectrum at one corner of the Brillouin zone, there will be two bands, which we can label as − and + for now, both having the same number of states. As in graphene there is only one π

electron per atom, then the electron will occupy a state of spin up ↑, or a state of spin down ↓. The band with the lower energy is the − band, which is the valence band. The electron will occupy a state in this lower band making the valence band fully occupied. The + band, which is the conduction bad, will be left completely empty. Therefore, the Fermi level will be at the point where the valence band and the conduction band touch. This point is what is called Dirac point, where the conduction band and the valence band form reversed canonicals. The electrons in graphene have zero effective mass, meaning that they can be treated as massless fermions using Dirac equations, which is described in the following section. Thus, the six corners of the 1stBZ in graphene are called Dirac points in analogy to the zero-mass limit of the relativistic Dirac equation, where electron and positron bands touch at zero momentum.

The conduction and the valence bands meet exactly and only at the six corners of the 1stBZ. The upper and the lower cones are referred to as the electron and hole cones. The six Dirac points are noted as three K points representing sublattice sites A, and K' points for sublattice B. The electronic states located near the cones are described by two set of 2D spinors [48], with zero number of states at K and K' points. Although the valence and the conduction bands touch at six Dirac points, they never overlap. Because of Dirac points, graphene is considered a zero-bandgap semiconductor or a semimetal.

3.4.2 Dispersion relation

Semiconductors usually form parabolic dispersion relation near Fermi energy, apart from graphene, which has a linear dispersion of the π band with the separation distance. Graphene has unique properties because of this linear dispersion relation. Photons are also characterized by a linear dispersion relation because of kinetic energy being much larger than its mass energy. Therefore, the electrons in graphene can be considered ultra-relativistic particles as they copy the behavior of photons. The Fermi velocity (v_F) of graphene electrons is 300 times smaller than the speed of light, thus v_F is energy independent. Thus, the energy around K points for electron in graphene is proportional to momentum as:

$$E(\vec{k}) = \hbar v_F |\vec{p}|$$
(3.12)

where $\hbar$ is Planck's constant, v_F is Fermi velocity and $\vec{p}$ is the momentum.

a) 3D hexagonal spectrum

b) hexagonal 1stBZ
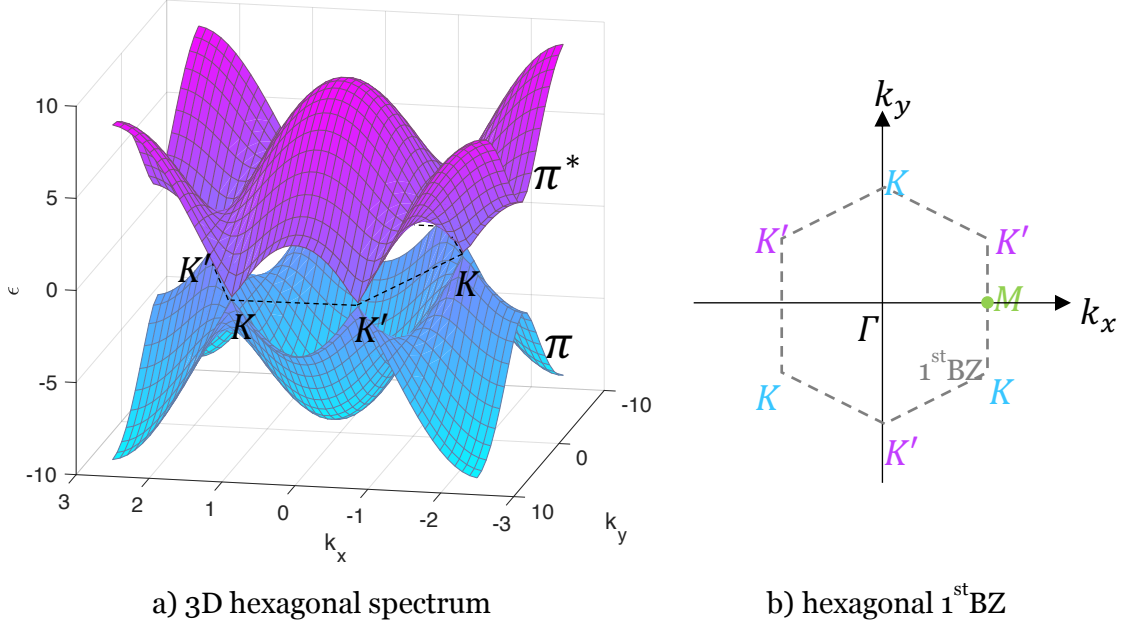
Figure 3.1 The gapless energy spectrum as a function of wave vector $\vec{k}$ (a) showing the valence band (upper spectrum) and conduction band (lower spectrum). The Fermi level is at the canonical points (Dirac points), where the valence band osculate the conduction band. (b) The hexagonal first Brillouin zone showing the only 6 corners conducting the π and π^* bands (K and K' points). The gap between the valence and the conduction band occur at the M points.

3.4.3 Massless Dirac fermions in graphene

At very low energy, the two sublattices A and B, (hence the two conical points K and K'), should be taken into account when finding the Hamiltonian such that[22]:

$$\hat{H} = \begin{pmatrix} \hat{H}_K & 0 \\ 0 & \hat{H}_{K'} \end{pmatrix}$$
(3.13)

where:

$$\widehat{H}_K = -i\hbar v_F \vec{\sigma} \, \nabla \qquad (3.14)$$

$$\widehat{H}_{K'} = \ \widehat{H}_K^T \qquad (3.15)$$

having $\vec{\sigma} = (\sigma_x, \sigma_y, \sigma_z)$ are the 2D Pauli matrix $= \begin{pmatrix} 0 & 1 \\ 1 & 0 \end{pmatrix}, \begin{pmatrix} 0 & -i \\ i & 0 \end{pmatrix}, \begin{pmatrix} 1 & 0 \\ 0 & -1 \end{pmatrix}.$

This Hamiltonian in equation 3.10 is a two-dimensional Dirac Hamiltonian for massless fermions [22]. The low-energy-momentum dispersion relation can be written as [22]:

$$E(p_x, p_y) = \ \pm v_F (p_x^2 + p_y^2)^{\frac{1}{2}} \qquad (3.16)$$

where, (p_x, p_y) are the electron momentum, v_F is the Fermi velocity, and E is the energy spectrum, which equals zero at Dirac points. Although graphene is a gapless semiconductor, sometimes it is applicable to create a gap in the graphene's band structure. Such a goal can be achieved using various techniques like selective doping, applying a gate voltage, substrate engineering, or deposition of molecules on graphene layer[49]. Some methods are described later in this chapter.

3.5 Dirac equation

To describe the electrical properties of materials it is sufficient to use Schrodinger equation, however, not in the graphene case. The charge carriers in graphene exhibit relativistic behaviour of quasiparticles with low energies and can be easily and accurately described by Dirac equation. These quasiparticles could be considered as massless electrons or charged neutrinos and they called massless Dirac fermions. Dirac equation basically describes a wave function ψ with four components by four coupled differential equations [49].

Graphene is a zero-gap semiconductor, with low-energies quasiparticles that can be describes by the Hamiltonian [49]:

$$\hat{H} = \hbar v_F \begin{bmatrix} 0 & p_x - ip_y \\ p_x + ip_y & 0 \end{bmatrix} = \hbar v_F \, \vec{\sigma} . \vec{p} \qquad (3.17)$$

where, the Dirac-like Hamiltonian is $\hat{H}$, Fermi velocity is v_F, the quasiparticles momentum is $\vec{p} = (p_x, p_y)$, and Planck constant is considered $\hbar = 1$. The energy can be found by simply finding the eigenvalues of the Hamiltonian:

$$\hat{H} \, \psi_{A,B} = E \, \psi_{A,B} \qquad (3.18)$$

The lattice of graphene is a hexagonal lattice (honeycomb lattice) that is made up of two sublattices referred to as sublattice A and sublattice B. Both equivalent sublattices are associated with cosine-like energy bands that intersect at zero near the boundaries of Brillouin zones. Therefore, the energy spectrum in graphene forms two canonical sections.

If a charged particle in moving in an electromagnetic field (classically), then the fields are defined by static and vector potentials such that[22]:

$$E = -\nabla U(x) - \frac{1}{c} \left(\frac{\partial A(t)}{\partial t} \right) \qquad (3.19)$$

$$B = \nabla \times A^H(x) \qquad (3.20)$$

where, U is static potential, A and A^H are vector potentials, and c is the speed of light which is replaced in graphene by Fermi velocity v_F.

Then the system is described by the classical Hamiltonian for a charged particle [22]:

If charged carriers are in motion in graphene, behaving as zero mass particles, then their dynamics can be described by 2D Dirac Hamiltonian as the solution to:

$$\hat{H} \, \psi_{A,B} = i \frac{\partial}{\partial t} \, \psi_{A,B} \qquad (3.21)$$

which is expressed as[30]:

$$\widehat{H} = \{\vec{\sigma}.\,[\vec{p} - \vec{A}(t) - \vec{A}^H(x)] + U(x)\} \qquad (\,3.22)$$

In this equation $\vec{A}(t)$ is the potential of time dependent electric field, $\vec{A}^H(x) = (\vec{A}^H(x), \vec{A}^H_y(x))$ is magnetic potential, and $U(x)$ is SE field.

3.6 Symmetry and symmetry breaking

As has been discussed, graphene has a filled valence band that touches an empty conduction band in six conical points, where Fermi energy lies with no gap energy. The gapless structure of graphene is not the reason of the unusual electrical properties but rather the chiral nature of the electron states and the high symmetry between electrons and holes, thus these quantities need to be conserved.

Since there are two sublattices per unit cell, at Dirac point two linear energy dispersions intersect as independent from each other, which result in the existence of pseudospin. The Dirac spinors are represented by the two sublattices, so "pseudospin-up" is sublattice A and "pseudospin-down" is sublattice B. However, it is actually a chiral pseudospin, which is a quantum number resulted from the lattice structure and is used to distinguish the electrons in the sublattices of graphene. Chirality connects electrons and holes in graphene so one can tell that they are originally form the same sublattice [5]. Considering the direction of motion $\vec{p}$ or $\vec{k}$, then the chirality in graphene the projection of electrons in positive (k state) and for holes is negative (-k state), except that: $\varepsilon(\vec{k}) \neq \varepsilon(-\vec{k})$ but rather $\varepsilon(\vec{k} + \vec{K}) = \varepsilon(-\vec{k} - \vec{K})$.

There are two more internal degrees of freedom in graphene: 1- isospin, which is the valley of the conical point K & K' usually represented by + and -, and 2-real spin, which is just the spin for Dirac fermions. The Hamiltonian of graphene is therefore represented by an 8×8 matrix that produces a dispersion energy that has threefold symmetry. In the Hamiltonian, $\vec{\sigma}$ refers to pseudospin of the quasiparticles rather than the real spin of electrons.

At the conical points, the zero gap state is symmetrical, thus it is time (T) symmetric and inversion (I) symmetric [63]. So the following conditions has to hold for the gapless state to be described as T and I invariant:

$$T: H_K = H_{K'}^* = H_K \qquad (3.23)$$

$$I: H_K = \sigma_x H_{K'} \sigma_x = H_K \qquad (3.24)$$

$$TI: H_K = \sigma_x H_K^* \sigma_x = H_K \qquad (3.25)$$

Then, if a perturbation, invariant for T and I, is applied to graphene it can cause some deformation to the spectrum such as shifting a conical point, but it cannot cause a gap opening as the sublattices remains equivalent. Consequently, to allow gap opening in the graphene, the inversion symmetry has to be broken.

Due to symmetry, different classes of topological semimetals have been described [64]. One type is the 3D Dirac semimetal is distinguished by its Dirac cone having a fourfold degeneracy. It emerges from twofold degeneracy of the time symmetry (T invariance) plus twofold degeneracy of the spatial inversion symmetry (P invariance). Another topological metal type is Weyl semimetals, which appears in the breaking of either symmetries (T or P). Thus, this type has a twofold degeneracy cones forming two Weyl points, which always appears in pairs. The pair hold two different topological charges +1 and -1, caused by the chirality of the Weyl fermions. Therefore, Weyl points form some kind of "magnetic" monopoles in momentum space.

3.7   Gap induction in graphene

Although graphene has properties with the potential to replace silicon in electronical applications, the zero-band gap structure stands as an obstacle. Graphene has a low on off ratio because of its energy band structure. Thus, gap opening problem in graphene is one of the most researched aspect of graphene. Studies and experiments aim to obtain a gap band without compromising graphene's properties. This section discusses some of the gap induction

techniques.

3.7.1 Deforming the honeycomb structure methods

3.7.1.1 Carbon nanotubes

The accidental discovery of Carbon nanotubes in 1991 has established a demanding research topic, as it is an essential part of the new generation of devices [55]. The physical properties of the nanotube, confined in very small structures remarkably, promises to provide a range of advanced applications. Perfect and pure nanotubes are more producible now with the achieved development of the synthesis techniques [56].
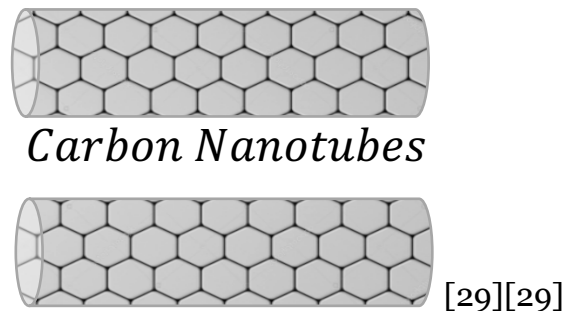
Figure 3.2 One-dimensional carbon nanotube

Carbon nanotubes are basically cylindrical tubes of graphene stripes with a very small radius (Figure 3.2). They can be produced to a significant length, and still considered a one-dimensional structure [57]. It can be fabricated with a monolayer graphene or multilayered, and the chiral index modifies the electronic band structure in the produces nanotubes. Hence the physical properties are determined by the structure, size and topology of nanotubes. Thus, nanotubes allow gap opening in the graphene band structure.

The energy gap in the nanotubes is proportional to the radius, which is determined by the boundary conditions of the graphene strips used in the formation. These boundary conditions will illustrate the conduction of the nanotubes, thus an armchair boundary conditions indicates conducting and semiconducting, while the zigzag boundary conditions only allow conduction behavior [56][58]. The energy states of the nanotubes are also specified by the

boundary conditions. Such simple basics is associated with the fact that the production volume is still below industrial limit with the amount of cost and techniques involved, in addition, the manipulation of nanostructure is still a challenging aspect [56]. Nevertheless, nanotubes are likely candidate for building graphene-based devices, such as transistors, where nanotubes works as efficient channels between the source and the drain [29].
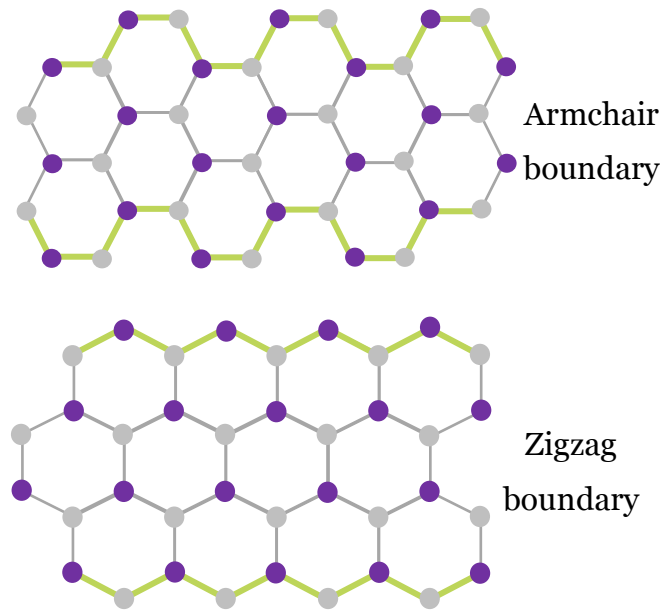
Figure 3.3 The edge of graphene nanoribbons determines the conduction behavior in the stripes.

3.7.1.2 Graphene nanoribbons

The graphene stripes with a very narrow width are called graphene nanoribbons. Nanoribbons can be fabricated simply by cutting carbon nanotubes longitudinally [29]. They are known to be a useful technique in creating an energy gap in graphene spectrum. Therefore, graphene would gain metallic properties or semiconducting properties depending on the structure of nanoribbons (the arm chair edge indicates a metallic and semiconducting behavior, and the zigzag edge indicates a metallic behavior only) (FIG 2.7) [37].

The size of the band gap in nanoribbons is influences by the width of the graphene sheet, the structure defects and the edges. Changing the width in practice requires high precision nanometers and nanofabrication; hence it can be hardly controlled. Moreover, the fabrication defects in the structure of the

sheet or in the uniformity of the edges is highly possible, therfore the manufacturing of nanoribbons devices still requires more developments [37]. Above all, the phonon scattering due to the defects or the edges of the nanoribbons cause a decrease in the mobility [29].

3.7.2 Structure preserving method

3.7.2.1 Substrate induced band gap opening

The isolation of graphene on an insulating substrate was reported on 2004, however gap opening in epitaxial graphene on hexagonal Boron Nitride (h-BN) was experimentally realized in 2002 [65]. This method was the first reported method in graphene gap opening allowing an energy gap of around 0.5 eV. Following up, a number of experiments achieved substrate induced band gap in graphene [66].

Recent theoretical research has been focusing on introducing energy gap to graphene on substrates such as h-BN, copper and SiO2. The minimum gap opening achieved was close to 0.1 meV and the maximum was around 0.52 eV. The studies were conducted to explore the validity of the substrate growth process or gate voltage application to preserve the semiconducting and semi-metallic features [67][68].

3.7.2.2 Superlattices gap opening

One of the greatest achievements in semiconductor physics is the work of Esaki and Tsu of superlattices[69]. Since then superlattices has been studied in depth and had influenced the field. Many phenomena have been determined by superlattices, such as "negative differential conductivity, Bloch oscillations, gap openings at the mini-Brillouin-zone boundary formed by the additional periodic potential and so on"[70]. The production of superlattices usually is based on metalorganic vapour phase epitaxy and molecular beam epitaxy [71]. For graphene, fabricating superlattices can be achieved either by:

1. impurities, which are positioned and aligned using or scanning tunnelling microscopy[72][73].

2. by epitaxial growth on top of a structured substrate [58].

3. by applying a local top- gate voltage to graphene [74][75]. The resulting material consists of two crystals aligned together, as a result the energy band structure of the materiel changes.

Graphene superlattices have gained a huge interest for theoretical physics, investigating to generate periodic potential or barrier structure using electrostatic and magnetic potentials[32][76][70][77][78][79][80][81][82]. One of the features of graphene superlattices is that in a 1D periodic potential superlattices the velocities of charge carriers show a strong anisotropy. Therefore, the charges mobile in one direction only with a constant velocity[70]. Such anisotropy results from formation of new Dirac points in the energy spectrum with new zero energy states. It has been shown that the emerged states can be controlled by altering the parameters of the periodic potentials [83][84]. Graphene superlattices have experimental realization. However, the fabrication tools and techniques are based on nanofabrication, which are of expensive cost, long fabrication time, and limited fabrication structures[85]. Therefore, theoretical periodic potential superlattices provides a promising tool with the features of superlattices.

In many researches, the investigation of charge carriers in graphene superlattices is based on calculating the energy dispersions, the group velocities and the energy-gap openings[70]. The massless charge carriers in graphene are described by Dirac equation, where the resulting energy dispersion near Dirac points is linear and isotropic[30][34][53][70][86][87]. Many models demonstrated that the wavefunction of the quasiparticles in graphene has two components represented by the two trigonal sublattices. Therefore, within the effective-Hamiltonian formalism, the two amplitudes can be represented by a spinor with two components and is called a pseudospin. This spinor results from the structure of the wavefunction and it is not related to the real spin or chirality. If an external periodic potential is applied to graphene, the spatial period of the superlattice potential is usually much larger than the nearest-neighbour distance between the carbon atoms in graphene $=\sim 1.42 \overset{\circ}{A}$. Consequently, there will not be a state scattering near Dirac points and hence no gap

opening[86][88][89].

The purpose of this research is to show that applying two different potentials to a SLG can create gap opening and furthermore, provides theoretically investigated analogies to graphene superlattices that are affordable and highly controlled.

3.8 Summary

Graphene band structure is different from other semiconductors. In graphene the energy is given by a linear dispersion in momentum due to the massless behavior of electrons at Dirac cones. The electrons travel freely between graphene atoms in light of Bloch's theory and the tight binding model. Around Dirac points represents the singularity of graphene, where electrons are considered Dirac fermions. Thus, Dirac Hamiltonian is used to describe the dynamics of electrons in graphene, which holds a number of symmetries. Therefore, inducing a gap in the energy spectrum of graphene requires symmetry breaking at Dirac points. Some of the gap inducing methods are based on deforming the honeycomb structure of graphene such as carbon nanotubes and carbon nanoribbons. These methods introduce scattering centers which reduces the electrons mobility in graphene. Other methods preserve the crystal structure of graphene for example, substrate gap opening and superlattices gap induction.

4 Theory

4.1 Massless Dirac fermions in graphene

From the previous chapter we can conclude that charge carriers in graphene can be considered massless Dirac fermions. They are identical particles with half integer spin, they have a very small mass, they obey Pauli exclusion principle, and they can be described with Fermi-Dirac statistic (in case of equilibrium). Therefore, an analogy between electron spectrum of graphene and Dirac fermions' spectra can be established [30].

There is a gap for research in optical properties of graphene. Respectively, there is an interest studying the electron behaviour of graphene in strong laser fields. Moreover, the symmetry in massless Dirac fermions needs to be investigated more, in different periodic fields (electric and magnetic). In the case of special periodic potentials, the energy spectrum $\varepsilon(\vec{k})$ splits into a number of subbands. This happens when the potential has a special period larger than interatomic distances. The electron waves are then reflected by such potentials and due to constructive interference, the electron spectrum is split with gaps. This reflection and interference do not occur in the case of time periodic potential [41]. However, a change in the electron energy spectrum can occur. Floquet theory can be used to analyse and control such a change in time-periodic potential systems. In this chapter we describe the basic approach to our study.

4.2 Floquet theory

Floquet theory is a branch of the theory of ordinary differential equations relating to the class of solutions to periodic linear differential equations analogues to Bloch theory. Floquet theory plays an essential role in analysing dynamical systems. Using the theory, periodic systems can be transformed to linear forms.

Floquet theory can be used to solve the time dependent Schrödinger equation:

$$i \frac{\partial}{\partial t} \Psi(x,t) = \widehat{H}(t)\Psi(x,t) \qquad (4.1)$$

Floquet theory illustrates that time periodic potentials transfers the electron's energy into a quasi-energy confined within its Brillouin zone $(-\frac{\pi}{T} < \varepsilon < \frac{\pi}{T})$, where, T is the time period of the spatially homogenous field. Therefore, Floquet theory gives a solution of the form:

$$\Psi(x,t) = e^{-i\varepsilon t} \Phi(x,t) \qquad (4.2)$$

where $\Phi(x,t) = \Phi(x,t+T)$, and ε is the quasienergy or Floquet energy.

The initial energy spectrum splits into several subbands (Floquet Bloch bands) [30][90]. These changes enlighten the possibility of "gapping" in quasiparticles[43].

The analogy between graphene in spatial periodic fields and time periodic fields can be explained from a mathematical perspective by Floquet theory as it forms a linear differential equation as [42]:

$$\dot{x} = M(t)x \qquad (4.3)$$

where, $M(t)$ is a $n \times n$ with a period of T piecewise continues function,

x is a column vector of length n, however, no need to be periodic but has to be of the form: $x = e^{\mu t}J(t)$. Where, $J(t)$ is periodic in T and μ is of nth order. Therefore, the wave functions $\Phi(x,t)$ should also be a solution to Schrödinger equation:

$$\hat{H}(t)\, \Phi(x,t) = \varepsilon\, \Phi(x,t) \qquad\qquad (4.4)$$

where $\Phi(x,t)$ can be expanded as [10]:

$$\Phi(x,t) = \sum_{n=-\infty}^{\infty} \varphi_n(x)e^{-in\omega t} \qquad\qquad (4.5)$$

Using resonance approximation [91] this solution can be expanded with exclusion of high frequencies. The resonance effect results from the rate of change in the subsystem–reservoir interaction modes. Since it is not possible to accurately calculate the frequency and the lifetime of the resonance, the associated eigenfunctions cannot be accurately determined. Thus, an approximation of the eigenstates is considered [92].

4.3 2D-Dirac Hamiltonian

Graphene is a zero-gap semiconductor, with low-energies quasiparticles that can be describes by Dirac Hamiltonian in equation (3.22). The lattice of graphene is a hexagonal lattice (honeycomb lattice) that is made up of two sublattices referred to as sublattice A and sublattice B. Both equivalent sublattices are associated with cosine-like energy bands that intersect at zero near the boundaries of Brillouin zones. Therefore, the energy spectrum in graphene forms two canonical sections where the charged carriers' are in motion which is described by 2D Dirac equation [5]:

$$\left\{\vec{\sigma}.\left[\vec{p} - \vec{A}(t) - \vec{A}^H(x)\right] + U(x)\right\}\psi_{A,B} = i\, \partial\psi_{A,B}/\partial t \qquad\qquad (4.6)$$

We will consider the units $e = \hbar = v_F = 1$, where $\vec{A}(t)$ is the potential of time dependent electric field, $\vec{A}^H(x) = (\vec{A}^H(x), \vec{A}_y^H(x))$ is the magnetic potential, and $U(x)$ is the static electric field. The special periodic electro-static potential $U(x)$, or the vector magneto-static potential $A^H(x)$, each should have large periods in respect interatomic distance.

The electron wave function ψ is represented by two components ψ_A and ψ_B, referring to the electrons in the two triangular sublattices A and B.

$$\psi = \begin{pmatrix} \psi_A \\ \psi_B \end{pmatrix} \tag{4.7}$$

Substituting a solution of the wavefunction using Floquet theory eq. (3.6) [93] and the potentials, then by rearranging and cancelling high harmonics terms, we end up with an equation of the form:

$$M \begin{bmatrix} \psi_A^{++} \\ \psi_B^{++} \\ \psi_A^{+-} \\ \psi_B^{+-} \\ \psi_A^{-+} \\ \psi_B^{-+} \\ \psi_A^{--} \\ \psi_B^{--} \end{bmatrix} = \varepsilon \begin{bmatrix} \psi_A^{++} \\ \psi_B^{++} \\ \psi_A^{+-} \\ \psi_B^{+-} \\ \psi_A^{-+} \\ \psi_B^{-+} \\ \psi_A^{--} \\ \psi_B^{--} \end{bmatrix} \tag{4.8}$$

Equation (4.14) can be solved for $\varepsilon(k_x, k_y)$ numerically or analytically if high oscillation terms are neglected. The matrix M can be represented by a general form as a solution to the 2D equation as the following matrix:

$$\begin{vmatrix}
\frac{\omega}{2} & k + Cf & C_n U_0 & iC_m A_0^H & 0 & -\left(\frac{A_0}{2}\right)e^{-i\theta} & 0 & 0 \\
k^* + Cf & \frac{\omega}{2} & -iC_m A_0^H & C_n U_0 & -\left(\frac{A_0}{2}\right)e^{i\theta} & 0 & 0 & 0 \\
C_n U_0 & iC_m A_0^H & \frac{\omega}{2} & k + Cf & 0 & 0 & 0 & -\left(\frac{A_0}{2}\right)e^{-i\theta} \\
-iC_m A_0^H & C_n U_0 & k^* + Cf & \frac{\omega}{2} & 0 & 0 & -\left(\frac{A_0}{2}\right)e^{i\theta} & 0 \\
0 & -\left(\frac{A_0}{2}\right)e^{-i\theta} & 0 & 0 & \frac{-\omega}{2} & k + Cf & C_n U_0 & iC_m A_0^H \\
-\left(\frac{A_0}{2}\right)e^{i\theta} & 0 & 0 & 0 & k^* + Cf & \frac{-\omega}{2} & -iC_m A_0^H & C_n U_0 \\
0 & 0 & 0 & -\left(\frac{A_0}{2}\right)e^{-i\theta} & C_n U_0 & iC_m A_0^H & \frac{-\omega}{2} & k + Cf \\
0 & 0 & -\left(\frac{A_0}{2}\right)e^{i\theta} & 0 & -iC_m A_0^H & C_n U_0 & k^* + Cf & \frac{-\omega}{2}
\end{vmatrix} \tag{4.9}$$

where $k = k_x - ik_y$, hence, $k^* = k_x + ik_y$, C, C_n & C_m are constants that can be determined by the initial conditions, A_0^H is the amplitude of the magnetic potential, U_0 is the amplitude of the electric potential, $f = \mu$ or k_0 is the frequency of the applied potential, A_0 is the laser amplitude which in the case of circularly polarised laser will be multiplied in the matrix by $(1 \pm ie^{i\varphi})$, ω is the laser frequency, and θ is the angle between the laser and the applied field.

4.4 Summary

Charge carriers in graphene are treated as massless Dirac fermions, which are described by the 2D Dirac equation. Block theory allows the use of Floquet theory to obtain a linear solution for Schrodinger's equation. Then the resonance approximation can be used to obtain the dynamical behaviour and energy spectrum in graphene from the solution of Dirac Hamiltonian.

5 Graphene in Laser Field

5.1 Energy spectrum in periodic potential

The study of electron transport in graphene devices is usually approached by studying graphene superlattices. In addition, they allow for electron spectra manipulation. Yet, the nanofabrication of graphene superlattices is of a high cost and does not provide a perfect tunability in modifying electron spectra. Therefore, an analogy was found between electron spectra in graphene superlattices and Dirac-fermions spectra in laser field [30]. The application of laser fields to semiconducting lattices, such as graphene, creates a band gap structure in electron spectra. Moreover, such an effect can be easily controlled. The laser fields create a Strack effect in the energy band structure, causing the gap creation [30]. Applying different laser frequency or amplitude changes the size and location of the gap in the semiconductor. This is promising in term of obtaining spectra in graphene, in each time-dependent or spatial-dependent potential. Moreover, provides an analogy to spectra in graphene superlattices [30].

The next section will show the problem of analytically finding the electron spectrum in graphene in both linearly and circularly polarised laser fields (LPL & CPL) based on the work done by Savel's and Alexandrov [30]. Then we will apply

the same calculation approach the problem of electron spectrum in graphene in SE field.

The aim of this chapter is to establish the approach to the problems of finding the energy spectrum of the electrons in graphene using the 2D Dirac equation (3.6), which describes the electrons' motions in 2D graphene lattice.

5.2 Graphene in time periodic laser field

5.2.1 Graphene in linearly polarised laser field LPL

In the application of LPL field, we will only consider the electric potential, as the magnetic field is negligible. Hence, we will consider $U(x) = 0$, $\vec{A}^H = 0$, and the laser time-periodic electric field is $E_x(t) = -\frac{dA_x}{dx}$ and $E_y(t) = -\frac{dA_y}{dt}$. In the case of LPL, the potential can be of the form [30]:

$$A_x(t) = A_0 \cos(\omega t) \quad \& \quad A_y(t) = 0 \qquad (5.1)$$

The frequency of the harmonic field is known to be of the form: $\omega = \frac{2\pi}{T}$, and the electron wave function can be written as two functions [30]:

$$\psi_{A,B} = \phi_{A,B}(t) \exp(ik_x x + ik_y y) \qquad (5.2)$$

The function $\phi_{A,B}(t)$ only depends on time. Subsitiuting the wave function and the potential into the 2D Dirac equation (4.6), we obtain the differential equation:

$$i\frac{d}{dt}\begin{pmatrix}\phi_A\\\phi_B\end{pmatrix} = \begin{pmatrix} 0 & (k_x - A_x(t)) - i\left(k_y - A_y(t)\right) \\ (k_x - A_x(t)) + i\left(k_y - A_y(t)\right) & 0 \end{pmatrix}\begin{pmatrix}\phi_A\\\phi_B\end{pmatrix} \qquad (5.3)$$

$A_x(t)$ can be rewritten as:

$$A_x(t) = A_0\left(e^{i\omega t} + e^{-i\omega t}\right) \qquad (5.4)$$

This is an ordinary differential equation, of the form: $\dot{x} = M(t)x$. Hence, we can use Floquet theory to find the solution. The 2×2 matrix is: (i) periodic in T (as $A_x(t) = A_0 \cos(\omega t)$ and $\omega = \frac{2\pi}{T}$), (ii) piecewise continues function (as $A(t) = \begin{pmatrix} A_x \\ A_y \end{pmatrix}$) . On the other hand, $\phi_{A,B}$ has to be of the form $e^{\mu t}J(t)$. Therefore, we can consider a general standing wave oscillating in a quantum system travelling through a harmonic potential (resonance approximation [30]):

$$\phi_{A,B}(t) = e^{i\varepsilon t}\left(D^+_{A,B}\, e^{\frac{i\omega t}{2}} + D^-_{A,B}\, e^{\frac{-i\omega t}{2}} + D^+_{A,B}\, e^{\frac{3i\omega t}{2}} + D^-_{A,B}\, e^{\frac{-3i\omega t}{2}} \dots \dots \right) \qquad (5.5)$$

where, D^+_A, D^+_B, D^-_A and D^-_B are four variables associated with the waves travelling direction ($e^{\frac{i\omega t}{2}}$ to the right and $e^{\frac{-i\omega t}{2}}$ to the left).

To find an analytical solution we ignore all terms with fast oscillations which are all terms with $n > \pm 1$ (e.g. $e^{\frac{\pm 3i\omega t}{2}}, e^{\frac{\pm 5i\omega t}{2}} \dots$), therefore,

$$\phi_{A,B}(t) = e^{i\varepsilon t}\left(D^+_{A,B}\, e^{\frac{i\omega t}{2}} + D^-_{A,B}\, e^{\frac{-i\omega t}{2}} \right) \qquad (5.6)$$

Substituting (5.4) and (5.6) that into equation (5.3) we will obtain four equations such as:

$$D^+_A\left(\frac{\omega}{2} - \varepsilon\right) + D^+_B\left(-(k_x - ik_y)\right) + D^-_A(0) + D^-_B\left(\frac{A_0}{2}\right) = 0 \qquad (5.7)$$

$$D^+_A(0) + D^+_B\left(\frac{A_0}{2}\right) + D^-_A\left(\frac{\omega}{2} - \varepsilon\right) + D^-_B\left(-(k_x - ik_y)\right) = 0 \qquad (5.8)$$

$$D^+_A\left(-(k_x + ik_y)\right) + D^+_B\left(-\frac{\omega}{2} - \varepsilon\right) + D^-_A\left(\frac{A_0}{2}\right) + D^-_B(0) = 0 \qquad (5.9)$$

$$D^+_A\left(\frac{A_0}{2}\right) + D^+_B\left(-\frac{\omega}{2} - \varepsilon\right) + D^-_A\left(-(k_x + ik_y)\right) + D^-_B\left(\frac{\omega}{2} - \varepsilon\right) = 0 \qquad (5.10)$$

46

We can combine these four equations to produce a four by four matrix L:

$$\begin{bmatrix} -\omega/2 & -(k_x - ik_y) & 0 & A_0/2 \\ -(k_x + ik_y) & -\omega/2 & A_0/2 & 0 \\ 0 & A_0/2 & \omega/2 & -(k_x - ik_y) \\ A_0/2 & 0 & -(k_x + ik_y) & \omega/2 \end{bmatrix} \begin{bmatrix} D_A^+ \\ D_B^+ \\ D_A^- \\ D_B^- \end{bmatrix} = \varepsilon \begin{bmatrix} D_A^+ \\ D_B^+ \\ D_A^- \\ D_B^- \end{bmatrix} \qquad (5.11)$$

This is simply an eigen value problem that can be solved by setting the determinant equal to zero:

$$\det[L - \varepsilon] = 0 \qquad (5.12)$$

Therefore [30],

$$\varepsilon = \pm \sqrt{\frac{\omega^2 + A_0^2}{4} + k^2 \pm \sqrt{k^2 \omega^2 + A_0^2 k_x^2}} \qquad (5.13)$$

where $k^2 = k_x^2 + k_y^2$ and A_0 can be defined at t=0.

Taking each sign at a time ($\pm$ inside and outside the square root), this equation will produce four energy spectra (FIG 5.1).

The given spectra (FIG 5.1 & 5.2) show two upper bands representing the hole states and two lower bands for the electron states. The spectrum shows 2 Dirac points along the k_x axis where the cones change size with different laser parameters without a gap opening at any case.

(a)

(b)

(c)
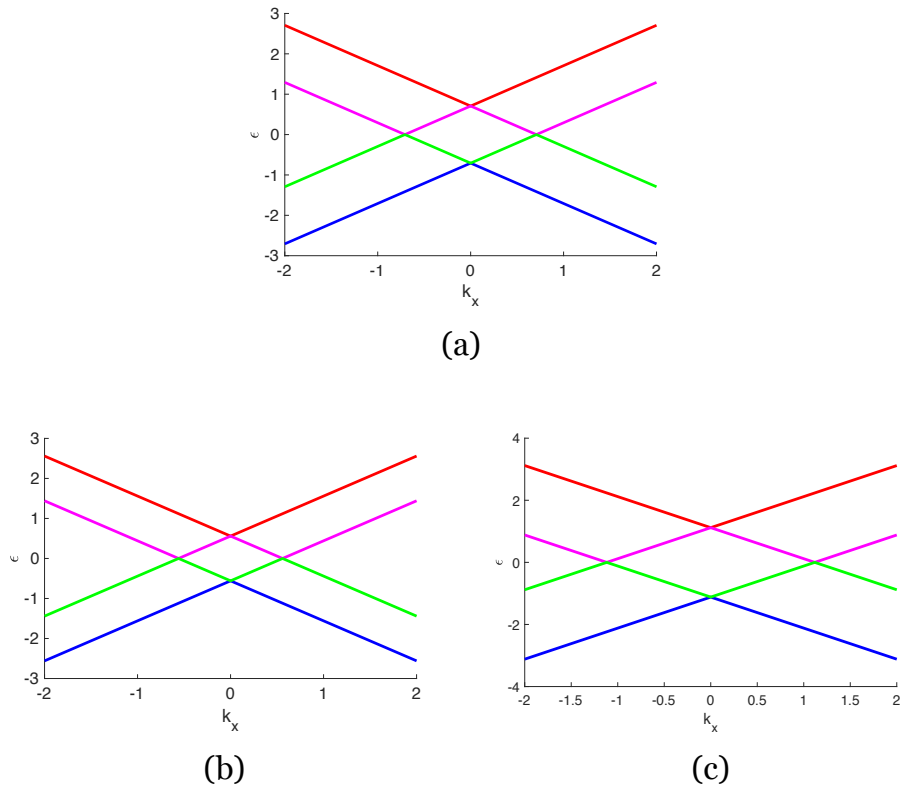
Figure 5.1 2D Electron spectra for SLG $\varepsilon(k_x, k_y)$ in LPL fields with units of π/T considering (a) $\omega = 1$ and $A_0 = 1$ (a) showing the gapless spectra at ($k_y = 0$) where the hole states in the upper bands and electron states in the lower bands have no gap, the figure shows that changing the laser parameter only affect the size of the cone however does not allow a gap opening (b) $\omega = 0.5$ or $A_0 = 0.5$ (c) $\omega = 1.5$ or $A_0 = 1.5$.
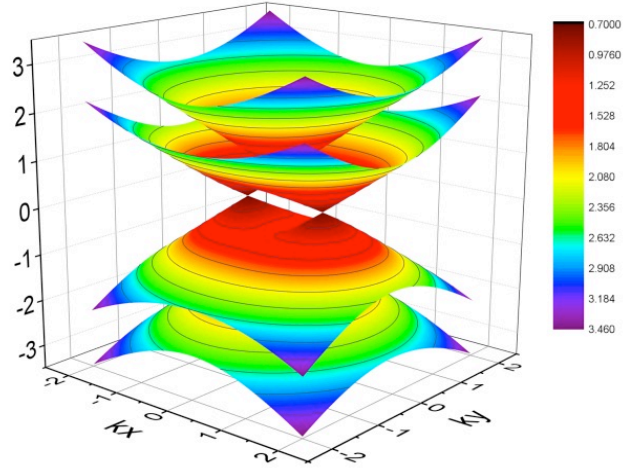
(a)
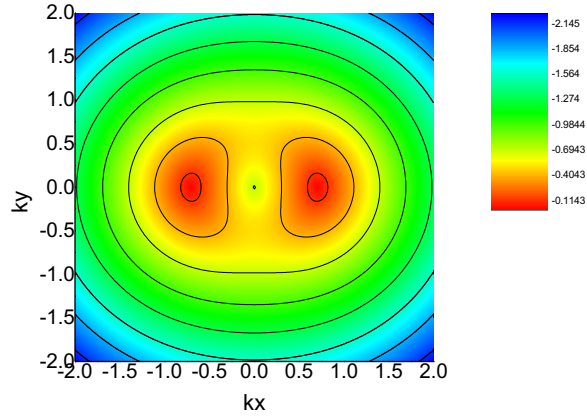
(b)

Figure 5.2 $\varepsilon(k_x, k_y)$ in 3D plot for SLG in LPL field (a) the upper bands are hole states and the lower bands are electron states touching in 2 Dirac points with no gap opening (b) showing the two Dirac cones to be ellipses near with single Dirac points for each cone ($\omega = 1$ and $A_0 = 1$ in units of π/T).

5.2.2 Graphene in circularly polarised laser field CPL

Applying a CPL field will result in a duality between the electrical and the magnetic field hence it cannot be neglected. Therefore, we will consider a laser field that is arbitrary polarised [62]:

$$A_x(t) = \left(\tfrac{A_0}{\sqrt{2}}\right)\cos(\omega t) \text{ and } A_y(t) = \left(\tfrac{A_0}{\sqrt{2}}\right)\cos(\omega t + \varphi) \tag{5.14}$$

$$\text{or } A_x(t) = \left(\tfrac{A_0}{2\sqrt{2}}\right)\left(e^{i\omega t} + e^{-i\omega t}\right) \text{ and } A_y(t) = \left(\tfrac{A_0}{2\sqrt{2}}\right)\left(e^{i(\omega t + \varphi)} + e^{-i(\omega t + \varphi)}\right), \tag{5.15}$$

$$A_x(t) = \beta\left(e^{i\omega t} + e^{-i\omega t}\right) \text{ and } A_y(t) = \beta\left(e^{i(\omega t + \varphi)} + e^{-i(\omega t + \varphi)}\right) \tag{5.16}$$

where $\beta = \tfrac{A_0}{2\sqrt{2}}$ Then, by using the same $\phi_{A,B}(t)$ as in equation (5.7) and the same approach from the previous calculation we will find:

$$\begin{bmatrix} -\omega/2 & -k_x + ik_y & 0 & \beta - i\beta e^{i\varphi} \\ -k_x - ik_y & -\omega/2 & \beta + i\beta e^{i\varphi} & 0 \\ 0 & \beta - i\beta e^{-i\varphi} & \omega/2 & -k_x + ik_y \\ \beta + i\beta e^{-i\varphi} & 0 & -k_x - ik_y & \omega/2 \end{bmatrix} \begin{bmatrix} D_A^+ \\ D_B^+ \\ D_A^- \\ D_B^- \end{bmatrix} = \varepsilon \begin{bmatrix} D_A^+ \\ D_B^+ \\ D_A^- \\ D_B^- \end{bmatrix} \tag{5.17}$$

If the determinate is set equal to zero, then we will find:

$$\varepsilon = \pm \sqrt{\frac{\omega^2 + A_0^2}{4} + k^2 \pm \sqrt{k^2\left(\omega^2 + \frac{A_0^2}{2}\right) + S(\varphi)}} \tag{5.18}$$

where $S(\varphi) = A_0^4 \sin^2\left(\tfrac{\varphi}{16}\right) + A_0^2 k_x k_y \cos(\varphi)$. FIG 4.3 shows the energy spectrum at a chosen phase shift φ.
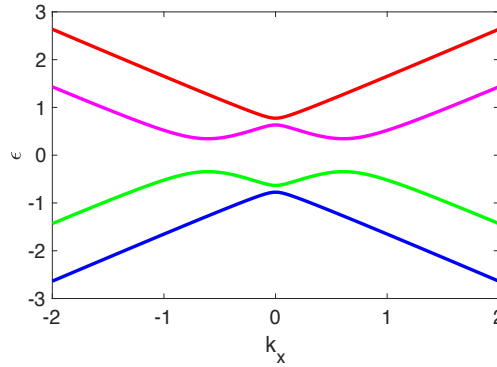
Figure 5.3 2D Electron spectra for SLG $\varepsilon(k_x, k_y)$ in CPL fields for a chosen phase shift $\varphi = \pi/2$ with units of π/T, considering (a) $\omega = 1$ and $A_0 = 1$, showing the gapped band structure at $k_y = 0$, where the hole states in the upper bands and electron states in the lower bands with no gap.

<div align="center">(a)   (b)</div>
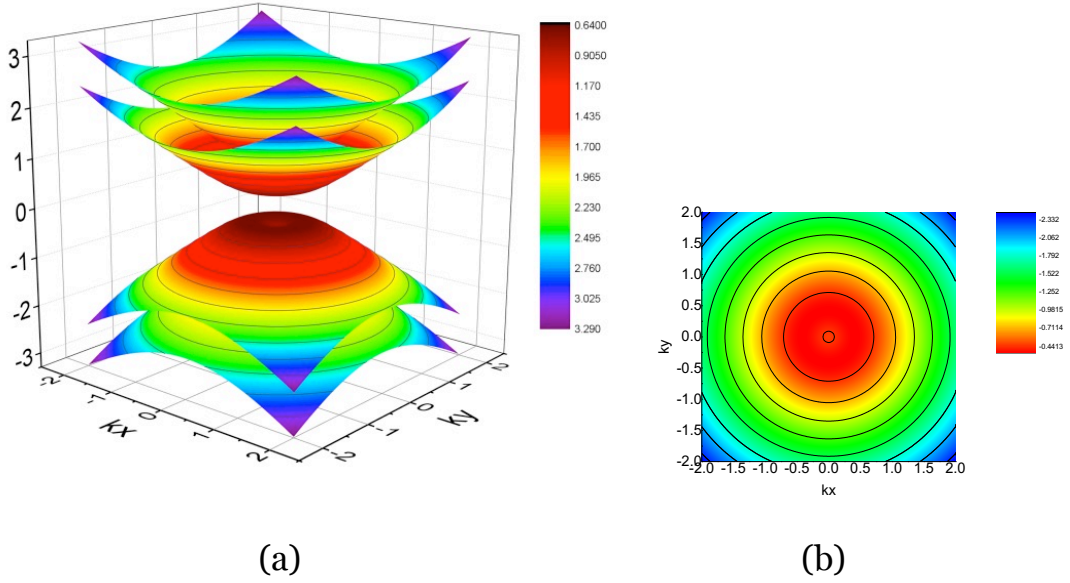
Figure 5.4 $\varepsilon(k_x, k_y)$ in 3D plot for SLG in CPL field for a chosen phase shift $\varphi = \pi/2$, where the upper bands are hole states and the lower bands are electron states with a gap opening in between (b) showing the spectrum to form a single circular structure ($\omega = 1$ and $A_0 = 1$ in units of π/T).

The spectrum forms a gapped structure where the conduction and the valence bands are in off state. Changing the laser parameters does not allow a touching point. As the laser in this case is circularly polarised, it combines two types of potentials: electrostatic and magnetostatic. This combination allows quasi-isotropic gap in the energy spectrum [5][9].

The solution function $\phi_{A,B}(t)$ (eq. 5.7), can be expanded to higher terms like of the order with $n > \pm 3$, so:

$$\phi_{A,B}(t) = e^{-i\varepsilon t}\left(D_{A,B}^{++}\, e^{\frac{3i\omega t}{2}} + D_{A,B}^{+-}\, e^{\frac{i\omega t}{2}} + D_{A,B}^{-+}\, e^{\frac{-i\omega t}{2}} + D_{A,B}^{--}\, e^{\frac{-3i\omega t}{2}} \right) \quad (5.19)$$

Such consideration will give a bigger matrix. In the LPL application the matrix is of the following form:

<div align="center">51</div>

$$
\begin{pmatrix}
\frac{3\omega}{2} & k_x - i k_y & 0 & \frac{-A_0}{2} & 0 & 0 & 0 & 0 \\
k_x + i k_y & \frac{3\omega}{2} & \frac{-A_0}{2} & 0 & 0 & 0 & 0 & 0 \\
0 & \frac{-A_0}{2} & \frac{\omega}{2} & k_x - i k_y & 0 & \frac{-A_0}{2} & 0 & 0 \\
\frac{-A_0}{2} & 0 & k_x + i k_y & \frac{\omega}{2} & \frac{-A_0}{2} & 0 & 0 & 0 \\
0 & 0 & 0 & \frac{-A_0}{2} & \frac{-\omega}{2} & k_x - i k_y & 0 & \frac{-A_0}{2} \\
0 & 0 & \frac{-A_0}{2} & 0 & k_x + i k_y & \frac{-\omega}{2} & \frac{-A_0}{2} & 0 \\
0 & 0 & 0 & 0 & 0 & \frac{-A_0}{2} & \frac{-3\omega}{2} & k_x - i k_y \\
0 & 0 & 0 & 0 & \frac{-A_0}{2} & 0 & k_x + i k_y & \frac{-3\omega}{2}
\end{pmatrix}
\tag{5.20}
$$

While in the application of the CPL filed the matrix is given by:

$$
\begin{pmatrix}
\frac{3\omega}{2} & k_x - i k_y & 0 & \frac{-A_0}{2\sqrt{2}}(1 - ie^{i\varphi}) & 0 & 0 & 0 & 0 \\
k_x + i k_y & \frac{3\omega}{2} & \frac{-A_0}{2\sqrt{2}}(1 + ie^{i\varphi}) & 0 & 0 & 0 & 0 & 0 \\
0 & \frac{-A_0}{2\sqrt{2}}(1 - ie^{-i\varphi}) & \frac{\omega}{2} & k_x - i k_y & 0 & \frac{-A_0}{2\sqrt{2}}(1 - ie^{i\varphi}) & 0 & 0 \\
\frac{-A_0}{2\sqrt{2}}(1 + ie^{-i\varphi}) & 0 & k_x + i k_y & \frac{\omega}{2} & \frac{-A_0}{2\sqrt{2}}(1 + ie^{i\varphi}) & 0 & 0 & 0 \\
0 & 0 & 0 & \frac{-A_0}{2\sqrt{2}}(1 - ie^{-i\varphi}) & \frac{-\omega}{2} & k_x - i k_y & 0 & \frac{-A_0}{2\sqrt{2}}(1 - ie^{i\varphi}) \\
0 & 0 & \frac{-A_0}{2\sqrt{2}}(1 + ie^{-i\varphi}) & 0 & k_x + i k_y & \frac{-\omega}{2} & \frac{-A_0}{2\sqrt{2}}(1 + ie^{i\varphi}) & 0 \\
0 & 0 & 0 & 0 & 0 & \frac{-A_0}{2\sqrt{2}}(1 - ie^{-i\varphi}) & \frac{-3\omega}{2} & k_x - i k_y \\
0 & 0 & 0 & 0 & \frac{-A_0}{2\sqrt{2}}(1 + ie^{-i\varphi}) & 0 & k_x + i k_y & \frac{-3\omega}{2}
\end{pmatrix}
\tag{5.21}
$$

The eigen-energies given by the determinant of (5.20) & (5.21) show a repeated periodic structure in the energy spectrum (FIG 5.5).

(a)   (b)
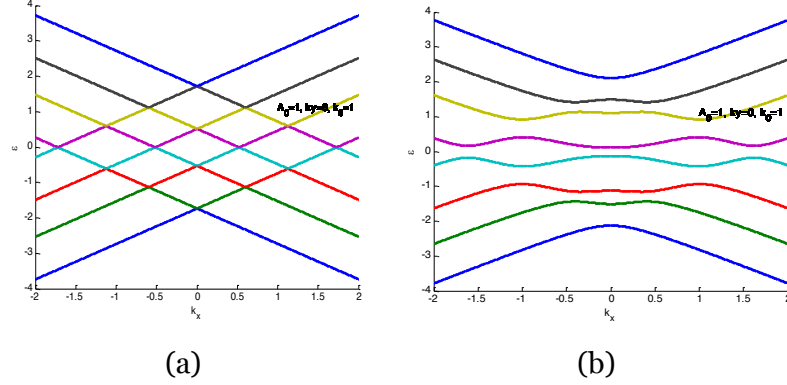
Figure 5.5 2D Electron spectra for graphene in laser fields with units of π/T considering $\omega = 1$ and $A_0 = 1$ for a higher approximation for Floquet waves (a) Electron spectrum for graphene in LPL ($k_y = 0$). $\varepsilon(k_x, k_y)$ shows the hole states in the upper bands and electron states in the lower bands with no gap. (b) The energy spectrum for graphene in CPL field with phase shift $\varphi = \pi/2$. The spectrum has a gap band at all laser parameters.

5.3 Graphene in spatially periodic field

In this part, we will apply a spatially periodic potential to a graphene lattice. We will consider a static potential of the form:

$$U(x) = U_0 \cos(k_0 x) \tag{5.22}$$

Considering $A(t) = (A_x, A_y) = 0$ and $A^H(x) = 0$, with a wavefunction of the form:

$$\psi = \begin{pmatrix} \psi_A \\ \psi_B \end{pmatrix} = \begin{pmatrix} \phi_A(t) \\ \phi_B(t) \end{pmatrix} e^{ik_x x + ik_y y} \tag{5.23}$$

We substituted (5.22) and (5.23) into the 2D Dirac equation (4.6), and hence obtained:

$$\begin{pmatrix} U_0 \cos(k_0 x) & -i(\partial/\partial x) - \partial/\partial y \\ -i(\partial/\partial x) + \partial/\partial y & U_0 \cos(k_0 x) \end{pmatrix} \begin{pmatrix} \phi_A \\ \phi_B \end{pmatrix} = i\frac{d}{dt}\begin{pmatrix} \phi_A \\ \phi_B \end{pmatrix} \tag{5.24}$$

To obtain a solution, we use Bloch wave function and resonance approximation to find the electron energy spectrum [64]:

$$\phi_{A,B} = e^{i\varepsilon t + i k_x x + i k_y y}\left(\psi_{A,B}^+ \, e^{\frac{i k_0 x}{2}} + \psi_{A,B}^- e^{\frac{i k_0 x}{2}}\right) \qquad (5.25)$$

where, ψ_A^+ is a component of the electron wave function, resembles the sublattice A and the direction $+$.

From there, we will have four equations that can be represented by the matrix equation:

$$\begin{bmatrix} 0 & \left(k_x - k_y + \frac{k_0}{2}\right) & \frac{U_0}{2} & 0 \\ \left(k_x + k_y + \frac{k_0}{2}\right) & 0 & 0 & \frac{U_0}{2} \\ \frac{U_0}{2} & 0 & 0 & \left(k_x - k_y - \frac{k_0}{2}\right) \\ 0 & \frac{U_0}{2} & \left(k_x + k_y - \frac{k_0}{2}\right) & 0 \end{bmatrix} \begin{bmatrix} \psi_A^+ \\ \psi_B^+ \\ \psi_A^- \\ \psi_B^- \end{bmatrix} = \varepsilon \begin{bmatrix} \psi_A^+ \\ \psi_B^+ \\ \psi_A^- \\ \psi_B^- \end{bmatrix} \qquad (5.26)$$

Solving this as an eigenvalue problem gives an energy spectrum of the form:

$$\varepsilon = \pm\sqrt{k^2 + \frac{k_0^2 + U_0^2}{4} \pm \sqrt{k_x^2 k_0^2 + k^2 U_0 - \frac{3k_0^2 U_0^2}{8}}} \qquad (5.27)$$

The spectra of the SLG at $k_y = 0$, shows gapless Dirac cones (Figure 5.6). Applying the SE filed with different frequency or different amplitude does not introduce a gap in the band structure.
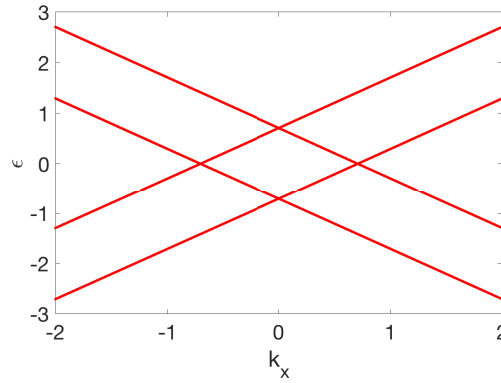
Figure 5.6 $\varepsilon(k_x, k_y)$ for SLG in a SE field shows gapless Dirac cones considering $\omega = 1$, $A_0 = 1$, $k_0 = 1$ and $U_0 = 1$ at $k_y = 0$

In BLG, the method of applying a vertical-external electric field has been found to be one of the most effective theoretical and experimental methods, which preserve the graphene's structure and thus the electrons' mobility, and results in a gap opening in the spectrum. The vertical electric field breaks the symmetry inversion and can introduce a tunable gap up to 0.25 eV in BLG[17]. However, applying the same method to SLG does not result in an energy gap formation because the two sublattices in the monolayer structure remain equivalent [17].

5.4 Summary

We investigated the gap opening in SLG in three cases; 1-lineraly polarised laser LPL, 2- circularly polarised laser CPL, and 3- static electric field SE. A general conclusion has been drawn from the investigation in the application of the laser field. The polarization of the laser determines the gap opening in the graphene spectrum.

In the application of laser field, the polarization of the laser is found to be the key difference to the gapped band structure. The LPL produces an anisotropic gapless energy spectrum [81], however permits an alteration to Dirac's cone shape and Dirac points positions. In contrast, the CPL field produces a graphene spectrum with a wide isotropic gap [30].

The obvious limitation of both cases are that each case allows only one option of gap structure without providing the transfer form gapless to gapped spectrum (and vice versa). So, it has been demonstrated theoretically that applying a laser field (an electromagnetic field) to graphene produces a band structure that depends on the polarization of the applied filed.

6 Electron States in Magnetic Field

6.1 The effective Hamiltonian of graphene in magnetic field

The application of quantized magnetic fields to graphene has allowed the realisation of massless Dirac fermions and the discovery of anomalous QHE [31][41]. This section provides a brief introduction to graphene's electrical properties in magnetic field. Next it theoretically examines SLG in time periodic magnetic field, and then SLG in static magnetic field with the application of linearly polarised laser to draw a conclusion.

In massless Dirac fermions, if a uniform magnetic field B is applied then the fermions will have eigen energies of [41]:

$$E_n^{\pm} = \pm\hbar\omega_c\sqrt{n} \qquad\qquad (6.1)$$

where, ω_c is the cyclotron frequency $= \frac{|e|B}{mc}$ and $n = 0,1,2\ldots$

This results in a number of levels, which is referred to as Landau levels. They are known to be the discrete energy of electron moving in two dimensions under the application of magnetic field [94].

In graphene, if a magnetic field is applied to the crystal, then $\boldsymbol{B}$ usually have a magnetic length l_B much larger than the interatomic distance a, where $l_B = \sqrt{\frac{\hbar c}{|e| \boldsymbol{B}}}$. Generally only π electrons are taken into consideration while looking at the transition of carriers in graphene, with the assumption that there is no hopping within each sublattices, hence, no crossing between electrons A and electrons B. Therefore, the effective Hamiltonian is taken with respect of the hopping parameter $\boldsymbol{t}$ [41]:

$$\widehat{H}_{eff} = \boldsymbol{t}(\hat{\pi}) \tag{6.2}$$

The operator $\hat{\pi}$ can be found in the original Hamiltonian of a magnetic field applying on Bloch states [41]:

$$\widehat{H} = \frac{\hat{\pi}^2}{2m} + V(\vec{r}) \tag{6.3}$$

Thus,

$$\hat{\pi}^2 = \hat{p} - \frac{e}{c}\vec{A} \tag{6.4}$$

The operator can be represented as [41]:

$$\hat{\pi}_- = \hat{\pi}_x - i\,\hat{\pi}_y \qquad \text{and} \qquad \hat{\pi}_+ = \hat{\pi}_x + i\,\hat{\pi}_y \tag{6.5}$$

$$\text{where,} \left[\hat{\pi}_x, \hat{\pi}_y\right] = -\left[\hat{\pi}_y, \hat{\pi}_x\right] = \frac{ie}{\hbar c}\boldsymbol{B} \tag{6.6}$$

The effective Hamiltonian then can be found to be of the form [41]:

$$H = v_F \begin{pmatrix} 0 & \hat{\pi}_- \\ \hat{\pi}_+ & 0 \end{pmatrix} \tag{6.7}$$

The application of a magnetic field alone does not affect the symmetry of graphene lattice between electron states and hole states. However, in the case of high magnetic fields, an energy gap can be formed within Landau levels due to either: (i) spin splitting; or (ii) sublattice symmetry breaking, where the introduced gap is either a consequence of magnetic interaction or many-body entanglement [94] [95]. In general, magnetic field causes a shift to the Landau levels [94].

6.2 Graphene in a time-periodic magnetic field

The same approach again can be used in the case of time periodic magnetic potentials in x and y given as:

$$A_x^H(x) = A_0^H \cos(\theta) \cos(\omega t) \quad , A_y^H(x) = A_0^H \sin(\theta) \cos(\omega t) \quad (6.8)$$

In this case, we can seek a solution of the form:

$$\Psi_{A,B} = e^{e^{i\varepsilon t + ik_x x + ik_y y}} \left(\psi_{A,B}^{++} e^{\frac{3i\omega t}{2}} + \psi_{A,B}^{+-} e^{\frac{i\omega t}{2}} + \psi_{A,B}^{-+} e^{\frac{-i\omega t}{2}} + \psi_{A,B}^{--} e^{\frac{-3i\omega t}{2}} \right) \quad (6.9)$$

Applying the potential along two axes in equation (4.6) make finding an analytical solution for the energy spectrum more complicated, however, a numerical solution has been found in (Figure 6.1) as the determinant of the following 8 by 8 matrix:

$$\begin{pmatrix}
-\dfrac{3\omega}{2} & -k_x+ik_y & 0 & \dfrac{A_0^H}{2}e^{-i\theta} & 0 & 0 & 0 & 0 \\
-k_x-ik_y & -\dfrac{3\omega}{2} & \dfrac{A_0^H}{2}e^{i\theta} & 0 & 0 & 0 & 0 & 0 \\
0 & \dfrac{A_0^H}{2}e^{-i\theta} & -\dfrac{\omega}{2} & -k_x+ik_y & 0 & \dfrac{A_0^H}{2}e^{-i\theta} & 0 & 0 \\
\dfrac{A_0^H}{2}e^{i\theta} & 0 & -k_x-ik_y & -\dfrac{\omega}{2} & \dfrac{A_0^H}{2}e^{i\theta} & 0 & 0 & 0 \\
0 & 0 & 0 & \dfrac{A_0^H}{2}e^{-i\theta} & \dfrac{\omega}{2} & -k_x+ik_y & 0 & \dfrac{A_0^H}{2}e^{-i\theta} \\
0 & 0 & \dfrac{A_0^H}{2}e^{i\theta} & 0 & -k_x-ik_y & \dfrac{\omega}{2} & \dfrac{A_0^H}{2}e^{i\theta} & 0 \\
0 & 0 & 0 & 0 & 0 & \dfrac{A_0^H}{2}e^{-i\theta} & \dfrac{3\omega}{2} & -k_x+ik_y \\
0 & 0 & 0 & 0 & \dfrac{A_0^H}{2}e^{i\theta} & 0 & -k_x-ik_y & \dfrac{3\omega}{2}
\end{pmatrix}$$

$$(6.10)$$

Figure 6.1 Electron spectrum for graphene in time-periodic magnetic field

In units of $k_x = 2: -2$, $k_y = 0$, $\omega = 1$, $A_0^H = 1$, $\theta = \frac{\pi}{2}$ showing gapless structure

Although the application of an external magnetic field causes a deformation in the energy band structure, it can be found that gap opening is not achieved at the zero states as they are topologically protected. The change in band structure in the case of time dependent fields is related to the change in the periodicity of the Bloch amplitude, which evolves under the application of external fields. A minor change in the width of the band could accrue because of the speed of the

time dependence which causes a small change in the probability of inter-band transition.

6.3 Graphene superlattice in static magnetic field

6.3.1 SLG in linear laser and static magnetic field

In the second case we will consider a static magnetic field applied vertically on the graphene sheet. The laser will be applied with a chosen angle θ in respect to the static field. The graphene's electron state can be considered as:

$$\Psi = e^{-i\varepsilon t + ik_x x + ik_y y} \left[\psi_{A,B}^{++} \, e^{\frac{i\omega t}{2} + \frac{i\mu x}{2}} + \psi_{A,B}^{+-} \, e^{\frac{i\omega t}{2} - \frac{i\mu x}{2}} + \psi_{A,B}^{-+} \, e^{\frac{-i\omega t}{2} + \frac{i\mu x}{2}} \right.$$
$$\left. + \psi_{A,B}^{--} \, e^{\frac{-i\omega t}{2} - \frac{i\mu x}{2}} \right] \qquad (6.11)$$

Then we apply a static magnetic potential $\vec{A}^H$, in the y direction with A_0^H amplitude and μ_H frequency of the form:

$$\vec{A}^H(x)_x = 0 \,, \vec{A}^H(x)_y = A_0^H \cos(\mu x) \qquad (6.12)$$

With the linearly polarised laser:

$$\vec{A}(t)_x = A_0 \cos(\theta) \cos(\omega t) \ and \ \vec{A}(t)_y = A_0 \sin(\theta) \cos(\omega t) \qquad (6.13)$$

where $\omega = 1$, $A_0 = 1$, $A_0^H = 1$ & $\mu = 1$ with units of π/T at chosen phase shifts.
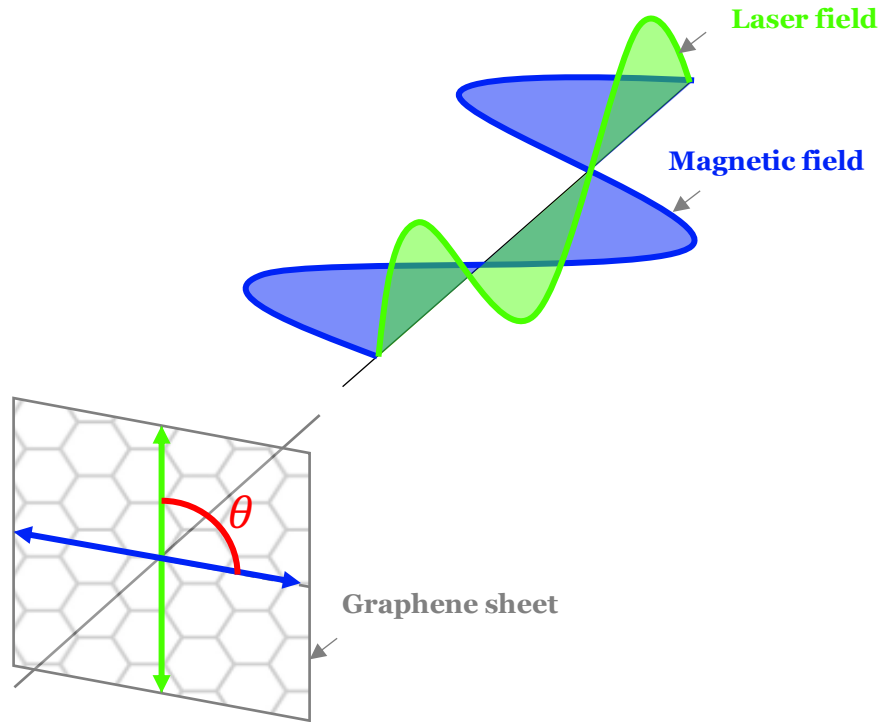
Figure 6.2 Schematic representation of the orientation set up for graphene in linearly polarized laser field applied in addition to an external spatially periodically modulated magnetic field which is applied perpendicular to the graphene sheet. The polarisation of the laser field is applied at a chosen incidence angle θ with respect to the orientation of the static field

Solving Dirac equation in the same proposed steps in model section equation (4.6), gives the an 8×8 matrix (equation 6.14), which determent can be found numerically to find the gapless energy spectrum $k_y = 0$ (Figure 6.3). The structure shows 3 Dirac points when the laser is perpendicular but then it shows a different structure if we change θ. Therefore, the spectrum needs to be investigated as the laser's parameters change.

$$
\begin{bmatrix}
\dfrac{\omega}{2} & k_x - ik_y + \dfrac{\mu}{2} & 0 & \dfrac{iA_0^H}{2} & 0 & -\left(\dfrac{A_0}{2}\right)e^{-i\theta} & 0 & 0 \\[2ex]
k_x + ik_y + \dfrac{\mu}{2} & \dfrac{\omega}{2} & \dfrac{-iA_0^H}{2} & 0 & -\left(\dfrac{A_0}{2}\right)e^{i\theta} & 0 & 0 & 0 \\[2ex]
0 & \dfrac{iA_0^H}{2} & \dfrac{\omega}{2} & k_x - ik_y - \dfrac{\mu}{2} & 0 & 0 & 0 & -\left(\dfrac{A_0}{2}\right)e^{-i\theta} \\[2ex]
\dfrac{-iA_0^H}{2} & 0 & k_x + ik_y - \dfrac{\mu}{2} & \dfrac{\omega}{2} & 0 & 0 & -\left(\dfrac{A_0}{2}\right)e^{i\theta} & 0 \\[2ex]
0 & -\left(\dfrac{A_0}{2}\right)e^{-i\theta} & 0 & 0 & \dfrac{-\omega}{2} & k_x - ik_y + \dfrac{\mu}{2} & 0 & \dfrac{iA_0^H}{2} \\[2ex]
-\left(\dfrac{A_0}{2}\right)e^{i\theta} & 0 & 0 & 0 & k_x + ik_y + \dfrac{\mu}{2} & \dfrac{-\omega}{2} & \dfrac{-iA_0^H}{2} & 0 \\[2ex]
0 & 0 & 0 & -\left(\dfrac{A_0}{2}\right)e^{-i\theta} & 0 & \dfrac{iA_0^H}{2} & \dfrac{-\omega}{2} & k_x - ik_y - \dfrac{\mu}{2} \\[2ex]
0 & 0 & -\left(\dfrac{A_0}{2}\right)e^{i\theta} & 0 & \dfrac{-iA_0^H}{2} & 0 & k_x + ik_y - \dfrac{\mu}{2} & \dfrac{-\omega}{2}
\end{bmatrix}
\tag{6.14}
$$

(a)

(b)
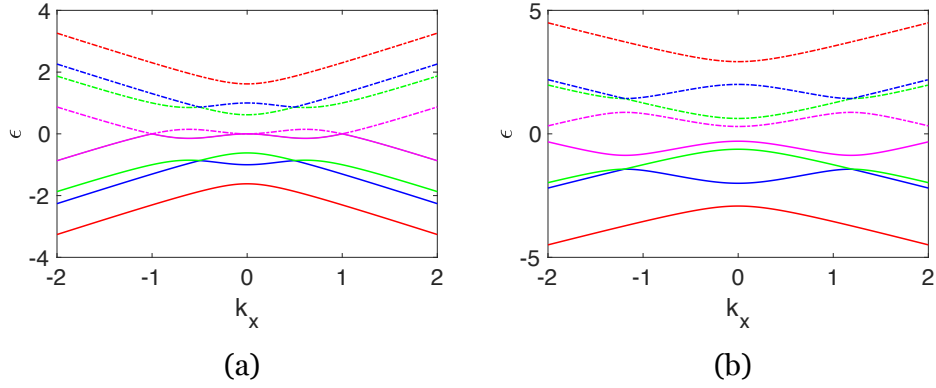
Figure 6.3 $\varepsilon(k_x, k_y)$ of SLG in the application of LPL field with a SPM field in the units of π/T, considering for a chosen orientation $\theta = 0$. (a) At, $\omega = 1$, $\mu_H = 1$, $A_0^H = 1$ and $k_y = 0$ the spectrum shows no gap across k_x axis (b) different low-band structure across k_x axis with no Dirac cones or points for $A_0^H = 1.1$, $A_0 = 1.3$, $\omega = 2.2$ & $\mu = 2.3$.

6.3.2 Graphene spectrum in laser rotation

To investigate the effect of the laser orientation we applied the laser in different angles holding the other parameters the same. Consequently, the orientation of Dirac points changed with similar angle to that of the laser's (Figure 6.4). It shows the contour plot of the low-energy spectrum $\varepsilon(k_x, k_y)$ taken in the vicinity of each K and K' points of the Brillouin zone for a single layered graphene in the perpendicular periodically modulated magnetic field and a linear polarised laser field tilted at different angles θ with respect to each other. The contour plot of the energy spectrum when $\theta = 0$ show the symmetry axes of the spectrum to be horizontally oriented parallel to k_x axis which coincides with the polarisation of the electromagnetic laser field. As we rotate the laser field polarisation on $\theta = \pi/4$ or $\pi/2$ angle, the Weyl Dirac points of the spectrum also rotates (see, panels b-e in Figure 6.4).
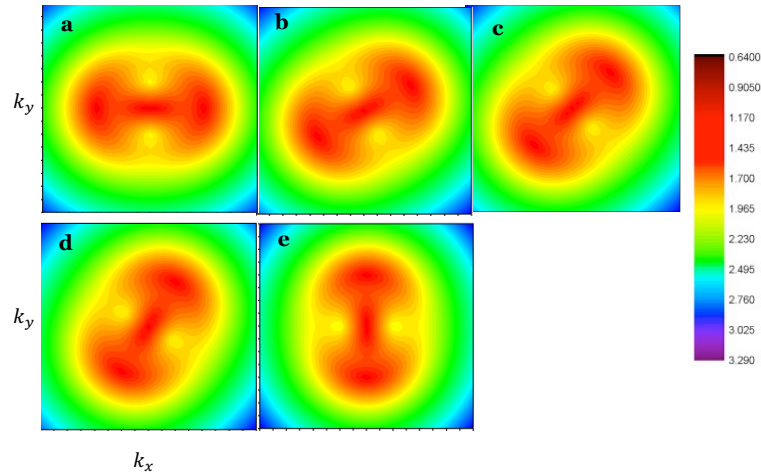
Figure 6.4 Electron spectrum $\varepsilon(k_x, k_y)$ in graphene in linearly polarized laser field with spatially periodic magnetic field with different orientations (a) $\theta = 0$ (b) $\theta = \pi/6$. (c) $\theta = \pi/4$. (d) $\theta = \pi/6$. (e) $\theta = \pi/2$. Showing the energy spectrum rotating with the magnetic field by the same angle without any change in the number of Dirac points. (considering $\omega = 1$, $\mu = 1$, $A_0 = 1$ and $A_0^H = 1$ in units of π/T).

(a)

(b)   (c)
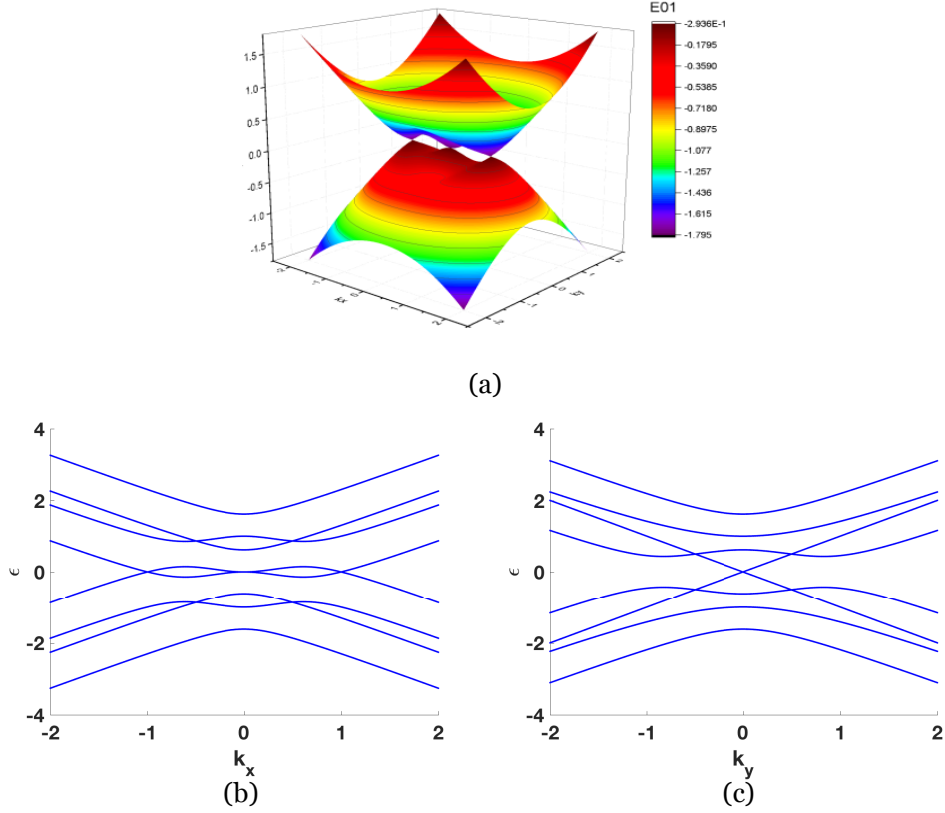
Figure 6.5 A three-dimensional plot and its cross sections of the energy spectrum $\varepsilon(k_x, k_y)$ of a SLG obtained in LPL field together with SPM field. The spectrum obtained with the parameters: $\omega = 1$, $\mu_H = 1$ and $A_0^H = 1$ for chosen fields orientations. (a) the spectrum shows two Dirac-Weyl points associated with Dirac cones and one highly anisotropic gapless point at $\varepsilon = 0$, corresponding both, $k_x = 0$ and $k_y = 0$. These two Dirac-Weyl points shifted in the k_x direction correspond to the creation of the monopole and the anti- monopole in the energy spectrum and are topologically protected. (b) we see this cross section while on the plot (c) we present the cross section of the spectrum taken at $k_x = 0$.

The static magnetic field is always applied perpendicular to the graphene sheet. Usually we should expect Landau Quantisation here and Landau spectrum consisting of Landau Levels if the spatial modulation period is very large. However, in additional linear polarised laser field and in the static field with the periodic spatial modulation the low energy spectrum from a first glance we see three Dirac points oriented parallel to k_x axes, when the wave vector $k_y = 0$ (see, the Figure 6.4). It is clear that this "tripling" is related to the spatial modulation

of the magnetic field in x- direction which is creating domain walls parallel to the y- axes. However, a more precise inspection of this part of energy spectrum in the vicinity of the zero energy reveals that we have here two Dirac-Weyl points and one highly anisotropic gapless Dirac-like point at $\varepsilon = 0$, corresponding to both, $k_x = 0$ and $k_y = 0$.

The two Dirac-Weyl points shifted in the k_x direction correspond to the creation of the monopole and the anti- monopole in the energy-momentum space having the form of Dirac cones in the vicinity of the zero energy. When these cones are separated in the momentum space they are topologically protected, and we cannot create a gap in the spectrum. But they can annihilate each other when you will be located at the same place and there an energy bandgap can be created. Note that the original Dirac point (in our notation here it is located at K or K' points of the Brillouin zone but at the values, $k_x = 0$ and $k_y = 0$) is now strongly deformed and lost its linear character along k_x direction.

The formation of the two Dirac-Weyl singularities in the vicinity of the K and K' points is a result of the dynamical topological phase transition created by an application of the both periodically modulated spatial and dynamical laser field. The position of these two Dirac-Weyl points can be rotated by the changes of the angle between the laser field polarisation and the direction of the applied field of the periodic spatial modulation, see the Figure 6.3, where for an illustration the calculations have been done with the values of the parameters: $\omega = 1, \mu_H = 1$ and $A_0^H = 1$. From this Figure 6.4 we see that when the polarisation direction changes by $\pi/2$ the position of these two Weyl-Dirac points is perpendicular to their original orientation, when the direction of the laser field polarisation and of the modulated field coincide (see, the Figure 6.5).

Therefore, Dirac points rotates by angle equals to the laser rotation angle θ, as we indicated before. The Figure 6.6 shows that the rotation of Dirac points does not fit a perfect circle (position wise) but it does in term of angles. The following plot represents Dirac points coordinates in k_x & k_y as the laser rotates a full circle (data in the table below). It can be argued that the energy solution is polarised in pseudospin by the direction of the magnetic field[41].

Table 6-1 The coordinates of the side Dirac points in Figure 6.5-a as a function of θ.

θ	k_x	k_y
0	1	0
30	0.8261	0.4783
45	0.6818	0.6818
60	0.5	0.8636
90	0	1
120	-0.5	0.8636
135	-0.6818	0.6818
150	-0.8261	0.4783
180	-1	0
210	-0.8261	-0.4783
225	-0.6818	-0.6818
240	-0.5	-0.8636
270	0	-1
300	0.5	-0.8636
315	0.6818	-0.6818
330	0.8261	-0.4783
360	1	0
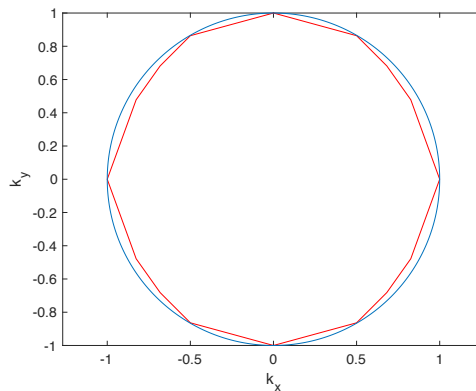
Figure 6.6 The rotation of Dirac points positions in Table 6-1 in laser rotation

6.3.3 Graphene spectrum at different laser frequencies

Similarly, the SPM field is theoretically applied vertically to the graphene sheet, and the LPL is applied with a chosen angle θ in respect to the static field. The spectrum near $\varepsilon = 0$, forms three zero energy points when the laser frequency is $\omega = 1$. Applying different frequency causes the spectrum to split in various ways causing changes in numbers of Dirac points and shapes of Dirac cones (see Figure 6.7). To determine these changes, the shapes, types and numbers of the cones have to be analysed as ω changes.
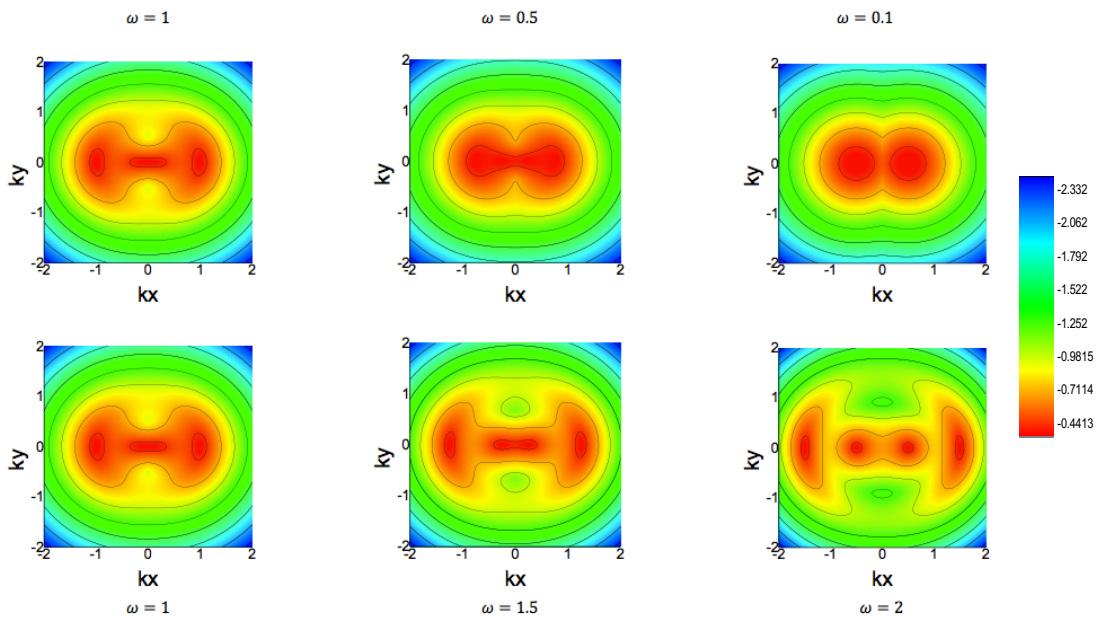
Figure 6.7 The energy spectrum of SLG in the application of SPM and LPL as laser frequency changes considering $\omega = 1$, $\mu = 1$, $A_0 = 1$ and $A_0^H = 1$ in units of π/T

The side cone in (Figure 6.7) has been found to form an elliptical shape at all ω sittings (Figure 6.8). To examine how the cone change/maintain shape as it expands we have measured the aspect ratio of a number of ellipses among the cone. The figure below shows a side ellipse expansion to be having the same anisotropy with a shared centre point (Figure 6.9).
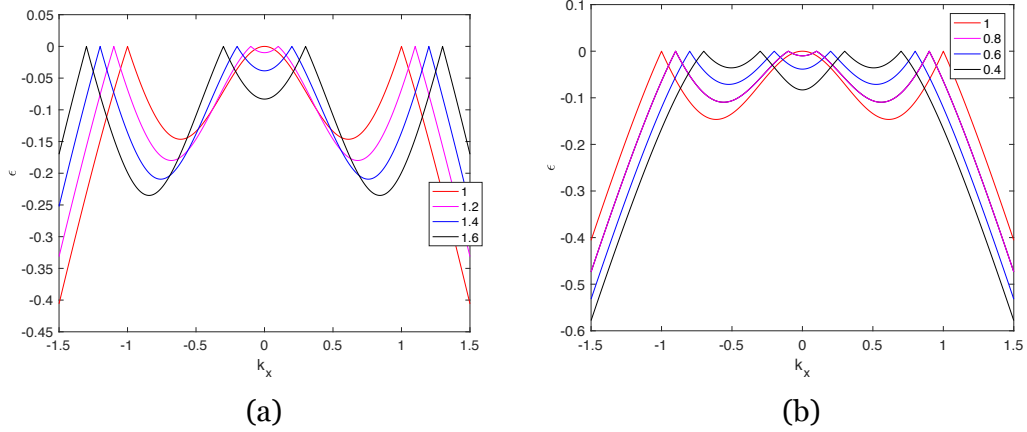
Figure 6.8 The linear cross section of the energy spectrum for low and high laser frequencies (a & b respectively)
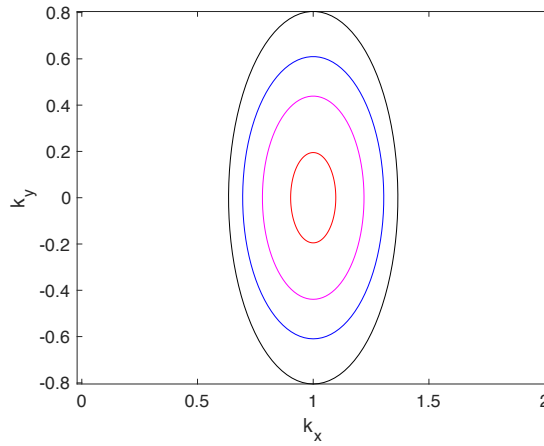
Figure 6.9 The cross area of the side elliptical cone having a fixed anisotropy of $\alpha = 2.1$ for 4 ellipses with a shared origin point (1,0) representing the spread of a cone

For instance, at $\omega = 1$, the side ellipse has a vertical orientation with an origin point $(k_x, k_y) = (1.0)$, which is the zero energy point at this case. Vertical ellipses have a Cartesian equation of: $\frac{x^2}{b} + \frac{y^2}{a} = 1$. In momentum space we will consider the vertical ellipse equation to be $\frac{k_x^2}{b} + \frac{k_y^2}{a} = 1$. The core ellipse has an equation of $\frac{k_x^2}{0.09} + \frac{k_y^2}{0.19} = 1$, with foci F_{i1} and F_{i2}. The foci length c is given by $c^2 = a^2 - b^2$, and the aspect ratio $\alpha = \frac{a}{b}$. The ellipse in this case has the anisotropy of $\alpha = \frac{0.19}{0.09} = 2.1$, which can be written as 2.1:1 as the aspect ratio of a circle is 1:1.

68

To determine wither this ellipse represents a cone, the ellipses have to maintain the same aspect ratio as we move away from zero energy. So, as the cone spreads, the anisotropy of the ellipses was found to be fixed to 2.1:1 (Table 6.2). This means that this is a cone. As the frequency increases the cones get sharper (Figure 6.10), hence the aspect ratio increases (Table 6.3).

Table 6-2 The major axis, minor axis, foci length and aspect ratio, for the side ellipse showing fixed α for different cones

ω	a	b	c	α
	0.1951	0.0976	0.169	2.1:1
1	0.439	0.2195	0.3802	2.1:1
	0.6098	0.3049	0.5281	2.1:1
	0.7317	0.3659	0.6337	2.1:1

Figure 6.10 The aspect ratio of the side Dirac cone as a function of laser frequency in LPL and SPM

Table 6-3 The aspect ratios α for the side cone at different laser's frequencies

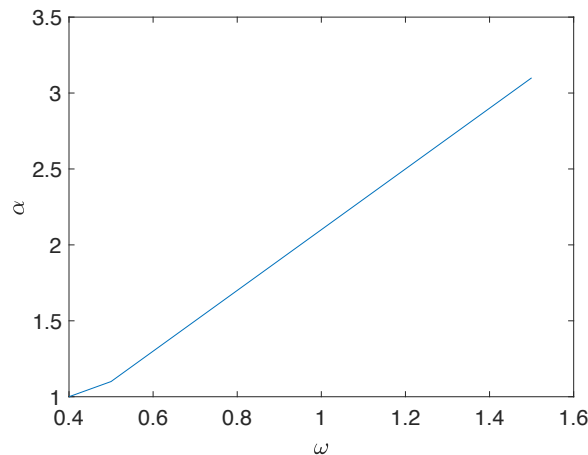| θ	0°							
ω	0.4	0.5	0.6	0.7	0.8	0.9	1	1.5
α	1	1.1	1.3	1.5	1.7	1.9	2.1	3.1

On the other hand, the middle cone in Figure 6.7 can be seen to exhibit some transformations as the laser frequency changes. Starting at $\omega = 1$, the middle cone can be seemed to be forming a quadratic curve than can be described as a Cassini oval. This single loop has two fixed foci points $(\pm A, 0)$, and the product of the distance from any point on the spectrum to the foci's is fixed by the value B^2. The curve has an equation of the form: $\big((k_x - A)^2 + k_y^2\big)\big((k_x + A)^2 + k_y^2\big) = B^2$. By $\varepsilon(k_x, k_y) = 0$.

The type of these cones have been identified by taking linear cross sections across the spectrum at different laser frequencies. For $\omega = 1$, the side cone forms a Dirac cone, with a single Dirac point. The middle cone however is parabolic as the conduction and the valence bands touch in a line as we zoom in across k_x axis (refer to Figure 6.11). The cut along the k_y axis in Figure 6.9 confirms that the band is parabolic at $(k_x, k_y) = (0,0)$ and $\omega = 1$. Near the zero-energy point $\varepsilon = 0$ at $k_x = k_y = 0$, the spectrum no longer forms a cone since it shows parabolic dependence on momentum for the energy cross-section at $k_y = 0$ and linear like dependence for the energy cross section at $k_x = 0$. This can be interpreted as divergence of anisotropy α when k_x tends to zero.

The splitting and change of shape in the spectrum in different frequencies can be associated with Cassini ovals as the following. For small frequencies $\omega < 0.5$, the spectrum forms two Cassini ovals, with fixed foci points P and P' at $(\pm 0.5, 0)$. However, B is different for each ω. At $\omega = 0.1$, $B = 0.45$ which is smaller than A indicating that the shape of the ovals is going to consist of two loops (Figure 6.12). Then as ω is increased B will increase to become $B = 0.48 \approx A$ at $\omega = 0.3$ forming the shape of lemniscate of Bernoulli. When $\omega = 0.5$, then $B = 0.8$ which is larger than A, so the spectrum will be one loop of Cassini oval. For higher ω, the spectrum is split to three ovals, where the middle oval is Cassini oval, with varying foci points and shape as ω changes.
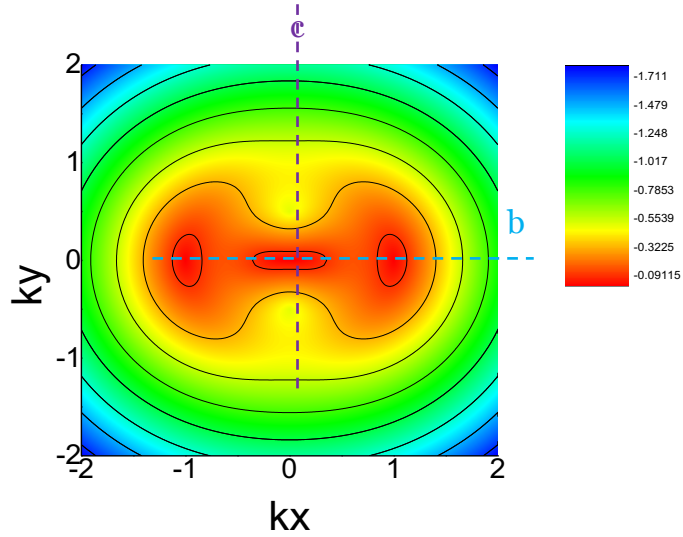
(a)
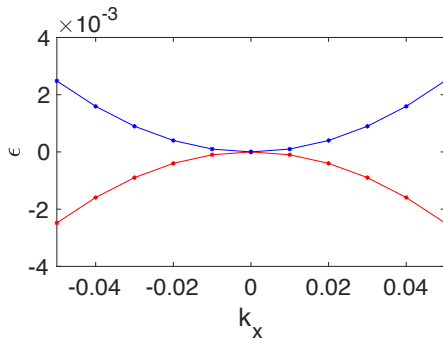
(b)
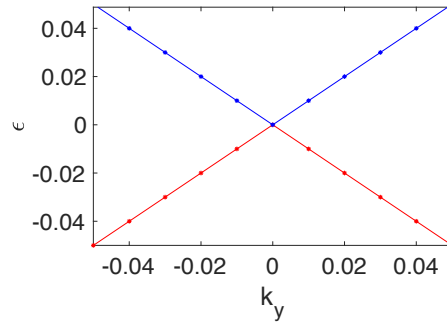
(c)

Figure 6.11 The cut line of the middle oval in the energy spectrum for graphene in linear laser and static magnetic field. (a) shows the middle cone in the energy spectrum (b) a zoomed plot of the middle cone showing the upper and the lower bands to be parabolic (c) the cut of the oval along the k_y axis at $k_x = 0$, confirming that the connection between the bands is a line. Thus in (a) the spectrum has a parabolic-type dependence in $\varepsilon \propto k_x^2$ and in (b) shows linear-type dependence $\varepsilon \propto |k_y|$. This indicates infinite anisotropy at $k_x = k_y = 0$.

$\omega = 0.1$	
$\omega = 0.3$	
$\omega = 0.5$	
$\omega = 0.7$	
$\omega = 0.9$	
$\omega = 1$	
$\omega = 1.1$	
$\omega = 1.3$	
$\omega = 1.5$	
$\omega = 1.7$	
$\omega = 1.9$	
$\omega = 2$	
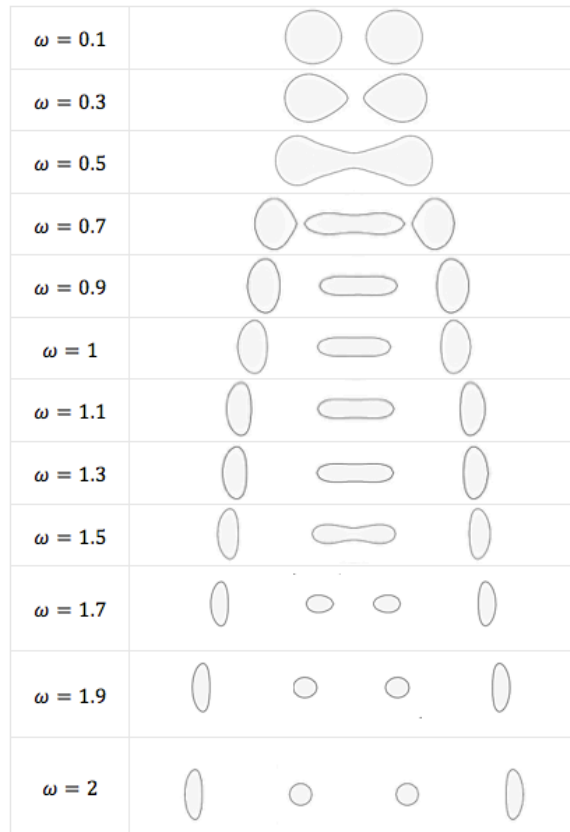
Figure 6.12 Cassini ovals in the energy spectrum of SLG in the application of SPM and LPL with different laser frequencies ω

As Cassini ovals change in numbers, shapes and positions, the foci points of the Cassini ovals also change with the frequency as in Figure 6.12. For $\omega \leq 0.5$, the foci points are the middle points between Dirac points, and for $\omega > 0.5$, Dirac points represents the foci points of Cassini ovals. So, the transition point is at the frequency where the two loops split into three loops at $\omega > 0.5$. For all $\omega \neq 1$, the spectrum has 4 Dirac points and 4 Dirac cones. At $\omega = 1$, the spectrum has three Dirac cones with three Dirac points.
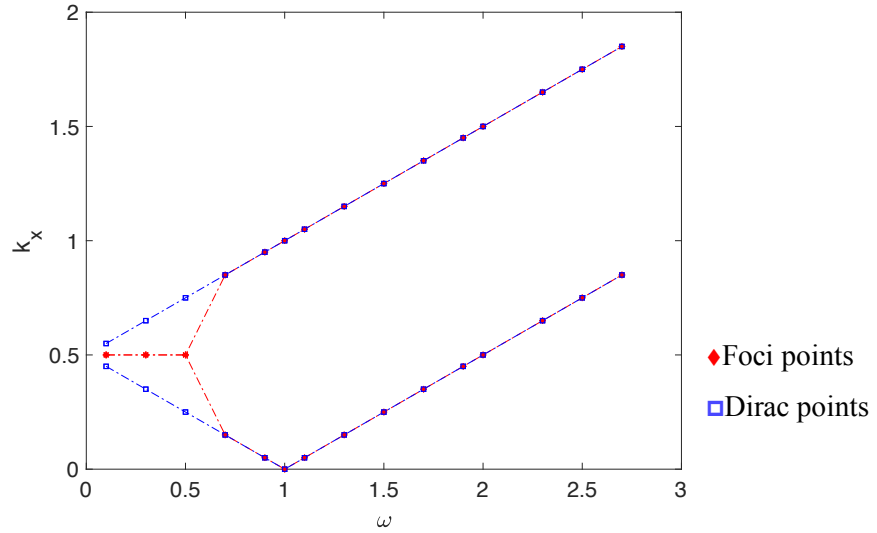
Figure 6.13 The positions of Cassini ovals foci points and Dirac points for different frequencies.

6.3.4 Graphene spectrum in different laser amplitude

The energy spectrum of SLG has been investigated in SPM and LPL with a range of laser amplitudes. Applying a laser with a small amplitude causes a gap opening in the centre of the spectrum (Figure 6.14-a). As the amplitude increases the gap becomes narrower until it reaches zero point at $A_0 = 1$. Before this point the spectrum has two Dirac cones/points, and at $A_0 = 1$ Dirac points become three, then for $A_0 > 1$ we see four Dirac points. Dirac points move apart from the centre as the amplitude increases (Figure 6.14-b). The spectrum has been found to form a parabolic cone at $A_0 = 1$, which then become a typical Dirac cone for $A_0 > 1$ (Appendix 1).
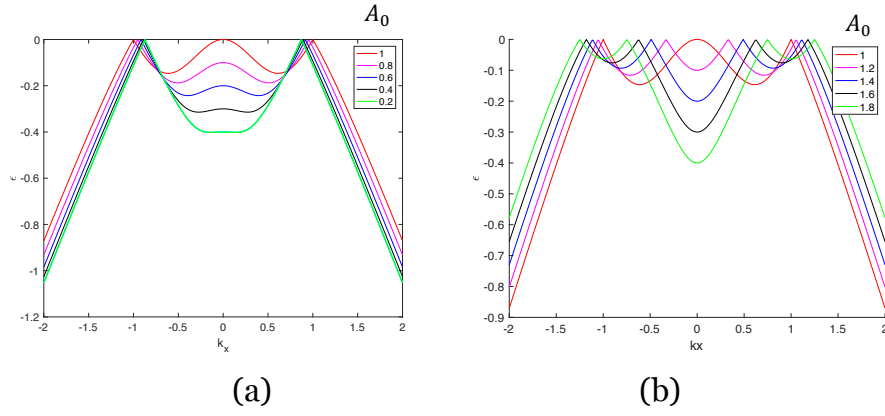
Figure 6.14 The energy spectrum $\varepsilon(k_x, k_y)$ of SLG in the application of SPM field and a LPL with different amplitudes showing (a) a gap reduction as the laser amplitudes increases (b) a split in the middle oval producing two cones each with a single Dirac point

The counter plot of the spectrum (Figure 6.15) shows the in-change shape and position of Dirac cones as A_0 varies. The side cone can be seen to form an elliptical cone, with an anisotropy that changes with different laser amplitudes. As Figure (6.16) illustrates, the aspect ratio of the side cone decreases as the amplitude increases (Table 6.4).
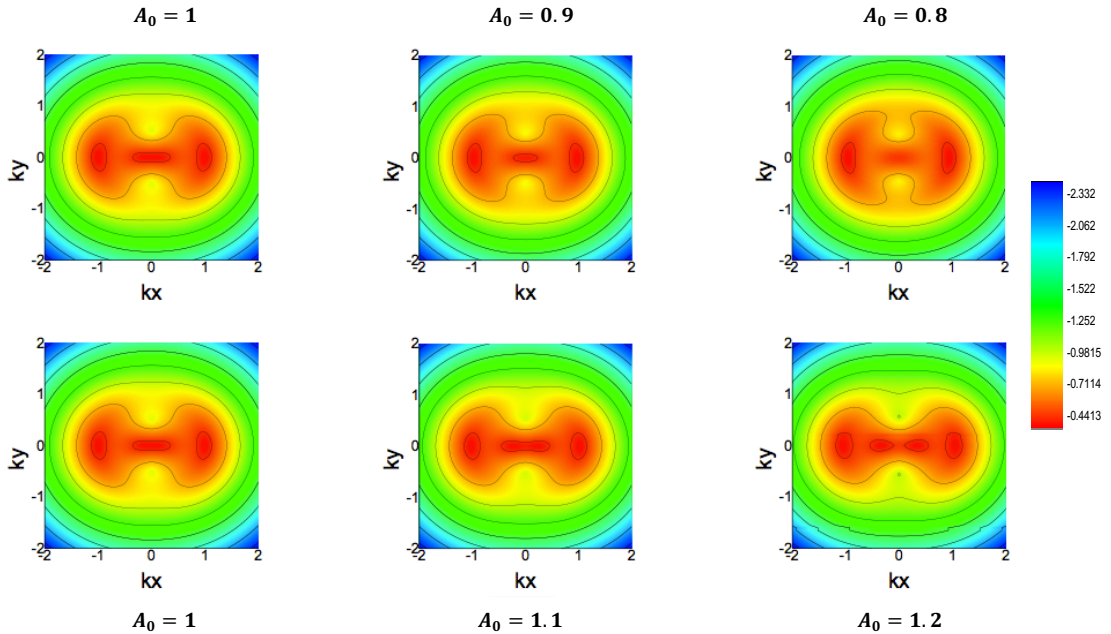
Figure 6.15 Counter plot of $\varepsilon(k_x, k_y)$ for monolayer graphene in the application of SPM field and a LPL with different amplitudes A_0 considering $\omega = 1$, $\mu = 1$, and $A_0^H = 1$ in units of π/T
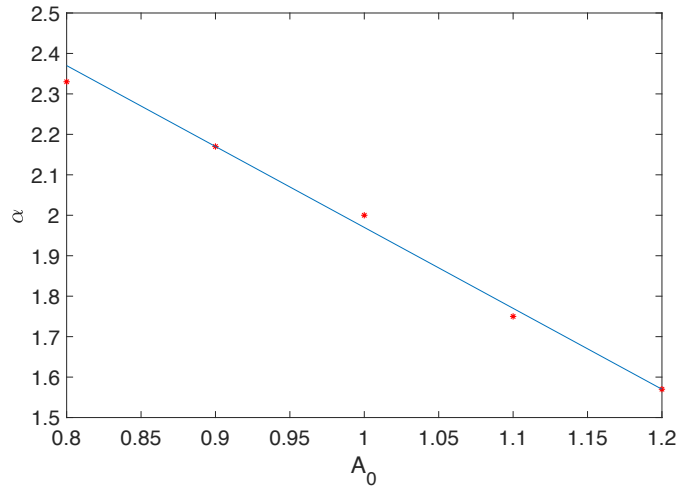
Figure 6.16 The aspect ratio of the side cone for a number of laser's amplitudes A_0

Table 6-4 The axis of the side cone ellipse in Figure 6.15 as the laser amplitude changes

Amplitude A_0	Major axis a	Minor axis b	Focal length c	Aspect ratio α
0.8	0.58	0.25	0.27	2.33
0.9	0.54	0.25	0.23	2.17
1	0.5	0.25	0.19	2
1.1	0.5	0.29	0.17	1.75
1.2	0.46	0.29	0.13	1.57

The change in the middle cone can be described by the size of the gap opening, then by the splitting of the cone. From Figure (6.14), it can be seen that for small laser amplitudes there is a gap opening that can be controlled by changing the A_0. The plot represents the size of the gap as a function of the laser's amplitude.
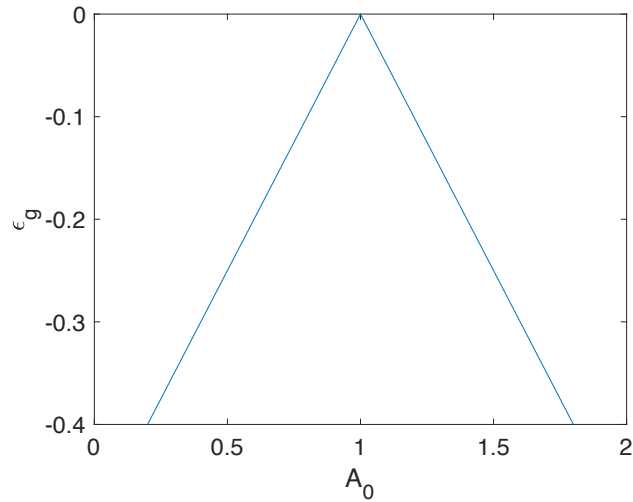
Figure 6.17 The size of the gap in the energy spectrum a function of
the laser's amplitude

The spectrum forms different shape of loops that can be assigned to Cassini ovals (refer to Figure 6.18). As the ovals change in shape, the positions of Dirac points change according to Figure 6.19, where the number of Dirac points increased for amplitudes larger than $A_0 = 1$.
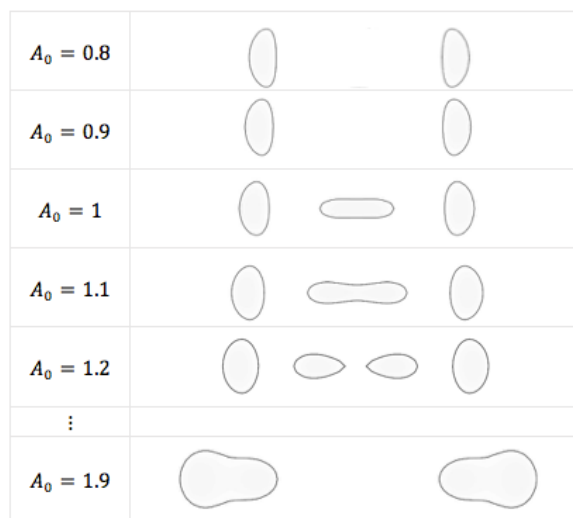
Figure 6.18 Cassini ovals in the energy spectrum of graphene in the
application of SPM field and LPL with a range of amplitudes A_0
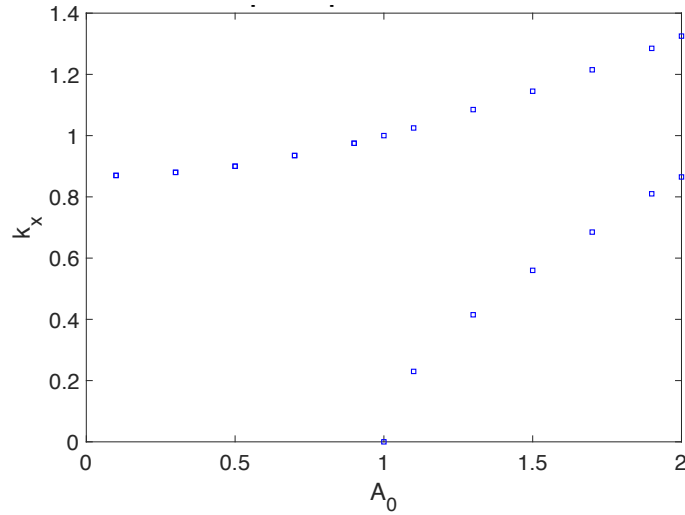
Figure 6.19 The positions of Dirac points in the spectrum of SLG in the duality of LPL and SPM field as the laser's amplitude changes

6.4 Dirac cones manipulation

The energy spectrum in SLG can be highly controlled if more than one laser parameter changes at the same application. Since the spectrum has been found to maintain its symmetry in laser rotation, this allows the choosing of the orientation of the Dirac points in an angle equal to the laser angle θ. The following Figure 6.20 of the spectrum displays the orientation of $\theta = \pi/4$ for different laser frequencies. The spectrum shows the exact structure and numbering at each ω as in θ. To confirm the symmetrical rotation of $\varepsilon(k_x, k_y)$, we measured the aspect ratio of the side cone different angles and found α to be 2.1:1 (Table 6.5 & Figure 6.21).
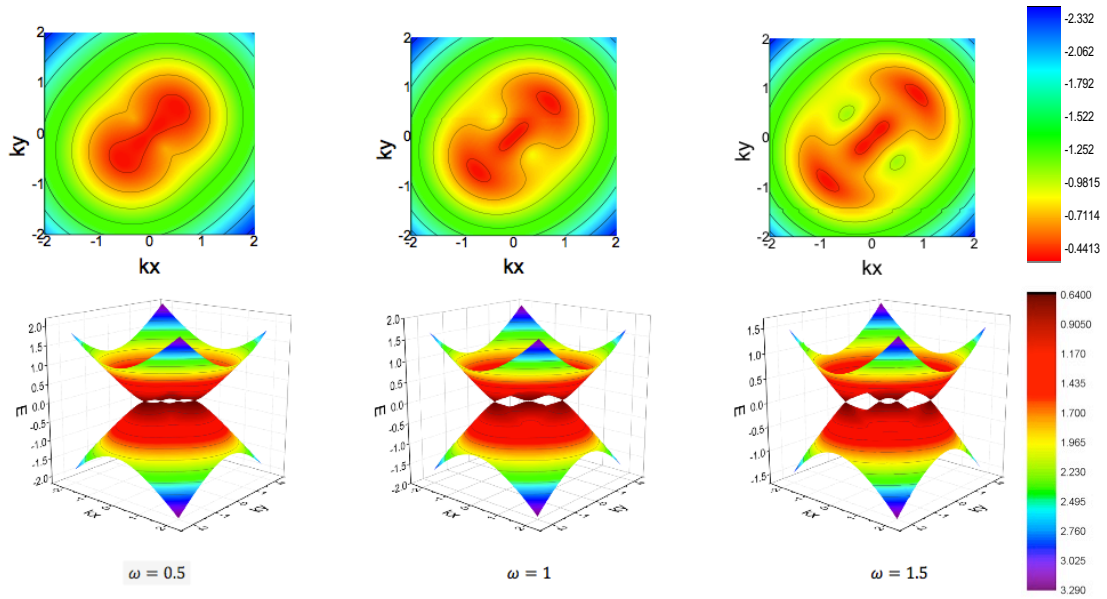
Figure 6.20 Counter and 3D plots for the spectrum in a chosen orientation with different frequencies in units of π/T considering $\mu = 1$, $A_0 = 1$ and $A_0^H = 1$ in units of

Table 6-5 The aspect ratio of the side cone as the energy spectrum rotates by the angle θ

θ	α
0	2.1
$\dfrac{\pi}{6}$	2.1
$\dfrac{\pi}{4}$	2.1
$\dfrac{\pi}{3}$	2.1
$\dfrac{\pi}{2}$	2.1
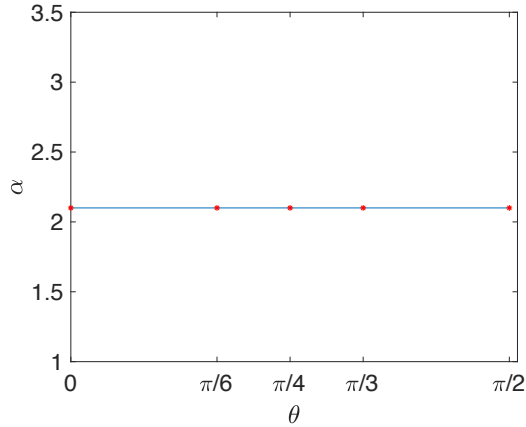
Figure 6.21 The aspect ratio α as a function of laser angle θ

In the following application we chose a desired energy structure for SLG. The desired orientation of 2 vertical Dirac points with a middle gap of the size is 0.4 (units of π/T). Therefore, the laser settings are: $\theta = \pi/2$, $A_0 = 0.2$ and $\omega = 1$. The resulted spectrum will be of the form as in Figure (6.22).

(a)   (b)
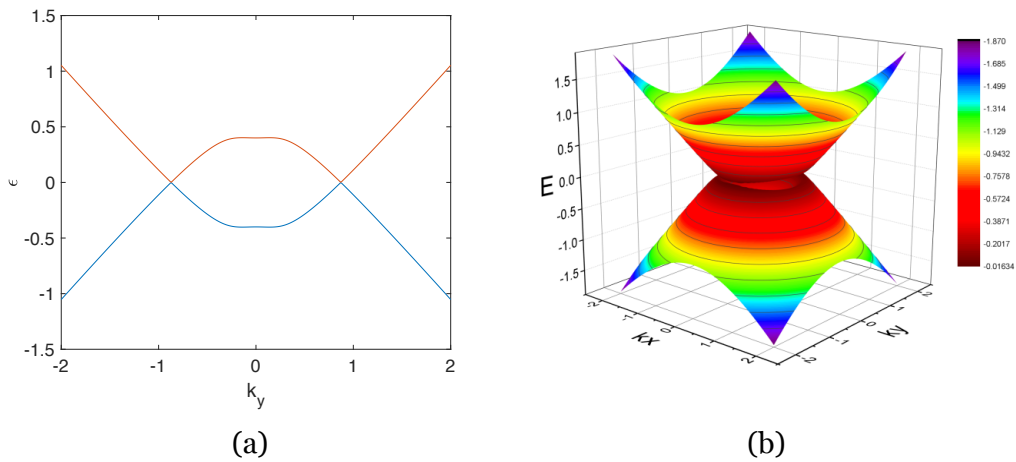
Figure 6.22 The energy spectrum of SLG controlled by LPL and SPM Showing (a) 2D display of 2 Dirac points parallel to the k_y axis with a mini gap in the middle (b) the 3D display of the spectrum

6.5 Space shift symmetry breaking

To be able to understand the motion of electrons' in the proposed systems, the symmetry breaking needs to be understood. The system of SLG in SPM and

LPL can be shown to be symmetric under time inversion, space inversion, and both. This was approached by solving Schrodinger equation and reproducing the energy bands (Figure 6.23). With space shift the symmetry of the system is broken, we chose a shift of half period. Time shifting though does not break the symmetry (Figure 6.24).

(a)

(b)

(c)

(d)
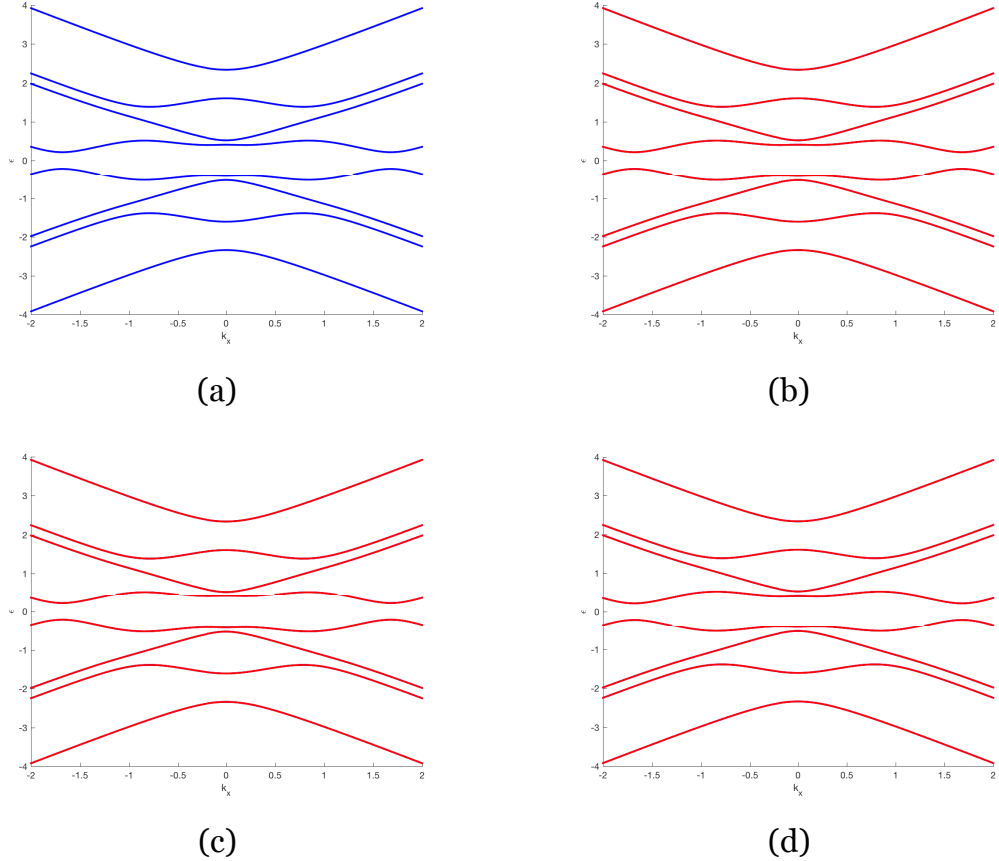
Figure 6.23 The energy spectra of graphene in linear laser and static magnetic field

(a) considering $\omega = 1$, $\mu_H = 1$ and $A_0^H = 1$ for a chosen orientation of the laser $\alpha = 0$ given in the units of π/T, (b) The spectra under time inversion $t \to -t$. (c) Space inversion $x \to -x$. (d) Time and space inversion. The spectra of the system is symmetric under these inversions.

The reason for the breaking the inversion symmetry is that the two sublattices are no longer equivalent. This is due to the interactions between the massless particles in graphene with the high external field. Applying a magnetic field alone or a LPL field alone does not break the inversion symmetry. The effect of electron-phonon couplings can be neglected. However, if the two fields are combined, then their effect break the chiral symmetry. As a consequence, a dynamical band gap

will be induced in the energy spectrum of graphene due to the nonlinear dependence of the magnetic field [96].
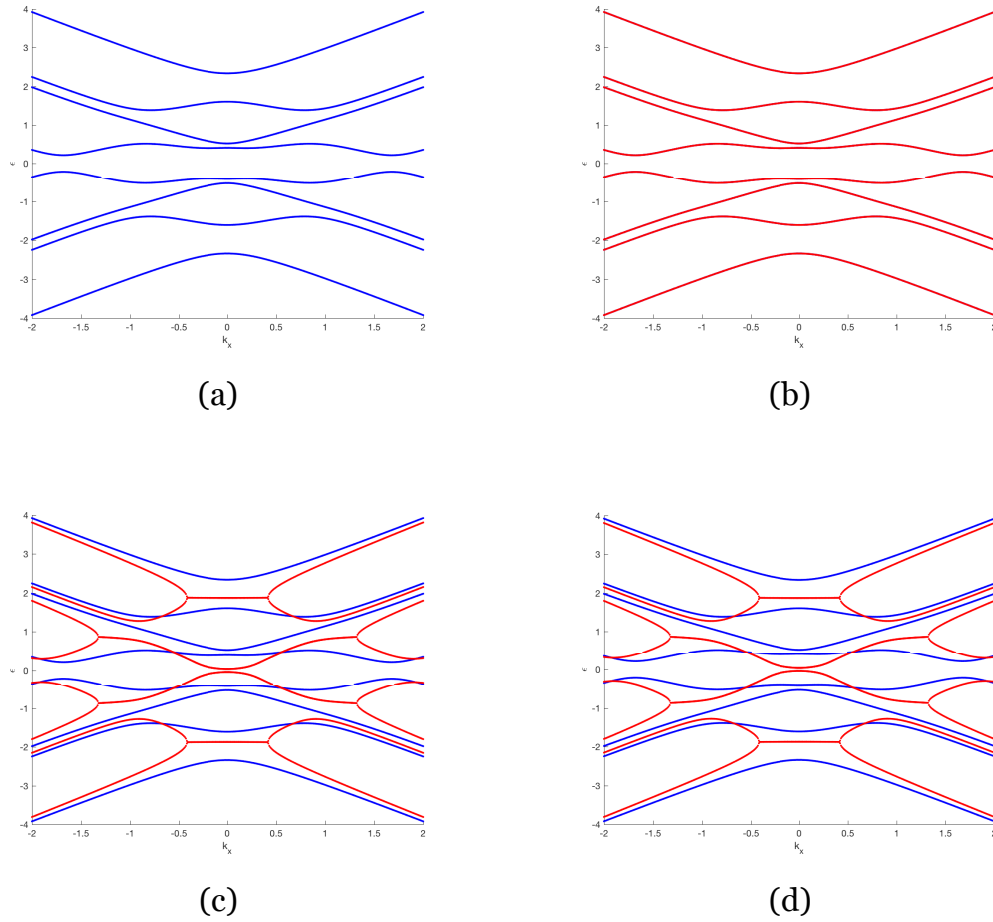
Figure 6.24 The energy spectra of graphene in linear laser and static magnetic field

 in the units of π/T, (a) The spectrum of the energy considering $\omega = 1$, $\mu_H = 1$ and $A_0^H = 1$ for a chosen orientation of the laser at $\theta = 0$, given by the blue spectrum for comparison (b) The spectra under time shift $t \to t + \frac{\pi}{2}$, being symmetric. (c) Space shift $x \to x + \frac{\pi}{2}$, showing a break in symmetry. (d) Time and space shift introduces symmetry breaking

6.6 Summary

We investigated the change in the energy spectrum of SLG in the application of two potential of LPL and SPE fields. This duality aims to control and manipulate Dirac points by changing the lasers' parameters.

The spectrum of graphene in this model is found topologically symmetrical as the laser is rotating, where the spectrum rotates with the same laser angle θ with no other changes. The spectrum was found to be time and space symmetric. However, space shift breaks the spectrum symmetry causing the gap opening in the energy band. The spectrum was further investigated with different laser frequencies ω. It has been found the spectrum changes the shapes and the number of cones as the frequency changes. The chiral symmetry is though broken, causing a gap band induction in the energy spectrum. This implies that the laser in this proposed model can be applied in any angle desired and the frequency and the amplitude can be used to control the splitting and the gap creation.

Overall, we shown that static periodically modulated magnetic/electric field together with linearly polarised laser field induce dynamical topological phase transitions in a single graphene layer. There in the vicinity of the original K and K' Dirac points the pairs of Weyl-Dirac cones are created. Then the graphene layer may be viewed as two-dimensional Weyl metal. The created Weyl metal energy spectrum is invariant under the laser field rotation when there is only spatial modulation of magnetic field. However, when the static electric field is periodically modulated, the system shows additional symmetry breaking phenomenon where additional pairs of the Weyl-Dirac cones are created. We show that this effect is controlled by a laser field tilting from the graphene plane where the modulated electric field is embedded. We expect that the described effect may be used in novel optoelectronic devices and the predicted phenomena will be observed in the future experiments.

The change in the energy band shape and Dirac points position is caused by the broken symmetry due to effect of the two applied fields: LPL and SPM. The coupling introduced a nonlinear effect, determined here by a parabolic cone, which causes the gap opening in the spectrum. Consequently, the duality of the fields allows Dirac points manipulations by changing only the laser's parameters.

The spectrum behaves as Cassini ovals in laser's alteration, where these ovals change shape and position in general, but change in number around the parabolic point. This form of change in anisotropy introduced anisotropic transport that can be controlled by the laser.

7 Graphene Superlattices in Static Electric Field

7.1 Graphene in linearly polarised laser and static electric field

For a graphene crystal with electron wave function given by (6.11), in the application of LPL with A_0 amplitude and frequency $\omega = \frac{2\pi}{T}$, given by (6.13), we theoretically apply a spatial periodic electric (SPE) field of the form:

$$U(x) = U_0 \cos(\mu x) \qquad\qquad (7.1)$$

where U_0 is the magnetic amplitude and μ is the magnetic frequency. The electric field will be in plane with the graphene sheet (Figure 7.1) considering $\omega = 1$, $A_0 = 1$, $U_0 = 1$ & $\mu = 1$.
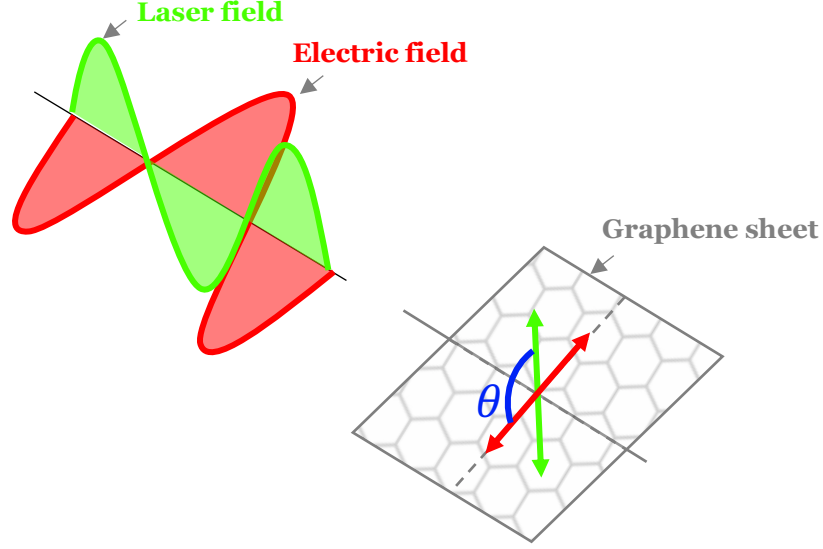
Figure 7.1 Schematic representation of the orientation set up for graphene in linearly polarized laser field applied in addition to an external spatially periodically modulated electric field SPE which is located in the graphene plane while a linear polarised laser field is tilted by angle θ with respect to the orientation of the electrical field

Substituting the wave function and the potentials into the 2D Dirac equation (3.22), we will obtain a differential equation with 8×8 matrix M given by (7.2). The energy spectrum is given by the determinant of M matrix in Figure 7.2. An energy band gap is obtained within the miniband structure. The number of Dirac points changes as the laser phase changes (See Figure 7.2 a, b, c & d for details).

$$
\begin{pmatrix}
\frac{\omega}{2} & k_x - ik_y + \frac{\mu}{2} & \frac{U_0}{2} & 0 & 0 & -\frac{A_0}{2}e^{-i\theta} & 0 & 0 \\
k_x + ik_y + \frac{\mu}{2} & \frac{\omega}{2} & 0 & \frac{U_0}{2} & -\frac{A_0}{2}e^{i\theta} & 0 & 0 & 0 \\
\frac{U_0}{2} & 0 & \frac{\omega}{2} & k_x - ik_y - \frac{\mu}{2} & 0 & 0 & 0 & -\frac{A_0}{2}e^{-i\theta} \\
0 & \frac{U_0}{2} & k_x + ik_y - \frac{\mu}{2} & \frac{\omega}{2} & 0 & 0 & -\frac{A_0}{2}e^{-i\theta} & 0 \\
0 & -\frac{A_0}{2}e^{-i\theta} & 0 & 0 & -\frac{\omega}{2} & k_x - ik_y + \frac{\mu}{2} & \frac{U_0}{2} & 0 \\
-\frac{A_0}{2}e^{-i\theta} & 0 & 0 & 0 & k_x + ik_y + \frac{\mu}{2} & -\frac{\omega}{2} & 0 & \frac{U_0}{2} \\
0 & 0 & 0 & -\frac{A_0}{2}e^{-i\theta} & \frac{U_0}{2} & 0 & -\frac{\omega}{2} & k_x - ik_y - \frac{\mu}{2} \\
0 & 0 & -\frac{A_0}{2}e^{-i\theta} & 0 & 0 & \frac{U_0}{2} & k_x + ik_y - \frac{\mu}{2} & -\frac{\omega}{2}
\end{pmatrix}
$$

(7.2)
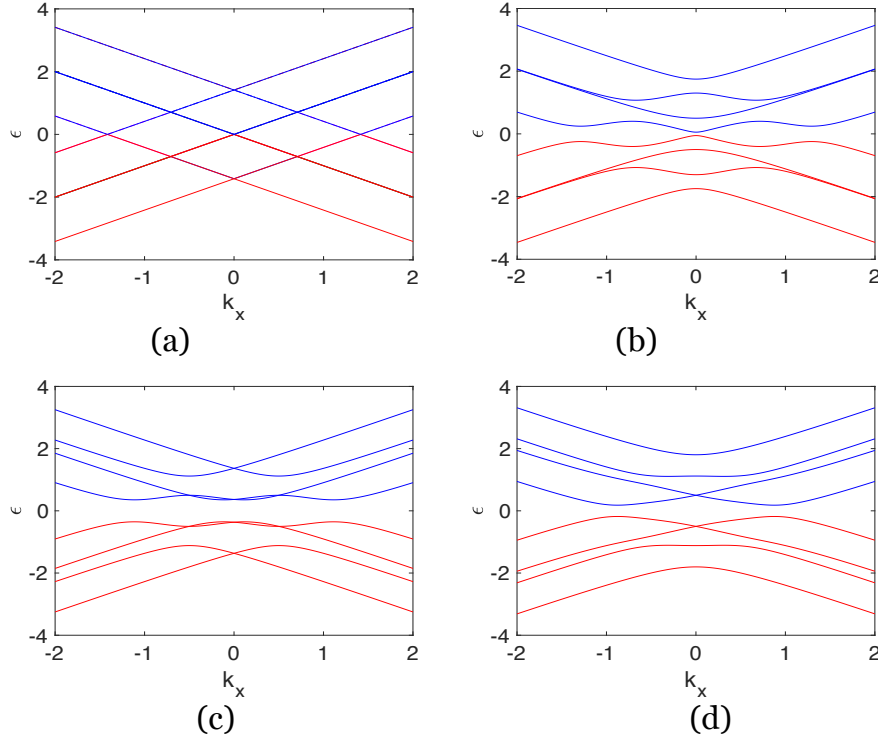
Figure 7.2 Electron spectra for graphene in LPL field in the existence of SPE field with units of π/T (a) Considering $\omega = 1$, $\mu = 1$, $U_0 = 1$ and $A_0 = 1$ for a chosen orientation $\theta = 0$. The spectrum shows the hole states in the upper bands and electron states in the lower bands with $k_y = 0$. A gap can be seen within the band structure. (b) viewing the band structure in the y direction shift ($k_y = 0.5$) (c) The energy spectrum for graphene in linearly polarised laser field for the chosen orientation $\theta = \pi/2$ showing a change in the number of Dirac points (reduction) in contrast to the case where $\theta = 0$ (d) showing the spectrum at $k_y = 0.5$.

If we apply a static periodically modulated electric field and the linearly polarized laser field in the plane of the graphene sheet there are arise two pairs of the Weyl-Dirac points. In this case when $\theta = 0$ the energy spectrum shows that Dirac cones of graphene split into several mini bands (see, Figure 7.3-a). The case is very similar to the model presented in chapter 6, the spectrum has two Dirac-Weyl point and one central original Dirac point. However, the elongation of this central point is different, it occurs along k_y axes. All these points are located along the k_x axis and the spectrum seems to be gapless. The 3D plot (see, the Figure 7.3-b) shows the shape of these Dirac and Weyl cones and that the middle Dirac cone is elliptically shaped. When the angle θ changed from 0 to $\frac{\pi}{2}$ the number and positions of Dirac-Weyl points changed to four (see, Figure 7.3-c), indicating a

dynamical symmetry breaking phenomenon arising in the band structure with changes of the different laser beam orientations.

(a)

(b)   (c)
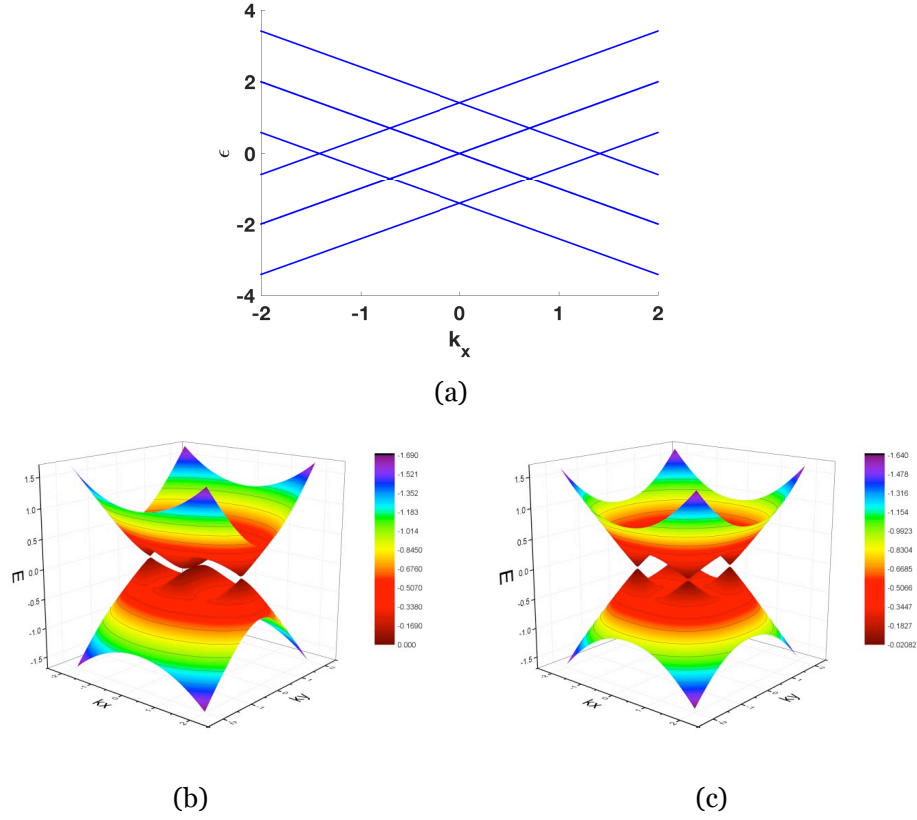
Figure 7.3 Electron spectra $\varepsilon(k_x, k_y)$ for graphene subjected to linearly polarised laser fields with a static spatially-modulated periodic electric field. In the calculations we used the parameters $\omega = 1$, $\mu = 1$, $U_0 = 1$ and $A_0 = 1$ for each of chosen orientations, θ. (a) The spectrum shows gapless multiple crossing at the plane crossing the k_x axes. (b) showing two Weyl-Dirac located symmetrically with respect to the central Dirac point at K or K' place in the Brillouin zone. All these three gapless points are along k_x axis at the value, $k_y = 0$. (c) The spectrum rotated by an angle equal to the laser's beam orientation, i.e., $\pi/2$, forming two pairs of Weyl-Dirac cones symmetrically positioned around K or K' points of the Brillouin Zone.

7.2 The duality of static electric field and a rotating laser

The change of the laser orientation with respect to the electric field will cause Dirac point to rotate and reposition (Figure 7.4).
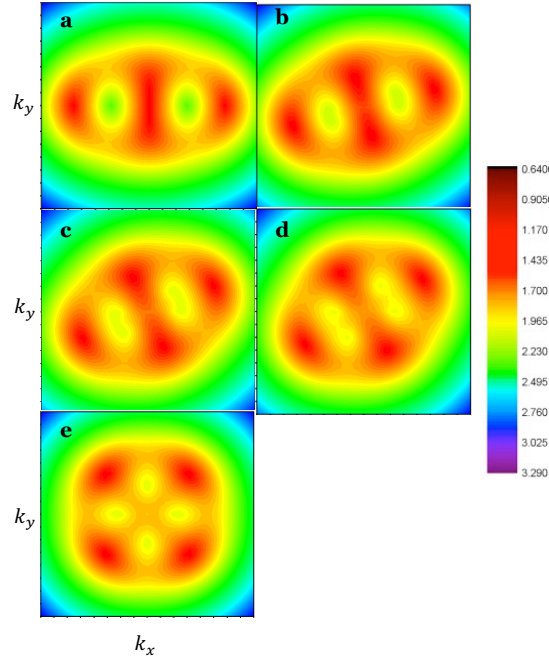
Figure 7.4 Electron spectrum $\varepsilon(k_x, k_y)$ in graphene in LPL field with SPE field in different orientations. (a) $\theta = 0$ (b) $\theta = \pi/6$, (c) $\theta = \pi/4$ & (d) $\theta = \pi/3$ showing the energy spectra rotating and repositioning of Dirac points as their number is increasing as the electric field reaches an angle of $\pi/2$ with respect to the laser field (e) $\theta = \pi/2$. ($\omega = 1$, $U_0 = 1$ and $A_0 = 1$ in units of π/T).

To investigate the change in the spectrum in details, surface contour plots were shown at different laser field angles. For $\theta = 0$ there are three gapless points where the top and bottom energy bands touch each other. The two side cones in Figure 7.5-a can be approximated as squeezed Dirac cones, $\varepsilon^2 = a\,(k_x)^2 + b(k_y)^2$,

while near the middle point, the structure shows a curve of energy $\varepsilon^2 = a(k_x)^2 + b(k_y)^4$, where a and b some real parameters. As the laser is rotating Figure 7.5-b, where the laser is applied at $\theta = \pi/4$, two changes occur: 1- the spectrum is rotating in a similar manner and 2- the middle point experience a splitting where the energy cut transforms into two squeezed cones. The result is a spectrum which has 4 Dirac points. When the laser field orientation changes further, to become perpendicular with $\theta = \pi/2$, the spectrum is rotated by $\pi/2$ forming 4 Dirac-Weyl cones symmetric about the pole (see, the Figure 7.5-c), which is associated with K or K' of the graphene Brillouin zone.
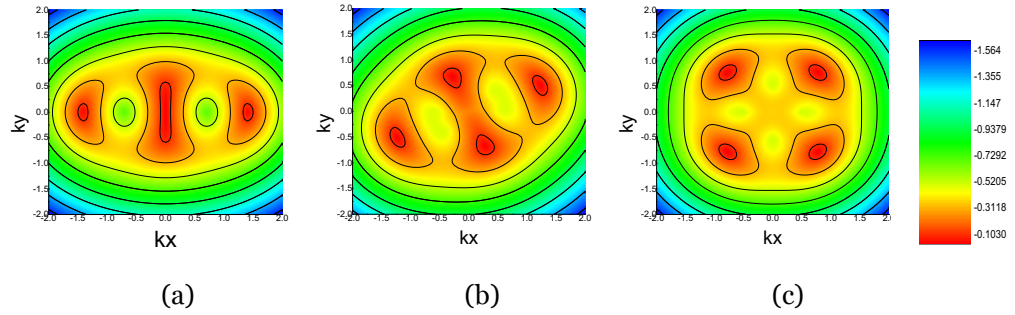
Figure 7.5 The surface contour plot of the spectrum dispersion, $\varepsilon(k_x, k_y)$, for a monolayer graphene subjected to in-plane static periodically modulated electric field and a linear polarised laser field tilted at the angle θ to the graphene plane
 (a) the case when the polarisation of the electromagnetic laser field coincides with the direction of the modulated electrical field, i.e. $\theta = 0$; Here we see a pair of the Weyl points located far apart from each other. In a centre there is an elongated valley where a new pair of Weyl points is going to be nucleated, when the tilting angle increases, i.e. when $\theta \neq 0$; (b) The snapshot of the spectrum taken when the tilting angle $\theta = \pi/4$; We see already two pairs of the Weyl points here (c) The snapshot spectrum displaying two symmetrical pairs of the Weyl points taken at their perpendicular orientation, i.e. at $\theta = \pi/2$.

Table 7-1 The change in Dirac cone's aspect ratio with different Laser incident angle

θ	α side cone	α middle cone
0	1.667	6
$\pi/6$	1.933	1.974
$\pi/4$	1.829	1.2
$\pi/3$	1.667	1
$\pi/2$	1.447	1.447
$2\pi/3$	1.667	1
$3\pi/4$	1.829	1.2
$5\pi/6$	1.933	1.974
π	1.667	6
$7\pi/6$	1.933	1.974
$5\pi/4$	1.829	1.2
$4\pi/3$	1.667	1
$3\pi/2$	1.447	1.447
$5\pi/3$	1.667	1
$7\pi/4$	1.829	1.2
$11\pi/6$	1.933	1.974
2π	1.667	6

For a single layer graphene under the application of linear laser field and static electric field with $\theta = 0$, the energy spectrum will form three Dirac cones (Figure 7.5-a). We have shown that laser rotation will cause rotation and splitting in the spectrum. The middle cone and the side cone both change aspect ratio as the laser changes angle θ. The change in the aspect ratio for the middle cone shows a great decline from $\theta = 0$ as the cone splits into two cones that rotates back to become one cone when the laser angle $\theta = \pi$ as seen in following Figure (7.6). The side cone change aspect ratio as well as rotating. At $\theta = \pi/2$, the middle cones and the side cones become identical with the same aspect ratio while the number and positions of Dirac cones and points change.

In this research we examine the spectrum to identify the type of the cones and the connection between the upper and lower bands. This can be achieved by taking a cut along both axis k_x & k_y (Figure 7.8). The middle cone is found to form a parabolic cone showing a line connection between the upper and the lower bands (Figure 7.8-a&b). The side cone is found to be a Dirac cone with one Dirac point and an aspect ratio of 1.8:1.

(a)   (b)
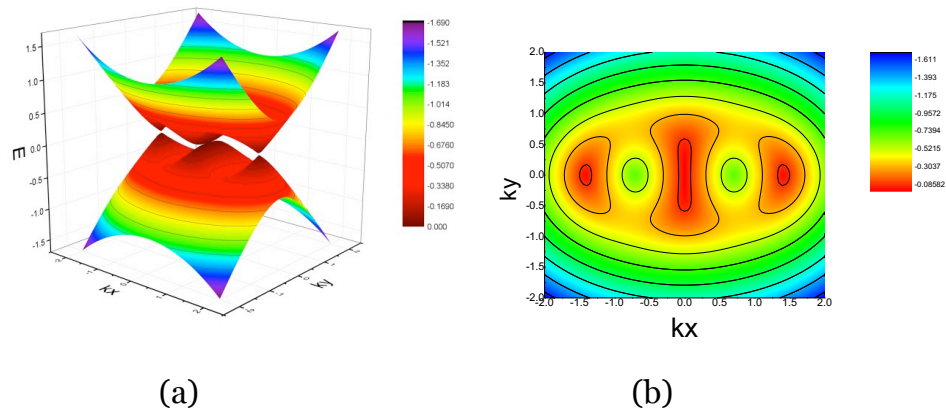
Figure 7.6 The energy spectrum $\varepsilon(k_x, k_y)$ of graphene under the application of linearly polarised laser and static electric filed for a chosen orientation $\theta = 0$ considering $\omega = 1$, $\mu = 1$, $U_0 = 1$ and $A_0 = 1$ (a) the upper and the lower bands touch in three areas: two side cones and an ellipse at the centre (b) the counter plot showing the three ellipses to be oriented parallel to k_x at $k_y = 0$
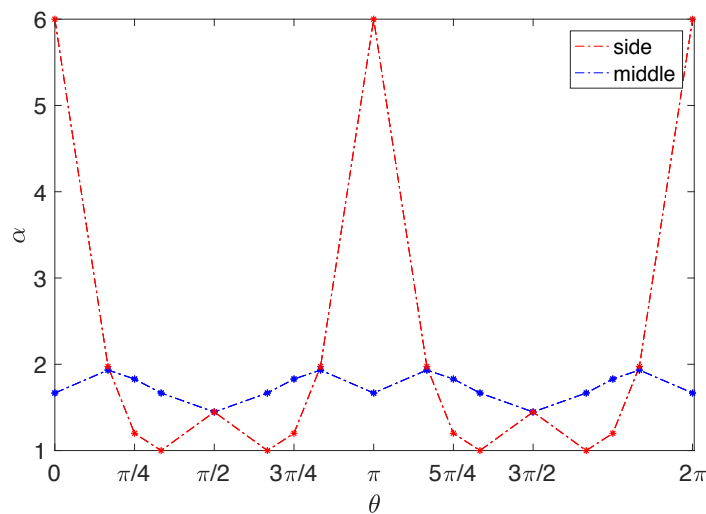
Figure 7.7 The aspect ratio of the side and middle cones α as a function of the laser angle θ

91

(a)

(b)

(c)
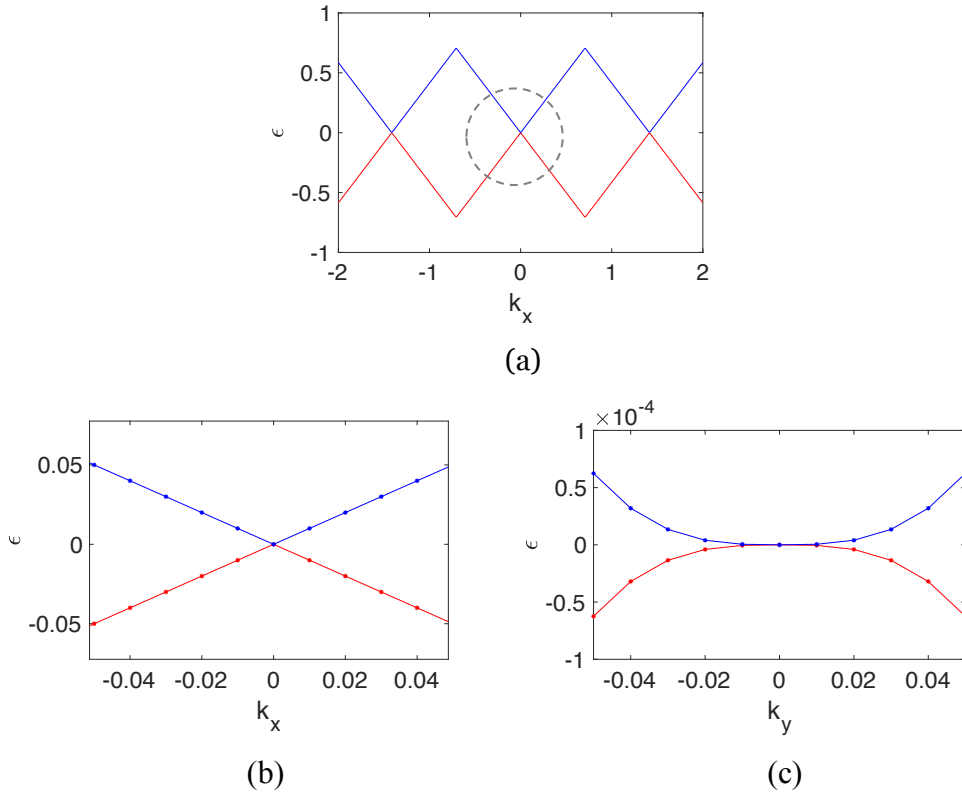
Figure 7.8 The $\varepsilon(k_x, k_y)$ cut of graphene in 2D along the k_x axis (a) showing the three touching points where $\varepsilon(k_x, k_y) = 0$ (b) the middle zero energy cone zoomed to show the connection point between the upper and the lower bands (c) the same scale for the zoomed cone showing the cone to be parabolic along the k_y axis.

7.3 SLG in static electric field and LPL in different frequencies and amplitudes

As we change the frequency or amplitude of the laser, the spectrum has been found to form Dirac cones (Appendix 2). The positions of the Dirac points are the same for the same pairs for $\omega = A_0$ (Figure 7.9) although the spectrum cone aspect ratio varies in the change of the frequency from the change in the amplitude (Figure 7.10). It shows a firmer parabolic curve around the value $A_0 = 1$, which can be the transition point where the dispersion relation changes to nonlinear

dependency of the external electric field. Such an effect results in breaking the symmetry of the energy spectrum.

(a)   (b)
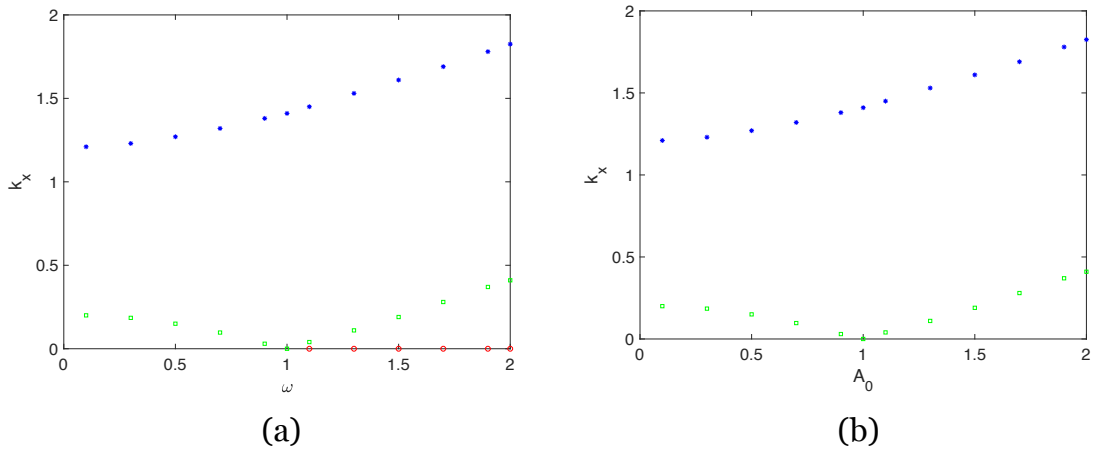
Figure 7.9 The positions of Dirac points on the spectrum where energy =0 in LPL and SPE giving Dirac cones for all ω and A_0. The different colours represent different Dirac points pairs
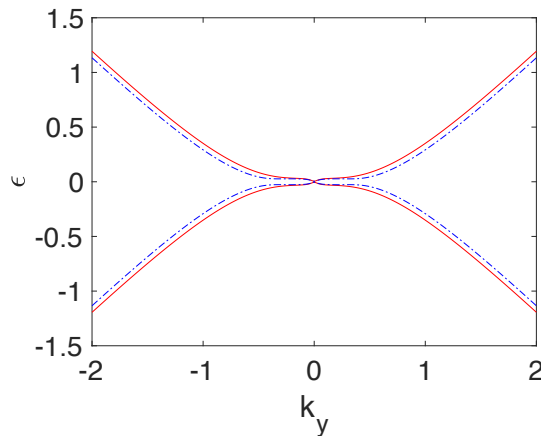
Figure 7.10 The energy spectrum of SLG in the application of SPE and LPL for two different laser parameters ω & A_0 showing both cases to have the same Dirac point and different cone aspect ratio. The solid lines present the upper and lower bands when the laser is set to $\omega = 0.9$ & $A_0 = 1$. The dashed lines give the upper and lower bands for laser settings $\omega = 1$ & $A_0 = 0.9$

Plotting the spectrum in 3D as the frequency of the laser changes (Figure 7.11) shows that at $\omega = 1.5$ the upper and lower bands are connected in 6 positions; 4 on the centre loop and two on the side cones. The connection on the centre at the points $(k_x, k_y) = (\pm 0.19, 0)$ represents Dirac points as well as $(k_x, k_y) = (0, \pm 0.56)$ (Appendix 3).

The change in the shape of the spectrum forms an evolving 2 pairs of Cassini ovals for frequencies smaller than the parabolic point, while for higher frequencies the spectrum forms 1 pair of Cassini ovals and one middle loop. As the frequency increases the deformation in the middle loop increases as Dirac points (see Figures 7.11 & 7.12)
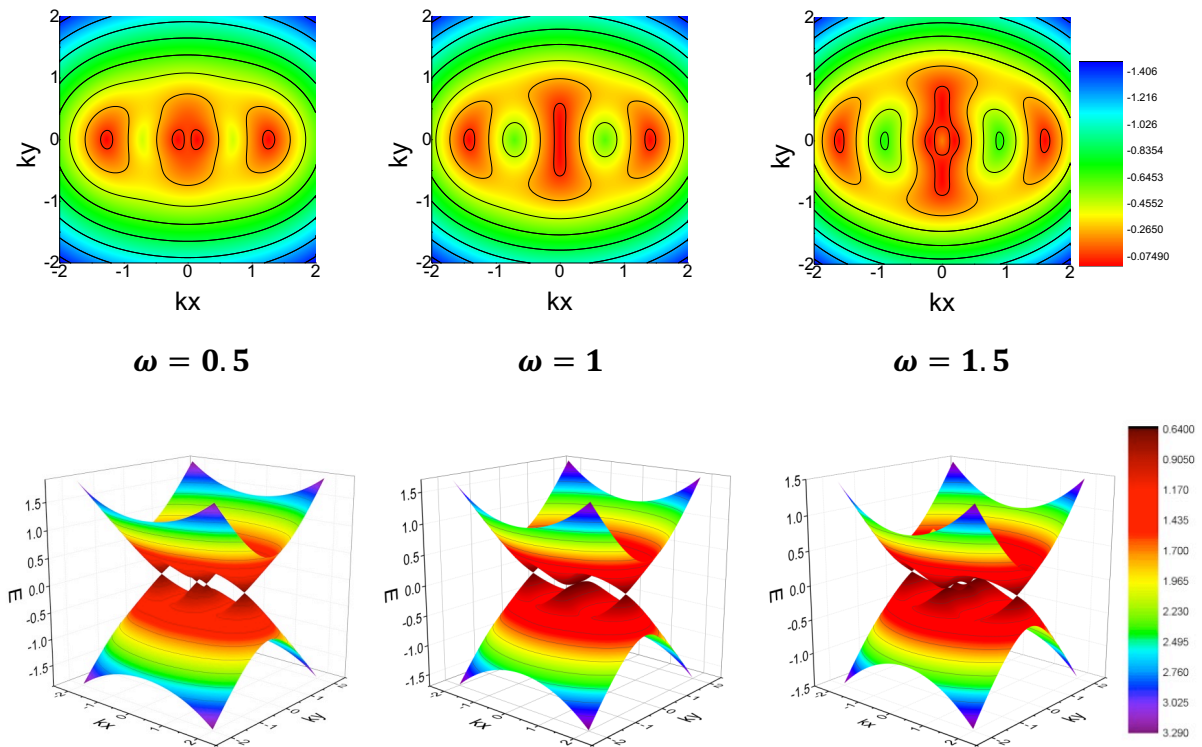
Figure 7.11 The change in the shape and the zero points energy points in graphene spectrum under the application of static electric field and linearly polarised laser with different frequencies.

94
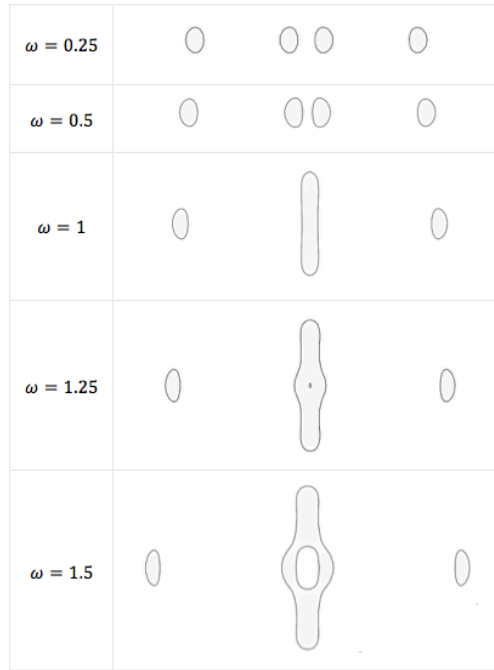
Figure 7.12 The deformation in graphene spectrum under the application of static electric field and linearly polarised laser with different laser's frequencies

This change can be used to change Dirac points. The shift in the spectrum applies to the shape and number of the cones as well as the position and numbers of Dirac points. Since the dispersion relation in the vicinity of K points in directly and strongly dependent on the symmetry of the graphene spectrum, the gap opening can be completely obtained through the broken symmetry.

The energy spectrum responds to the change in the laser's amplitude by shifting and splitting in the zero energy points. A decrease in the spacing between the valence and the conduction band results from applying a laser with small intensity. The increase in the laser's amplitude increases the distance between the valence and the conduction bands, however, the number of Dirac points does not change in amplitude alteration (see Figure 7.13). In addition, the cones represent Dirac cones at all amplitudes (Appendix 4).
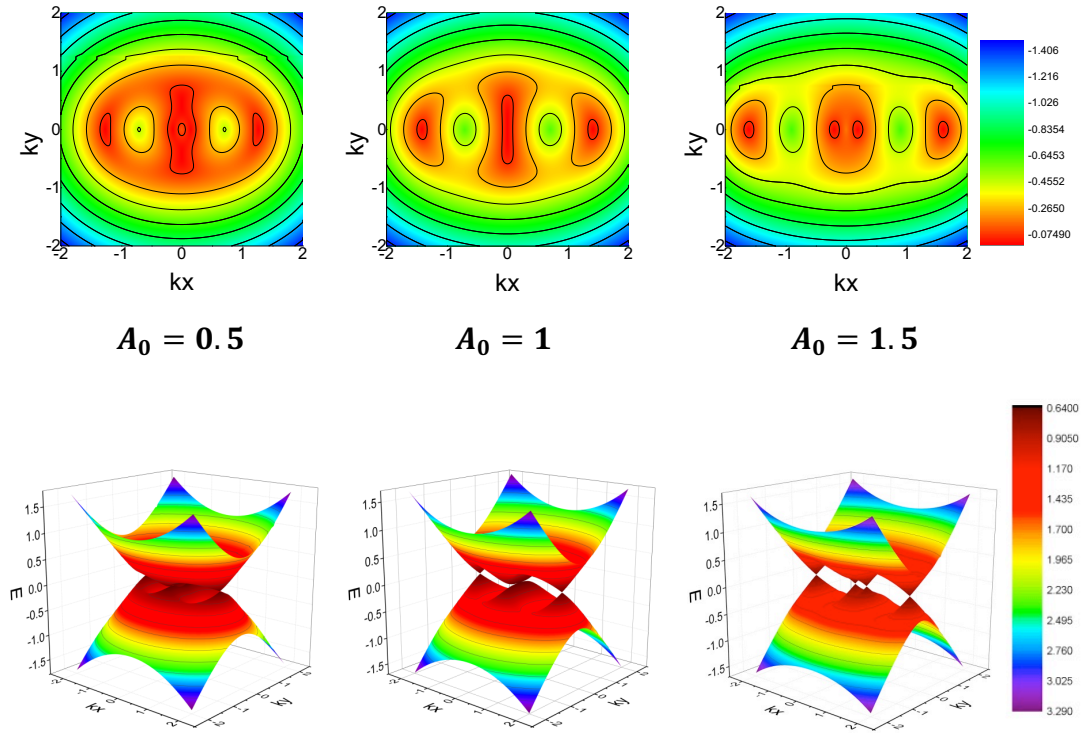
Figure 7.13 The change in the shape and the cones of graphene spectrum under the application of static electric field and linearly polarised laser with different amplitudes $A_0 = 0.5, 1, 1.5$ in units of $\frac{\pi}{T}$ showing different cones and different Dirac points.

The deformation in the spectrum energy as a result of the change in the lasers' amplitude can be seen in Figure (7.14). Such as the spectrum forms perfect Dirac cones with small aspect ratio at high laser amplitude. Whereas at low amplitudes, the cones deform and expand as a one loop. The number of zero energy points however remains constant.

$A_0 = 0.15$	
$A_0 = 0.25$	
$A_0 = 0.5$	
$A_0 = 1$	
$A_0 = 1.25$	
$A_0 = 1.5$	
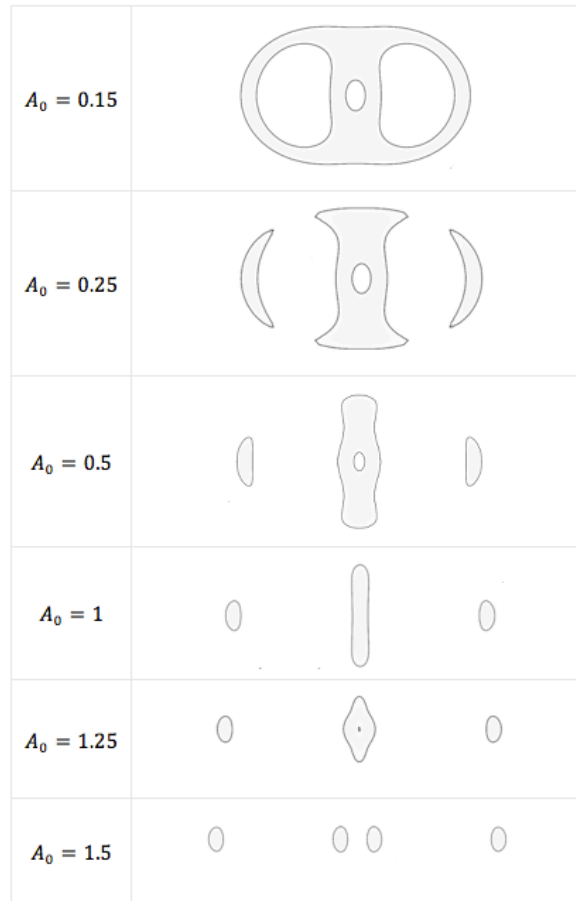
Figure 7.14 The splitting in graphene spectrum under the application of static electric field and linearly polarised laser with different laser's amplitudes

Preparing this module for practical application requires the investigation of a detectable quantity such as the single particle currents in graphene. j_i operator can be calculated (with components in x and y) at chosen laser orientation and wave vector $\vec{k} = \sqrt{k_x, k_y}$, where the current operator is given by:

$$j_i = \psi^* \sigma_i \psi \qquad (7.3)$$

(see examples in Appendixes 5).

97

7.4 Time and space shift symmetry breaking

This system can be shown to be symmetric under time inversion or space inversion or both by solving Schrodinger equation and reproducing the energy bands (FIG 19). With time and space shift the symmetry of the system is broken, we chose a shift of half period (FIG 20).

(a)

(b)

(c)

(d)
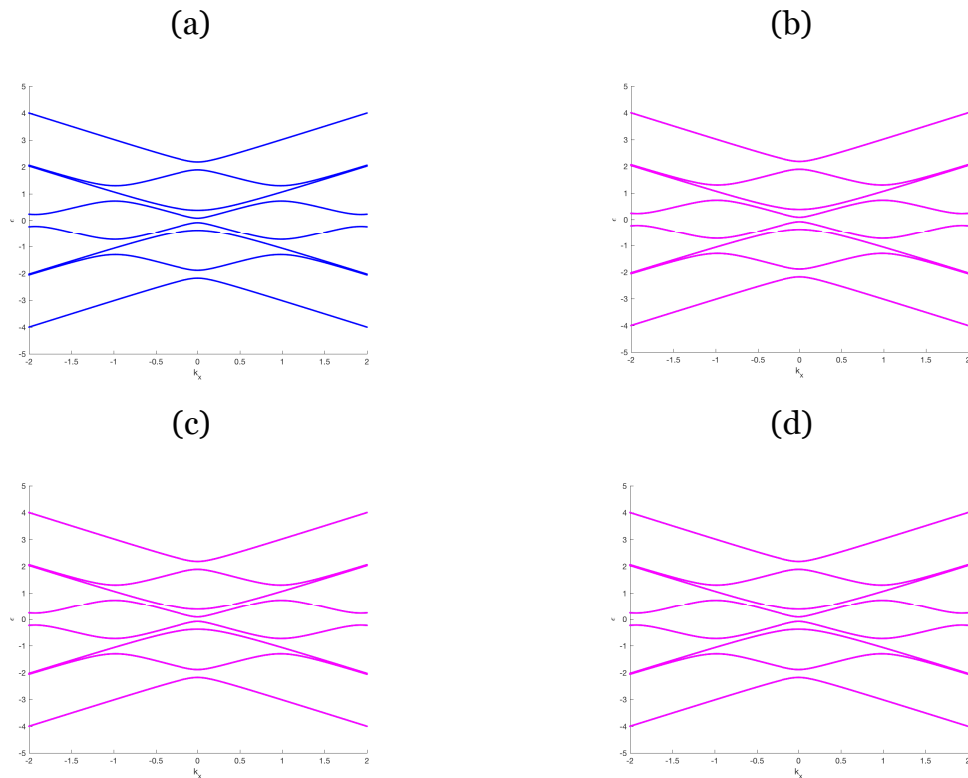
Figure 7.15 The symmetry of energy spectra of graphene in LPL and SPE (a) in the units of π/T, considering $\omega = 1$, $U_o = 1$ and $A_0 = 1$ for a chosen orientation of the laser ($\theta = 0$). (b) The spectra under time inversion $t \to -t$. (c) Space inversion $x \to -x$. (d) Time and space inversion. The spectra of the system are symmetric under these inversions

Applying a laser field in the existence of an electric filed parallel to graphene sheet causes a transformation of the Dirac dispersion relation in the vicinity of K point. Such transformation can cause a gap opening at K points if the laser applied is of a high intensity. The dispersion relation becomes more nonlinear as the

intensity increases. It is suggested that the nonlinearity in the Dirac-type dispersion relation transforms the massless Dirac to massive fermions [97].

(a)

(b)

(c)

(d)
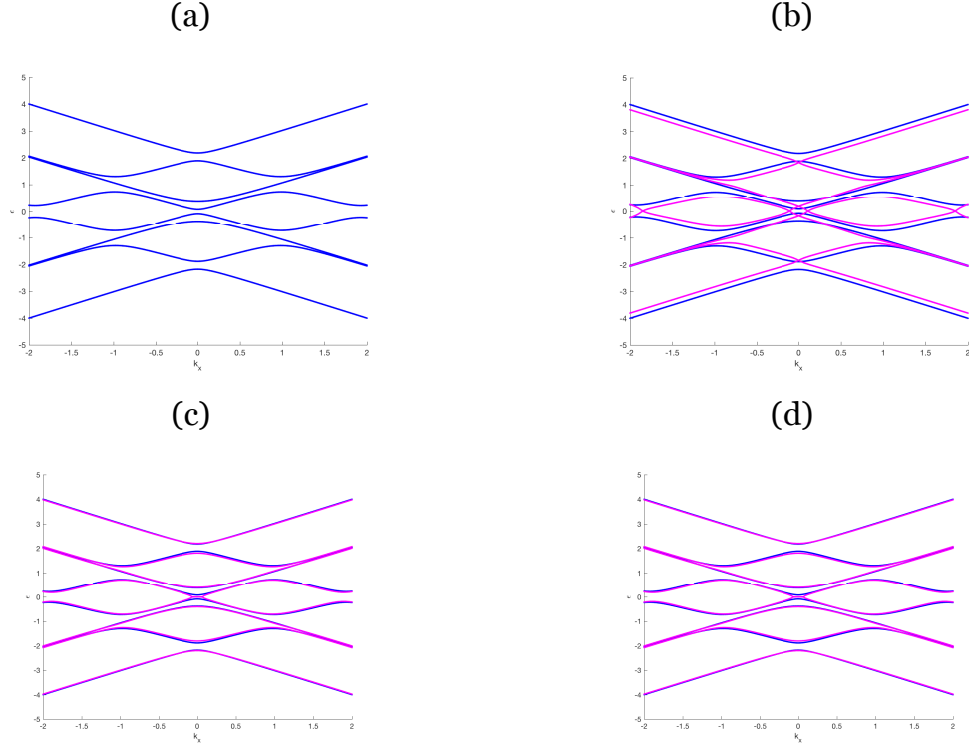
Figure 7.16 The symmetry of the energy spectra of graphene in LPL and SPE in the units of π/T, (a) considering $\omega = 1$, $U_0 = 1$ and $A_0 = 1$ for a chosen orientation of the laser ($\theta = 0$). (b) The spectra under time shift $t \to t + \frac{\pi}{2}$, being symmetric. (c) Space inversion $x \to x + \frac{\pi}{2}$, showing a break in symmetry. (d) Time and space shift introduces symmetry breaking

7.5 Summary

This chapter introduces the module of single layer graphene in the application of linearly polarised laser field and spatially periodic electric field. Overall, this investigation highlighted the relativistic properties of graphene by changing the Dirac-Cone spectrum of charge carriers. The theoretical modification of the spectrum is approached by applying high-frequency laser fields in the presence of

static electric/magnetic fields. The number of Dirac points, the shape of Dirac cones and the gap in spectrum can all be controlled by changing the laser's parameters. The energy spectrum in graphene exhibit a topological phase transition. In the vicinity of the original K and K' Dirac points, pairs of Weyl-Dirac cones are formed.

A symmetry breaking is introduced due to the application of the two fields. The rotation of the laser creates additional symmetry breaking as additional pairs of the Weyl-Dirac cones are formed in the spectrum. If the modulated electric field is fixed, tilting the laser alone can control the effect induced in the spectrum.

The change in the frequency and the amplitude of the laser result in a deformation of the energy spectrum. Different pairs and shapes of Cassini ovals induce in the spectrum indicating a symmetry breaking. Such effect causes a gap opening at the K points if the applied laser is of a high intensity. The nonlinearity in the Dirac dispersion relation increases furthermore with the increase in the laser amplitude.

In different potentials the spectrum shows different anisotropy, which can be further changed in specific potentials applications by changing their parameters. Thus, the modification of the anisotropy of the Dirac cone causes destruction/creation of Dirac points, hence electron transport can be modified. We showed that anisotropic transport in monolayer graphene can be controlled by changing high-frequency lasers' parameters, which even allow generation of infinite anisotropy.

Such module can be highly efficient in controlling the splitting and creation of Dirac points in the single layer graphene. Furthermore, it can create novel properties for optoelectronic devices.

8 Summary and Conclusion

The general aim of this research is to theoretically investigate the manipulation of Dirac points in the single layer graphene by studying electron spectra in graphene superlattice in Floquet-Bloch states under the application of different periodic potential.

An introduction to the topic is provided in **Chapter 1**, in addition to the aim and motivation of this research as the demonstration of graphene in 2004 has opened great research and application opportunities.

Chapter 2 provides an overall background to graphene structure and its properties. The one layer of carbon atoms in a honeycomb crystal allowed the applications and testing of quantum theories and behaviours. Graphene has shown so far extraordinary properties, such as high electrical and thermal conductivity, transparency and flexibility. Graphene can be produced in small quantities with almost perfect structure (exfoliation or epitaxial growth), or in huge quantities with some defect (chemical vapour deposition). This gapless band structure is not the reason of graphene being unique, but graphene's quantum behaviour in room temperature is rather remarkable such as: anomalous Quantum Hall Effect and perfect Klein tunneling. Therefore, graphene based devices are an attractive subject for research and application.

Chapter 3 reviewed in details the energy band structure of graphene, which was described a long before was actually produced in a free state. It has a gapless band structure at six Dirac points, where electrons transport within two sublattices with hopping process. The energy spectrum of graphene is well described using Bloch wave

in the tight binding model using Dirac equation. The development of these devices is based on the improvement of gap creation and control in the graphene band structure. Graphene can be widely applied due to its properties to form carbon nanotubes, nanoribbons, sensors, transistors and many photonic devices. Gap induction is an essential requirement for using graphene in electronic application. It has to be noted that the gap induction method could affect the novel properties of graphene, thus affecting its capability as high mobility material. Within this context, graphene superlattices are of a great focus for theoretical and experimental investigation. They are mainly used to understand the gap opening and Dirac points emerging in graphene near zero energy. The application of external field is an essential element in such development; therefore, the energy spectrum of graphene in some field is investigated in this research.

Chapter 4 illustrated the theoretical calculating to obtain the energy spectrum of graphene superlattices. In graphene the behaviour of charge carries can be demonstrated by the 2D Dirac equation. The solution of the Dirac Hamiltonian can become a simple eigen value problem using Floquet theory. The theory assists in transforming periodic dynamical systems into linear forms by solving Schrödinger equation. The obtained solution can be approximated to exclude resonance terms. The final solution can be found analytically or numerically to produce the energy spectrum of graphene.

Chapter 5 reviewed an investigated the gap opening in single layer graphene SLG in a single field application using three potentials; 1-lineraly polarised laser LPL, 2- circularly polarised laser CPL, and 3- static electric field SE. We concluded from the investigation that the gap opening in the graphene spectrum is determined by the polarization of the laser. For the linearly polarised laser, the spectrum has no gap opening at any laser parameter, while in the circularly polarised laser, the spectrum developed a gap energy at all laser parameters. In the application of time periodic electric filed, energy gap cannot be induced in the spectrum of graphene. In the application of electric field alone, the sublattices remains equivalent which does not break the topological symmetry of the energy dispersion.

Chapter 6 examined two different theoretical modules for spectrum manipulation in single layer graphene. In the first, a spatially periodic magnetic field is vertically applied to a single layer graphene sheet. The spectrum showed Dirac cones at zero energy points, with stationary states elsewhere which indicates decaying states.

The other module proposes the duality of a linear polarised laser in the application of a vertical static magnetic field. The static magnetic field hand transforms the electron spectra into mini bands. Overall, it was found that changing in the laser's parameters is enough to produce different Dirac points' dynamics while the topological symmetry of the spectrum is preserved. There in the vicinity of the original K and K' Dirac points the pairs of Weyl-Dirac cones are created. Then the graphene layer may be viewed as two-dimensional Weyl metal. The created Weyl metal energy spectrum is invariant under the laser field rotation when there is only spatial modulation of magnetic field. In addition, the change in the laser frequency and amplitude provided different Cassini ovals in the energy spectrum that should further splitting and creation of Dirac points indicating a further symmetry breaking and a controllable anisotropy.

Chapter 7 presented duality of linear polarised laser and static electric filed which was applied in plane to the single graphene sheet. We showed that static periodically modulated electric field together with linearly polarised laser field induce dynamical topological phase transitions in a single graphene layer. However, when the static electric field is periodically modulated, the system shows additional symmetry breaking phenomenon where additional pairs of the Weyl-Dirac cones are created. We show that this effect is controlled by a laser field tilting from the graphene plane where the modulated electric field is embedded. The change in the other laser parameters proposes high deformation in the spectrum cones slowing different anisotropic transport. Additionally, manipulation of electron current in graphene is allowed by laser-field-controlled band structures.

We expect that these modules may be used in novel optoelectronic devices and the predicted phenomena will be observed in the future experiments. In practice, applying a small DC electric field can induce the pseudo-periodic $\varepsilon(k_x(t))$ Bloch oscillations. The predicted spectrum in this study can be experimentally measured, directly, by applying a weak probe field in additional to static fields. The duality between the electron spectrum in time-periodic laser fields and spatially periodic electrostatic fields offers an experimental approach to spatially periodic graphene superlattices [30].

References

[1] K. S. Novoselov *et al.*, "Electric field effect in atomically thin carbon films," *Science (80-.).*, vol. 306, no. 5696, pp. 666–669, 2004.

[2] J. C. Meyer, A. K. Geim, M. I. Katsnelson, K. S. Novoselov, T. J. Booth, and S. Roth, "The structure of suspended graphene sheets," *Nature*, vol. 446, no. 7131, p. 60, 2007.

[3] A. K. Geim, "Graphene: status and prospects," *Science (80-.).*, vol. 324, no. 5934, pp. 1530–1534, 2009.

[4] J. Gizmodo, "5 Crazy New Man-Made Materials That Will Shape the Future," 2013. [Online]. Available: http://gizmodo.com/5-of-the-craziest-new-man-made-materials-893364032. [Accessed: 11-Jul-2018].

[5] A. K. Geim and K. S. Novoselov, "The rise of graphene," *Nanosci. Technol. A Collect. Rev. from Nat. Journals*, pp. 11–19, 2010.

[6] A. O'Hare, F. V. Kusmartsev, and K. I. Kugel, "A Stable "Flat″ Form of Two-Dimensional Crystals: Could Graphene, Silicene, Germanene Be Minigap Semiconductors?," *Nano Lett.*, vol. 12, no. 2, pp. 1045–1052, 2012.

[7] K. S. Novoselov *et al.*, "Room Temperature Quantum Hall Effect in Graphene," *Science (80-.).*, vol. 315, no. 5817, pp. 1379–1379, 2007.

[8] B. Trauzettel, D. V. Bulaev, D. Loss, and G. Burkard, "Spin qubits in graphene quantum dots," *Nat. Phys.*, vol. 3, no. 3, p. 192, 2007.

[9] S. Chen *et al.*, "Thermal conductivity of isotopically modified graphene," *Nat. Mater.*, vol. 11, no. 3, pp. 203–207, 2012.

[10] A. C. Neto and K. Novoselov, "New directions in science and technology: Two-dimensional crystals," *Reports Prog. Phys.*, vol. 74, no. 8, p. 082501, 2011.

[11] J. Rafiee *et al.*, "Wetting transparency of graphene," *Nat. Mater.*, vol. 11, no. 3, pp. 217–222, 2012.

[12] S. Pei and H. M. Cheng, "The reduction of graphene oxide," *Carbon N. Y.*, vol. 50, no. 9, pp. 3210–3228, 2012.

[13] V. Georgakilas *et al.*, "Functionalization of graphene: Covalent and non-covalent approaches, derivatives and applications," *Chem. Rev.*, vol. 112, no. 11, pp. 6156–6214, 2012.

[14] J. Bai, X. Zhong, S. Jiang, Y. Huang, and X. Duan, "Graphene nanomesh," *Nat. Nanotechnol.*, vol. 5, no. 3, pp. 190–194, 2010.

[15] T. Fang, A. Konar, H. Xing, and D. Jena, "Mobility in semiconducting graphene nanoribbons: Phonon, impurity, and edge roughness scattering," *Phys. Rev. B*, vol. 78, no. 20, p. 205403, 2008.

[16] A. V. Rozhkov, S. Savel'ev, and F. Nori, "Electronic properties of armchair graphene nanoribbons," *Phys. Rev. B*, vol. 79, no. 12, p. 125420, 2009.

[17] R. Quhe *et al.*, "Tunable and sizable band gap of single-layer graphene sandwiched between hexagonal boron nitride," *NPG Asia Mater.*, vol. 4, no. 2, p. e6, 2012.

[18] T. M. Lu, D. Laroche, S. H. Huang, Y. Chuang, J. Y. Li, and C. W. Liu, "High-mobility capacitively-induced two-dimensional electrons in a lateral superlattice potential," *Sci. Rep.*, vol. 6, no. 11, p. 20967, 2016.

[19] S. M. Choi, S. H. Jhi, and Y. W. Son, "Effects of strain on electronic properties of graphene," *Phys. Rev. B*, vol. 81, no. 8, p. 081407, 2010.

[20] Y. P. Bliokh, V. Freilikher, S. Savel'ev, and F. Nori, "Transport and localization in periodic and disordered graphene superlattices," *Phys. Rev. B*, vol. 79, no. 7, p. 075123, 2009.

[21] T. G. Pedersen, C. Flindt, J. Pedersen, N. A. Mortensen, A. P. Jauho, and K. Pedersen, "Graphene antidot lattices: Designed defects and spin qubits," *Phys. Rev. Lett.*, vol. 100, no. 13, p. 136804, 2008.

[22] J. C. W. Song, A. V. Shytov, and L. S. Levitov, "Electron interactions and gap opening in graphene superlattices," *Phys. Rev. Lett.*, vol. 111, no. 26, p. 266801, 2013.

[23] H. T. Grahn, *Semiconductor superlattices: growth and electronic properties.* World Scientific, 1995.

[24] K. N. Alekseev, E. H. Cannon, J. C. McKinney, F. V. Kusmartsev, and D. K. Campbell, "Symmetry-breaking and chaos in electron transport in semiconductor superlattices," *Phys. D Nonlinear Phenom.*, vol. 113, no. 2–4, pp. 129–133, 2001.

[25] V. M. Pereira, A. H. Castro Neto, and N. M. . R. Peres, "Tight-binding approach to uniaxial strain in graphene," *Phys. Rev. B*, vol. 80, no. 4, p. 045401, 2009.

[26] G. Gui, J. Li, and J. Zhong, "Band structure engineering of graphene by strain:

First-principles calculations," *Phys. Rev. B*, vol. 78, no. 7, p. 075435, 2008.

[27] F. Xia, D. B. Farmer, Y. M. Lin, and P. Avouris, "Graphene Field-Effect Transistors with High On / Off Current Ratio and Large Transport Band Gap at Room Temperature," *Nano Lett.*, vol. 10, no. 2, pp. 715–718, 2010.

[28] Y. Zhang *et al.*, "Direct observation of a widely tunable bandgap in bilayer graphene," *Nature*, vol. 459, no. 7248, pp. 820–823, 2009.

[29] J. B. Oostinga, H. B. Heersche, X. Liu, A. F. Morpurgo, and L. M. Vandersypen, "Gate-induced insulating state in bilayer graphene devices," *Nat. Mater.*, vol. 7, no. 2, pp. 151–157, 2008.

[30] S. E. Savel'Ev and A. S. Alexandrov, "Massless Dirac fermions in a laser field as a counterpart of graphene superlattices," *Phys. Rev. B - Condens. Matter Mater. Phys.*, vol. 84, no. 3, p. 035428, 2011.

[31] P. Rodriguez-Lopez, J. J. Betouras, and S. E. Savel'ev, "Dirac fermion time-Floquet crystal: manipulating Dirac points," *Phys. Rev. B*, vol. 89, no. 15, p. 155132, 2014.

[32] P. R. Wallace, "The band theory of graphite," *Phys. Rev.*, vol. 71, no. 9, p. 622, 1947.

[33] A. K. Geim and A. H. MacDonald, "Graphene: Exploring carbon flatland," *Phys. Today*, vol. 60, no. 8, 2007.

[34] A. K. Geim, "Graphene prehistory," *Phys. Scr.*, vol. T146, p. 014003, 2012.

[35] G. M. Scheuermann, L. Rumi, P. Steurer, W. Bannwarth, and R. Mülhaupt, "Palladium nanoparticles supported on amino functionalized metal-organic frameworks as highly active catalysts for the Suzuki – Miyaura cross-coupling reaction," *J. Am. Chem. Soc.*, vol. 131, no. 23, pp. 8262–8270, 2009.

[36] K. S. Novoselov, "Graphene: Materials in the Flatland," *Rev. Mod. Phys.*, vol. 83, no. 3, pp. 837–849, 2011.

[37] D. R. Dreyer, R. S. Ruoff, and C. W. Bielawski, "From Conception to Realization   : An Historial Account of Graphene and Some Perspectives for Its Future," *Angew. Chemie Int. Ed.*, vol. 49, no. 49, pp. 9336–9344, 2010.

[38] S. Gilje, S. Han, M. Wang, K. L. Wang, and R. B. Kaner, "A Chemical Route to Graphene for Device Applications," *Nano Lett.*, vol. 7, no. 11, pp. 3394–3398, 2007.

[39] Y. Kopelevich and P. Esquinazi, "Graphene physics in graphite. Advanced Materials," vol. 19, no. 24, pp. 4559–4563, 2007.

[40] A. M. Zagoskin, *Quantum engineering: theory and design of quantum coherent structures*. Cambridge University Press, 2011.

[41] M. I. Katsnelson, "Graphene: carbon in two dimensions," *Mater. today*, vol. 10,

no. 1–2, pp. 20–27, 2007.

[42]   M. O. Goerbig, "Electronic properties of graphene in a strong magnetic field," *Rev. Mod. Phys.*, vol. 83, no. 4, p. 1193, 2011.

[43]   A. C. Neto, F. Guinea, N. M. Peres, K. S. Novoselov, and A. K. Geim, "The electronic properties of graphene," *Rev. Mod. Phys.*, vol. 81, no. 1, p. 109, 2009.

[44]   P. Alonso-González *et al.*, "Controlling graphene plasmons with resonant metal antennas and spatial conductivity patterns," *Science (80-.).*, vol. 344, no. 6190, pp. 1369–1373, 2014.

[45]   M. Orlita *et al.*, "Approaching the Dirac point in high mobility multilayer epitaxial graphene," *Phys. Rev. Lett.*, vol. 101, no. 26, p. 267601, 2008.

[46]   D. A. Areshkin, D. Gunlycke, and C. T. White, "Ballistic Transport in Graphene Nanostrips in the Presence of Disorder   : Importance of Edge Effects," *Nano Lett.*, vol. 7, no. 1, pp. 204–210, 2007.

[47]   M. E. Umarol *et al.*, "Direct nanoscale imaging of ballistic and diffusive thermal transport in graphene nanostructures," *Nano Lett.*, vol. 12, no. 6, pp. 2906–2911, 2012.

[48]   K. C. Yung, W. M. Wu, M. P. Pierpoint, and F. V. Kusmartsev, "Introduction to Graphene Electronics – A New Era of Digital Transistors and Devices," *Contemp. Phys.*, vol. 54, no. 5, pp. 233–251, 2013.

[49]   K. I. Bolotin, K. J. Sikes, J. Hone, H. L. Stormer, and P. Kim, "Temperature-dependent transport in suspended graphene," *Phys. Rev. Lett.*, vol. 101, no. 9, p. 096802, 2008.

[50]   P. Avouris, "Graphene: electronic and photonic properties and devices," *Nano Lett.*, vol. 10, no. 11, pp. 4285–4294, 2010.

[51]   F. Schwierz, "Graphene transistors," *Nat. Nanotechnol.*, vol. 5, no. 7, p. 487, 2010.

[52]   C. Cookson, "Graphene: Faster, stronger, bendier," 2013. [Online]. Available: http://ig-legacy.ft.com/content/6f4717b6-66f9-11e2-a83f-00144feab49a#axzz3CoC5SsZx. [Accessed: 12-Jul-2018].

[53]   K. S. Novoselov *et al.*, "Two-dimensional gas of massless Dirac fermions in graphene," *Nature*, vol. 438, no. 7065, p. 197, 2005.

[54]   W. A. De Heer *et al.*, "Epitaxial graphene," *Solid State Commun.*, vol. 143, no. 1–2, pp. 92–100, 2007.

[55]   Y. Iyechika, "Application of graphene to high-speed transistors: expectations and challenges," *NISTEP Sci. Technol. Foresight Cent.*, 2010.

[56]   A. B. G. Trabelsi, A. Ouerghi, O. E. Kusmartseva, F. V. Kusmartsev, and M.

Oueslati, "Raman spectroscopy of four epitaxial graphene layers: Macro-island grown on 4H-SiC 0001¯ substrate and an associated strain distribution," *Thin Solid Films*, vol. 539, pp. 377–383, 2013.

[57] A. Das *et al.*, "Monitoring dopants by Raman scattering in an electrochemically top-gated graphene transistor," *Nat. Nanotechnol.*, vol. 3, no. 4, p. nnano-2008, 2008.

[58] C. Berger *et al.*, "Electronic confinement and coherence in patterned epitaxial graphene," *Science (80-.).*, vol. 312, no. 5777, pp. 1191–1196, 2006.

[59] H. S. Song *et al.*, "Origin of the relatively low transport mobility of graphene grown through chemical vapor deposition," *Sci. Rep.*, vol. 2, p. 337, 2012.

[60] F. V. Kusmartsev and A. M. Tsvelik, "Semimetallic properties of a heterojunction.," *JETP lett*, vol. 42, no. 5, 1985.

[61] S. Bae *et al.*, "Roll-to-roll production of 30-inch graphene films for transparent electrodes," *Nat. Nanotechnol.*, vol. 5, no. 8, p. 574, 2010.

[62] C. Bena and G. Montambaux, "Remarks on the tight-binding model of graphene," *New J. Phys.*, vol. 11, no. 9, p. 095003, 2009.

[63] J. L. Mañes, F. Guinea, and M. A. Vozmediano, "Existence and topological stability of Fermi points in multilayered graphene," *Phys. Rev. B*, vol. 75, no. 15, p. 155424, 2007.

[64] R. D. Y. Hills, A. Kusmartseva, and F. V. Kusmartsev, "Current-voltage characteristics of Weyl semimetal semiconducting devices, Veselago lenses, and hyperbolic Dirac phase," *Phys. Rev. B*, vol. 95, no. 21, p. 214103, 2017.

[65] T. Kawasaki, T. Ichimura, H. Kishimoto, A. A. Akbar, T. Ogawa, and C. Oshima, "Double atomic layers of graphene/monolayer h-BN on Ni (111) studied by scanning tunneling microscopy and scanning tunneling spectroscopy," *Surf. Rev. Lett.*, vol. 9, no. 03n04, pp. 1459–1464, 2002.

[66] G. Giovannetti, P. A. Khomyakov, G. Brocks, P. J. Kelly, and J. Van Den Brink, "Substrate-induced band gap in graphene on hexagonal boron nitride: Ab initio density functional calculations," *Phys. Rev. B*, vol. 76, no. 7, p. 073103, 2007.

[67] P. Shemella and S. K. Nayak, "Electronic structure and band-gap modulation of graphene via substrate surface chemistry," *Appl. Phys. Lett.*, vol. 94, no. 3, p. 032101, 2009.

[68] S. Y. Zhou *et al.*, "Substrate-induced bandgap opening in epitaxial graphene," *Nat. Mater.*, vol. 6, no. 10, p. 770, 2007.

[69] L. Esaki and R. Tsu, "Superlattice and negative differential conductivity in semiconductors," *IBM J. Res. Dev.*, vol. 14, no. 1, pp. 61–65, 1970.

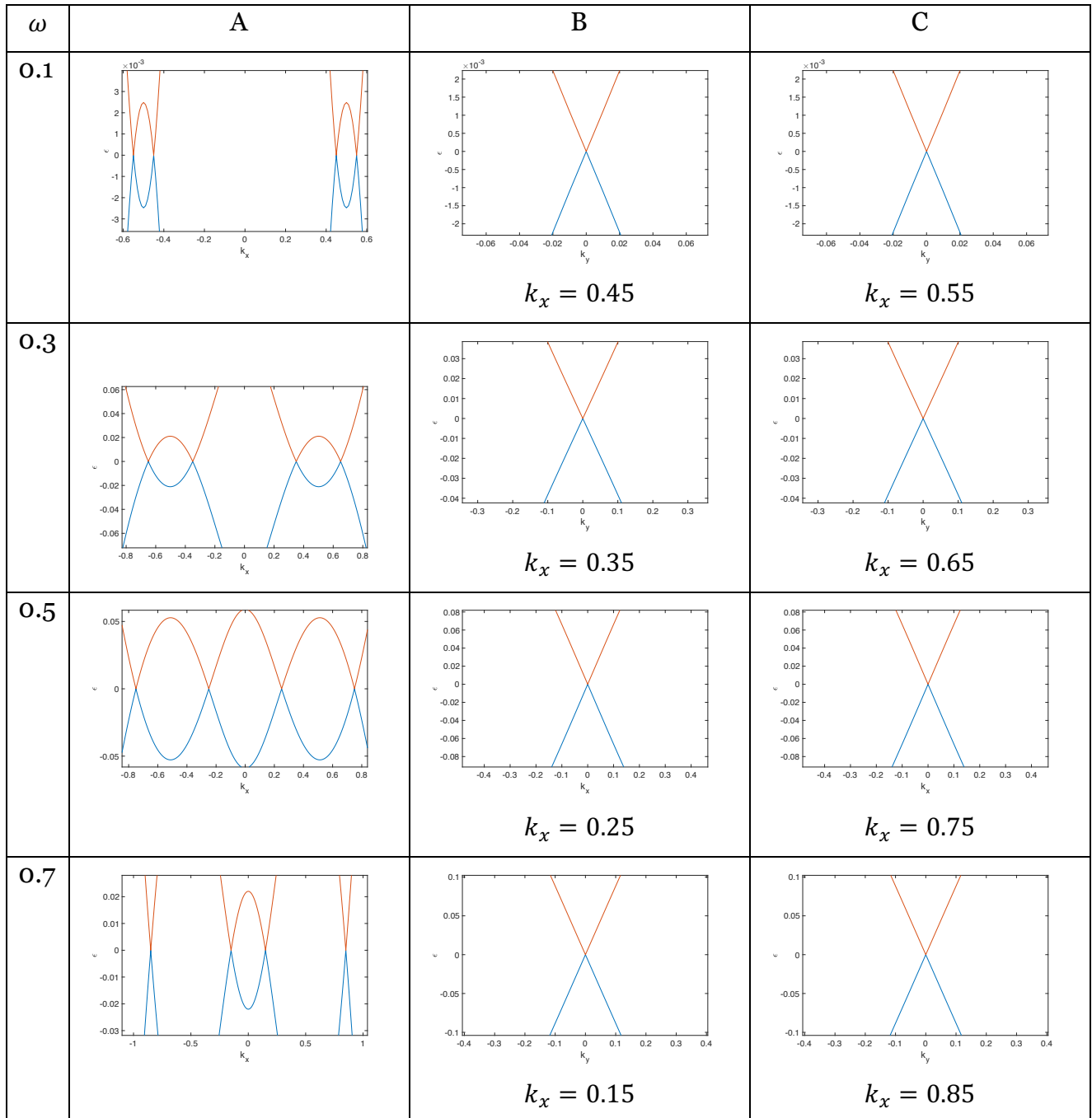[70] C. H. Park, L. Yang, Y. W. Son, M. L. Cohen, and S. G. Louie, "Anisotropic

behaviours of massless Dirac fermions in graphene under periodic potentials," *Nat. Phys.*, vol. 4, no. 3, p. 213, 2008.

[71] R. Tsu, *Superlattice to nanoelectronics*. Oxford: Elsevier, 2010.

[72] D. M. Eigler and E. K. Schweizer, "Positioning single atoms with a scanning tunnelling microscope," *Nature*, vol. 344, no. 6266, p. 524, 1990.

[73] H. Hiura, "Tailoring graphite layers by scanning tunneling microscopy," *Appl. Surf. Sci.*, vol. 222, no. 1–4, pp. 374–381, 2004.

[74] J. R. Williams, L. DiCarlo, and C. M. Marcus, "Quantum Hall effect in a gate-controlled pn junction of graphene," *Science (80-.).*, vol. 317, no. 5838, pp. 638–641, 2007.

[75] B. Huard, J. A. Sulpizio, N. Stander, K. Todd, B. Yang, and D. Goldhaber-Gordon, "Transport measurements across a tunable potential barrier in graphene," *Phys. Rev. Lett.*, vol. 98, no. 23, p. 236803, 2007.

[76] C. Bai and X. Zhang, "Klein paradox and resonant tunneling in a graphene superlattice," *Phys. Rev. B*, vol. 76, no. 7, p. 075430, 2007.

[77] M. Yankowitz *et al.,* "Emergence of superlattice Dirac points in graphene on hexagonal boron nitride," *Nat. Phys.*, vol. 8, no. 5, p. 382, 2012.

[78] P. Moon and M. Koshino, "Electronic properties of graphene/hexagonal-boron-nitride moiré superlattice," *Phys. Rev. B*, vol. 90, no. 15, p. 155406, 2014.

[79] M. R. Masir, P. Vasilopoulos, A. Matulis, and F. M. Peeters, "Direction-dependent tunneling through nanostructured magnetic barriers in graphene," *Phys. Rev. B*, vol. 77, no. 23, p. 235443, 2008.

[80] M. R. Masir, P. Vasilopoulos, and F. M. Peeters, "Tunneling, conductance, and wavevector filtering through magnetic barriers in bilayer graphene," *Phys. Rev. B*, vol. 79, no. 3, p. 035409, 2009.

[81] K. Kristinsson, O. V. Kibis, S. Morina, and I. A. Shelykh, "Control of electronic transport in graphene by electromagnetic dressing," *Sci. Rep.*, vol. 6, p. 20082, 2016.

[82] S. E. Savel'ev, W. Häusler, and P. Hänggi, "Current resonances in graphene with time-dependent potential barriers," *Phys. Rev. Lett.*, vol. 109, no. 22, p. 226602, 2012.

[83] L. G. Wang and S. Y. Zhu, "Electronic band gaps and transport properties in graphene superlattices with one-dimensional periodic potentials of square barriers," *Phys. Rev. B*, vol. 81, no. 20, p. 205444, 2010.

[84] L. Brey and H. A. Fertig, "Emerging zero modes for graphene in a periodic potential," *Phys. Rev. Lett.*, vol. 103, no. 4, p. 046809, 2009.
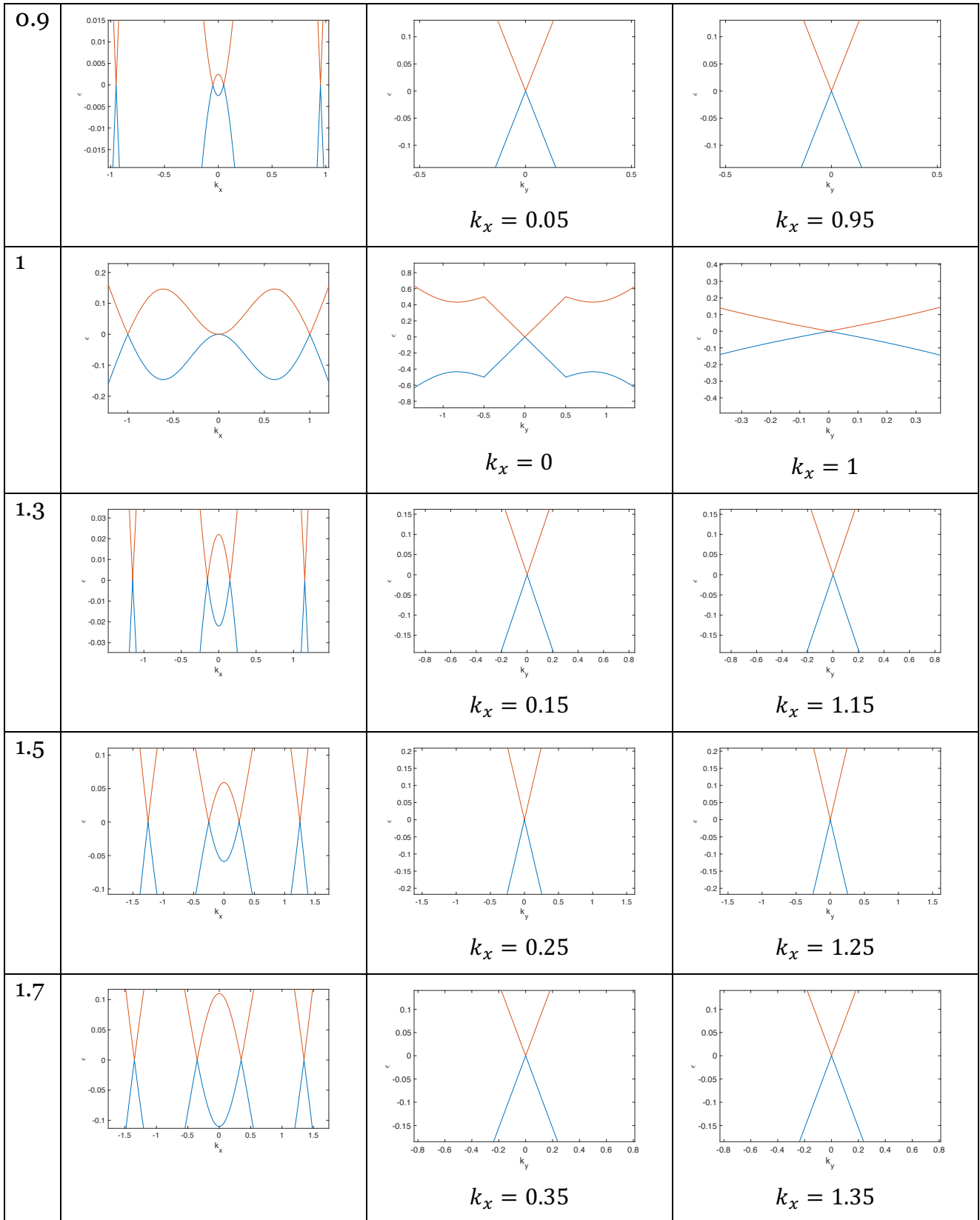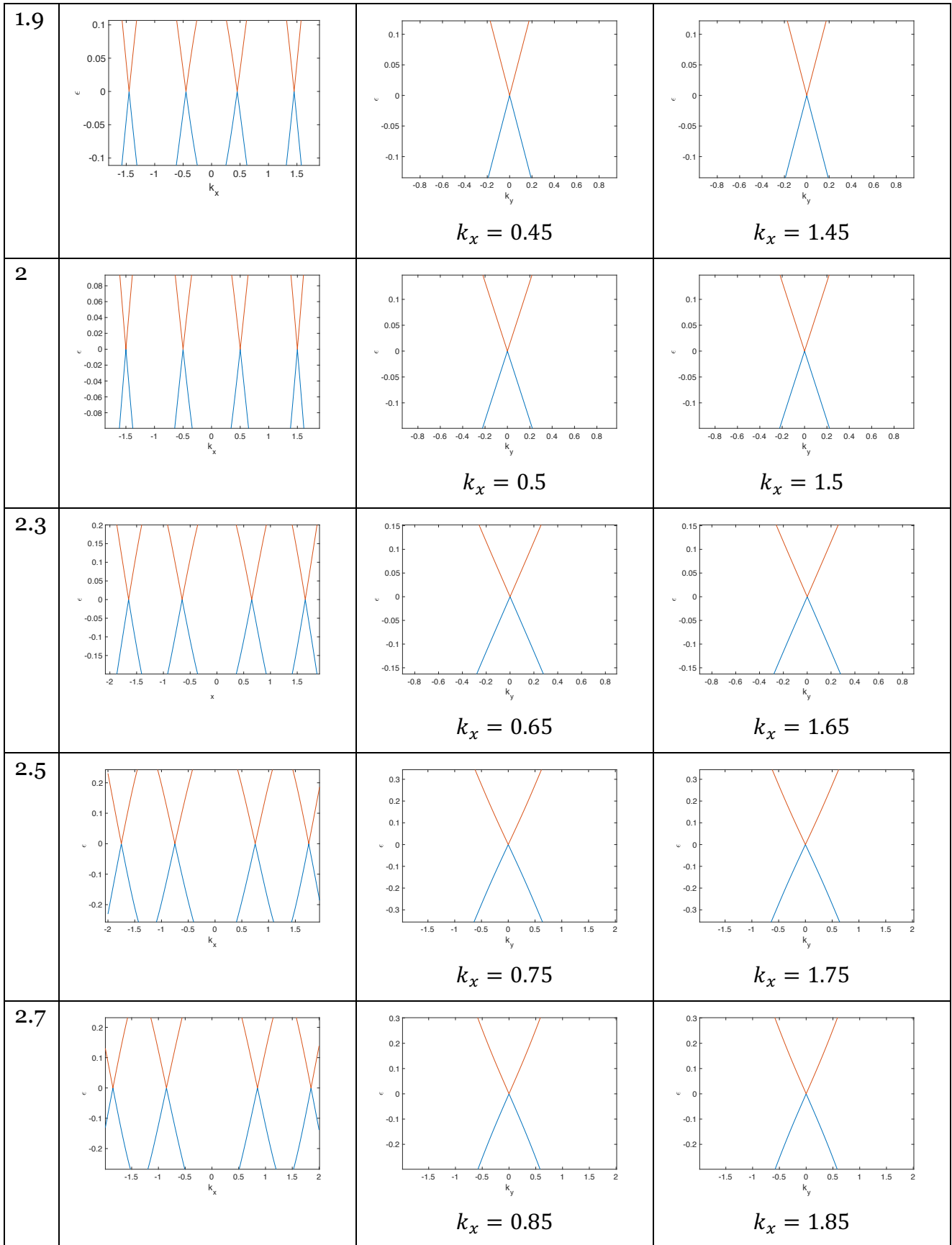
[85] W. Xiong, L. J. Jiang, T. Baldacchini, and Y. F. Lu, "Laser additive manufacturing using nanofabrication by integrated two-photon polymerization and multiphoton ablation," *Laser Addit. Manuf.*, pp. 237–256, 2017.

[86] T. Ando and T. Nakanishi, "Impurity scattering in carbon nanotubes–absence of back scattering," *J. Phys. Soc. Japan*, vol. 67, no. 5, pp. 1704–1713, 1998.

[87] D. P. DiVincenzo and E. J. Mele, "Self-consistent effective-mass theory for intralayer screening in graphite intercalation compounds," *Phys. Rev. B*, vol. 29, no. 4, p. 1685, 1984.

[88] T. Ando, T. Nakanishi, and R. Saito, "Berry's phase and absence of back scattering in carbon nanotubes," *J. Phys. Soc. Japan*, vol. 67, no. 8, pp. 2857–28621998, 1998.

[89] P. L. McEuen, M. Bockrath, D. H. Cobden, Y. G. Yoon, and S. G. Louie, "Disorder, pseudospins, and backscattering in carbon nanotubes," *Phys. Rev. Lett.*, vol. 83, no. 24, p. 5098, 1999.

[90] A. Gómez-León and G. Platero, "Floquet-Bloch theory and topology in periodically driven lattices," *Phys. Rev. Lett.*, vol. 110, no. 20, p. 200403, 2013.

[91] M. V. Fistul and K. B. Efetov, "Electromagnetic-field-induced suppression of transport through n– p junctions in graphene," *Phys. Rev. Lett.*, vol. 98, no. 25, p. 256803, 2007.

[92] J. Wilkie, "Dissipation in media with memory: A master equation in the statistical resonance approximation," *J. Chem. Phys.*, vol. 114, no. 18, pp. 7736–7745, 2001.

[93] S. A. Alfadhli, S. E. Savel'ev, and F. V. Kusmartsev, "Dirac-Weyl points' manipulation using linear polarised laser field in Floquet crystals for various Graphene superlattices," *J. Phys. Conf. Ser.*, vol. 961, no. 1, p. 012012, 2018.

[94] Y. Zhang *et al.*, "Landau-level splitting in graphene in high magnetic fields," *Phys. Rev. Lett.*, vol. 96, no. 13, p. 136806, 2006.

[95] D. V. Khveshchenko, "Ghost excitonic insulator transition in layered graphite," *Phys. Rev. Lett.*, vol. 87, no. 24, p. 246802, 2001.

[96] B. S. Kandemir and A. Mogulkoc, "Chiral symmetry breaking by a magnetic field in graphene," *Phys. Lett. A*, vol. 379, no. 36, pp. 2120–2124, 2015.

[97] S. Krukowski, J. Sołtys, J. Borysiuk, and J. Piechota, "Influence of a parallel electric field on the dispersion relation of graphene–A new route to Dirac logics.," *J. Cryst. Growth*, vol. 401, pp. 869–873, 2014.

Appendices

1. Dirac cones in the energy spectrum of SLG in SPM and LPL with different frequencies

ω	A	B	C
0.1		$k_x = 0.45$	$k_x = 0.55$
0.3		$k_x = 0.35$	$k_x = 0.65$
0.5		$k_x = 0.25$	$k_x = 0.75$
0.7		$k_x = 0.15$	$k_x = 0.85$

0.9		
		$k_x = 0.05$	$k_x = 0.95$
1		
		$k_x = 0$	$k_x = 1$
1.3		
		$k_x = 0.15$	$k_x = 1.15$
1.5		
		$k_x = 0.25$	$k_x = 1.25$
1.7		
		$k_x = 0.35$	$k_x = 1.35$

1.9		$k_x = 0.45$	$k_x = 1.45$
2		$k_x = 0.5$	$k_x = 1.5$
2.3		$k_x = 0.65$	$k_x = 1.65$
2.5		$k_x = 0.75$	$k_x = 1.75$
2.7		$k_x = 0.85$	$k_x = 1.85$

2. Dirac cones in the energy spectrum of SLG in SPM and LPL with different amplitudes

A_0	A	B	C
0.1			$k_x = 0.87$
0.3		No Zero energy	$k_x = 0.88$
0.5			$k_x = 0.9$
0.7			$k_x = 0.935$

0.9		 $k_x = 0.975$
1		 $k_x = 0$
		 $k_x = 1$
1.1		 $k_x = 0.23$
		 $k_x = 1.025$

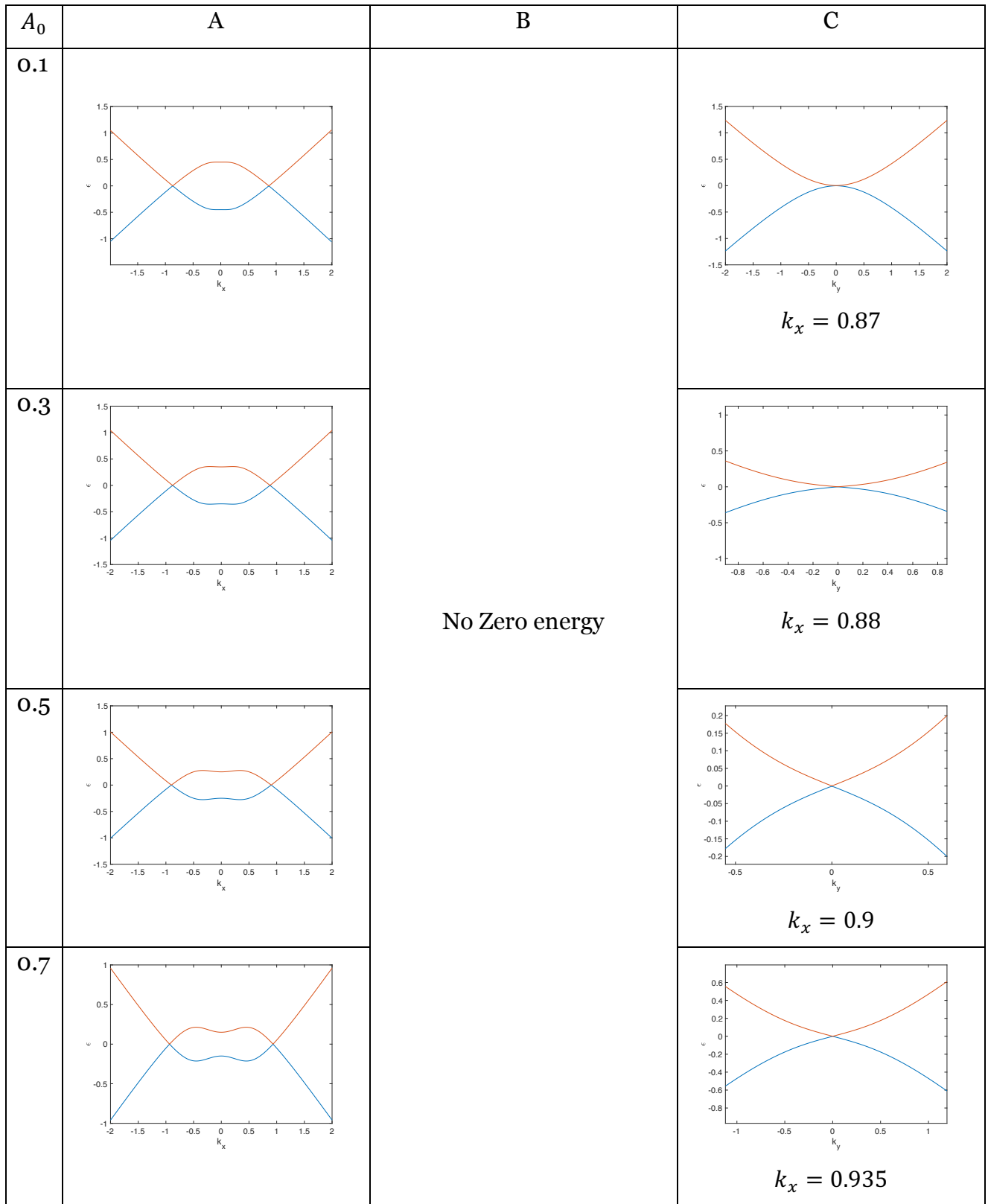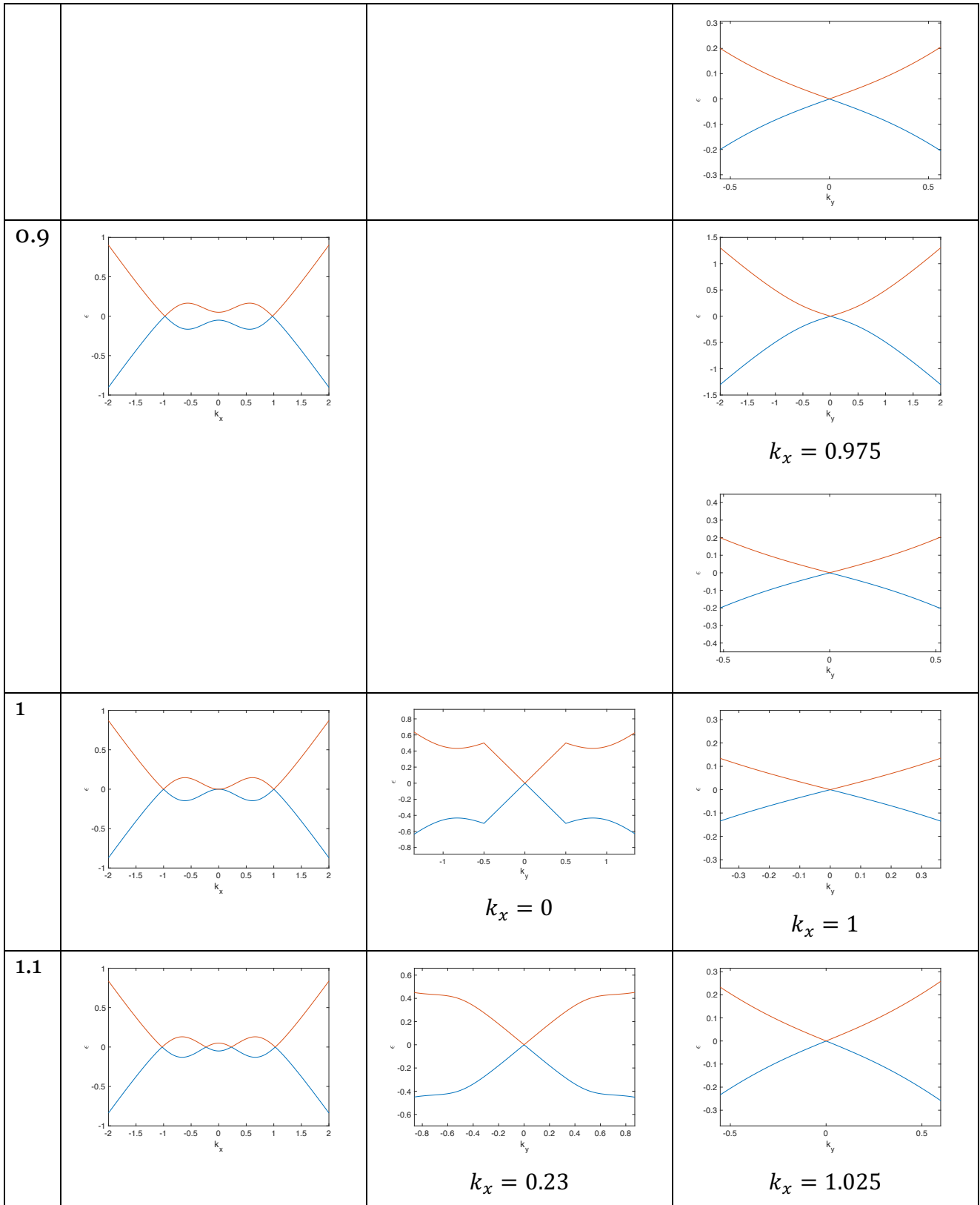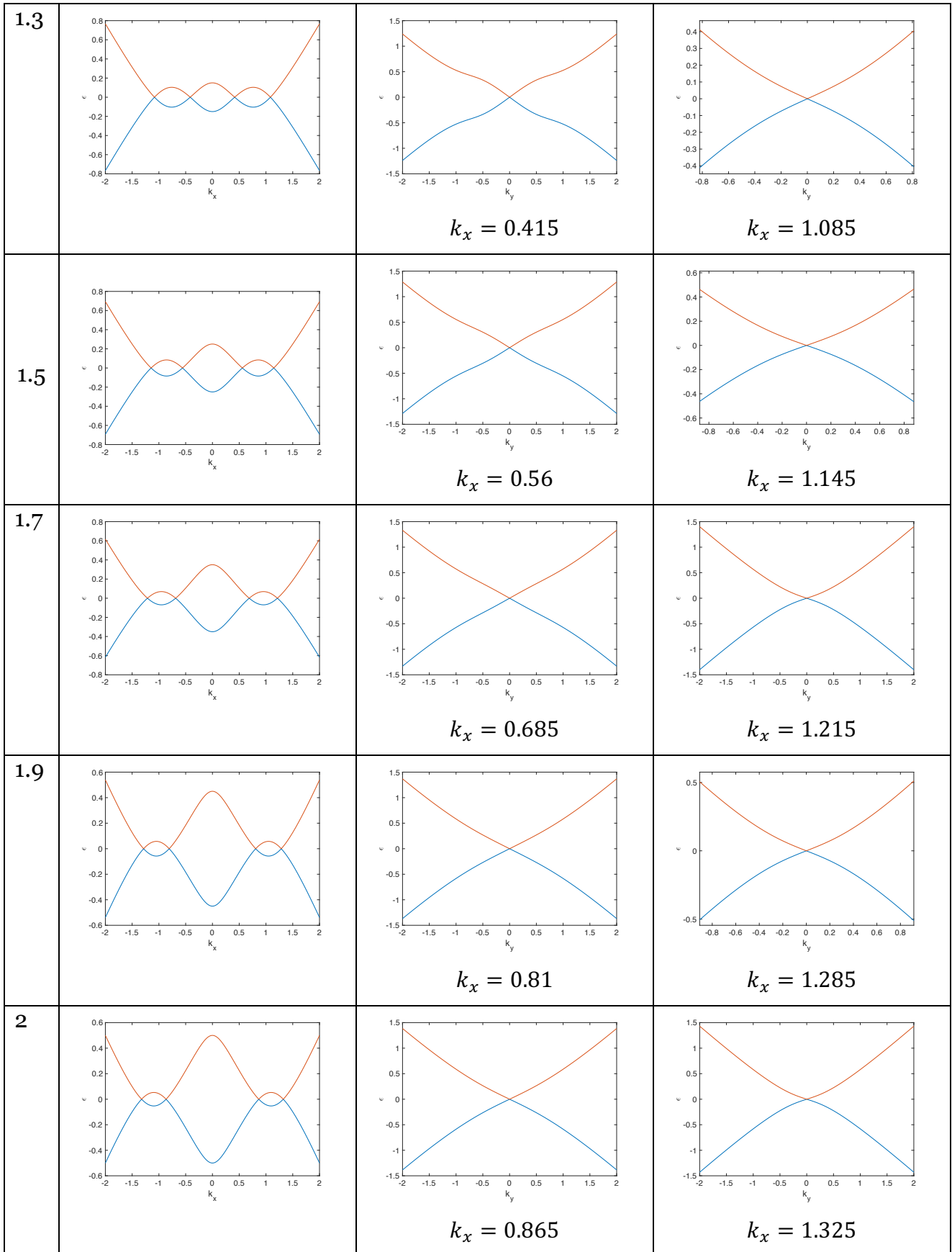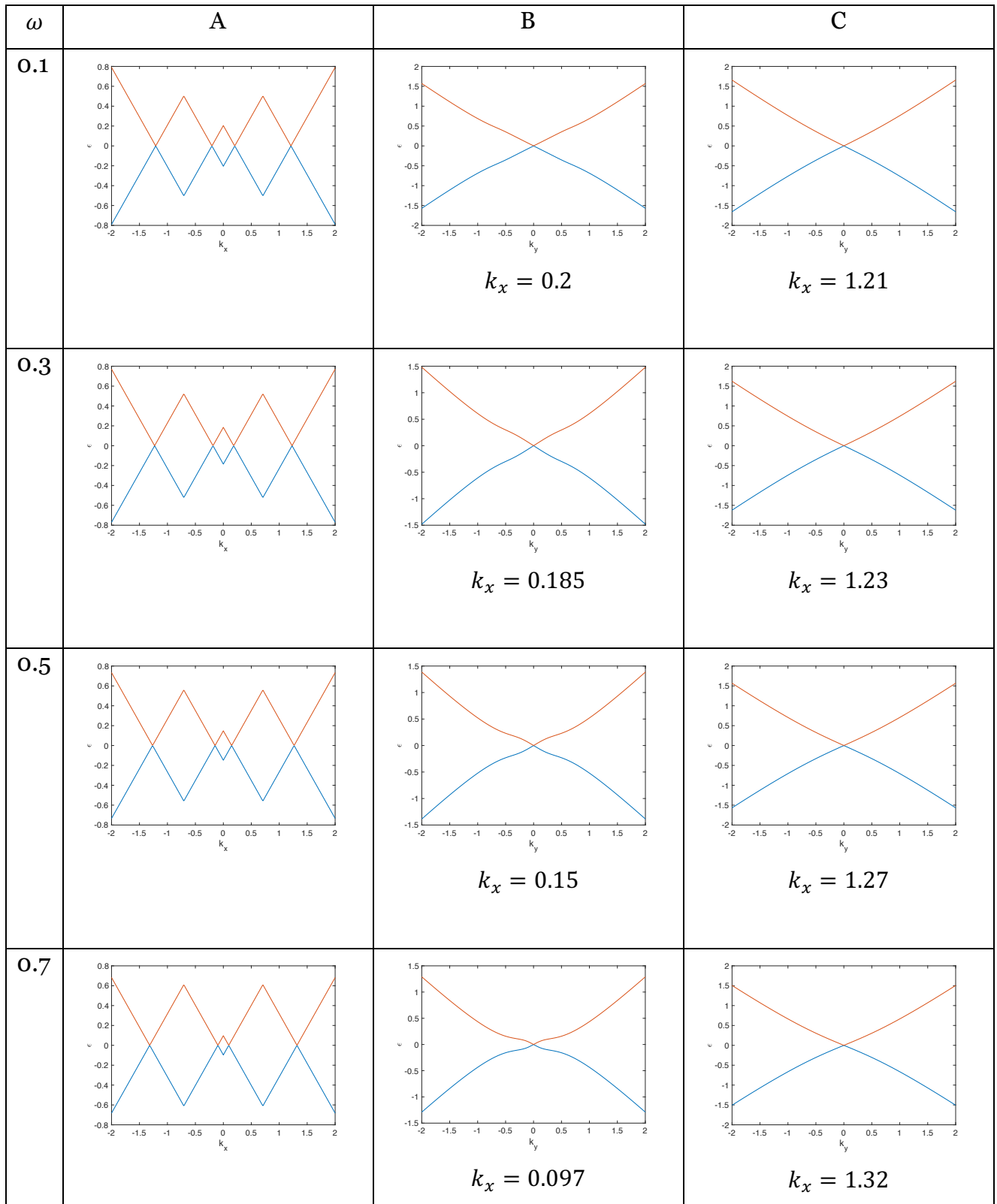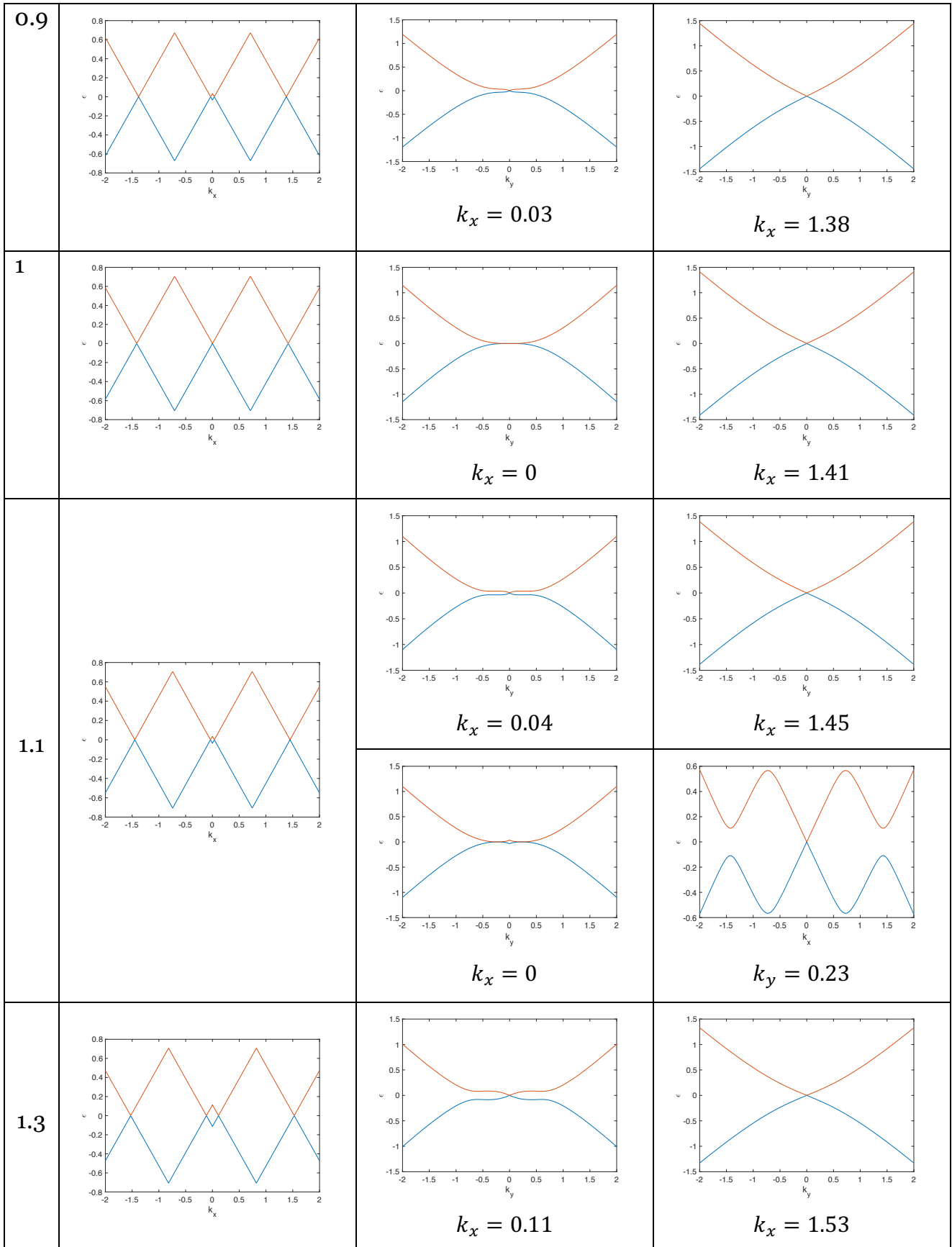| 1.3		$k_x = 0.415$	$k_x = 1.085$
1.5		$k_x = 0.56$	$k_x = 1.145$
1.7		$k_x = 0.685$	$k_x = 1.215$
1.9		$k_x = 0.81$	$k_x = 1.285$
2		$k_x = 0.865$	$k_x = 1.325$

3. Dirac cones in the energy spectrum of SLG in SPE and LPL with different frequencies

ω	A	B	C
0.1		 $k_x = 0.2$	 $k_x = 1.21$
0.3		 $k_x = 0.185$	 $k_x = 1.23$
0.5		 $k_x = 0.15$	 $k_x = 1.27$
0.7		 $k_x = 0.097$	 $k_x = 1.32$

0.9		$k_x = 0.03$	$k_x = 1.38$
1		$k_x = 0$	$k_x = 1.41$

1.1		$k_x = 0.04$
		  $k_x = 0$
			$k_x = 1.45$
			  $k_y = 0.23$

1.3		$k_x = 0.11$	$k_x = 1.53$

		$k_x = 0$	$k_y = 0.415$
1.5		$k_x = 0.19$	$k_x = 1.61$
		$k_x = 0$	$k_y = 0.56$
1.7		$k_x = 0.28$	$k_x = 1.69$
		$k_x = 0$	$k_y = 0.69$

119

<table>
<tr>
<td>1.9</td>
<td></td>
<td>
$k_x = 0.37$</td>
<td>
$k_x = 1.78$</td>
</tr>
<tr>
<td></td>
<td></td>
<td>
$k_x = 0$</td>
<td>
$k_y = 0.81$</td>
</tr>
<tr>
<td>2</td>
<td></td>
<td>
$k_x = 0.41$</td>
<td>
$k_x = 1.825$</td>
</tr>
<tr>
<td></td>
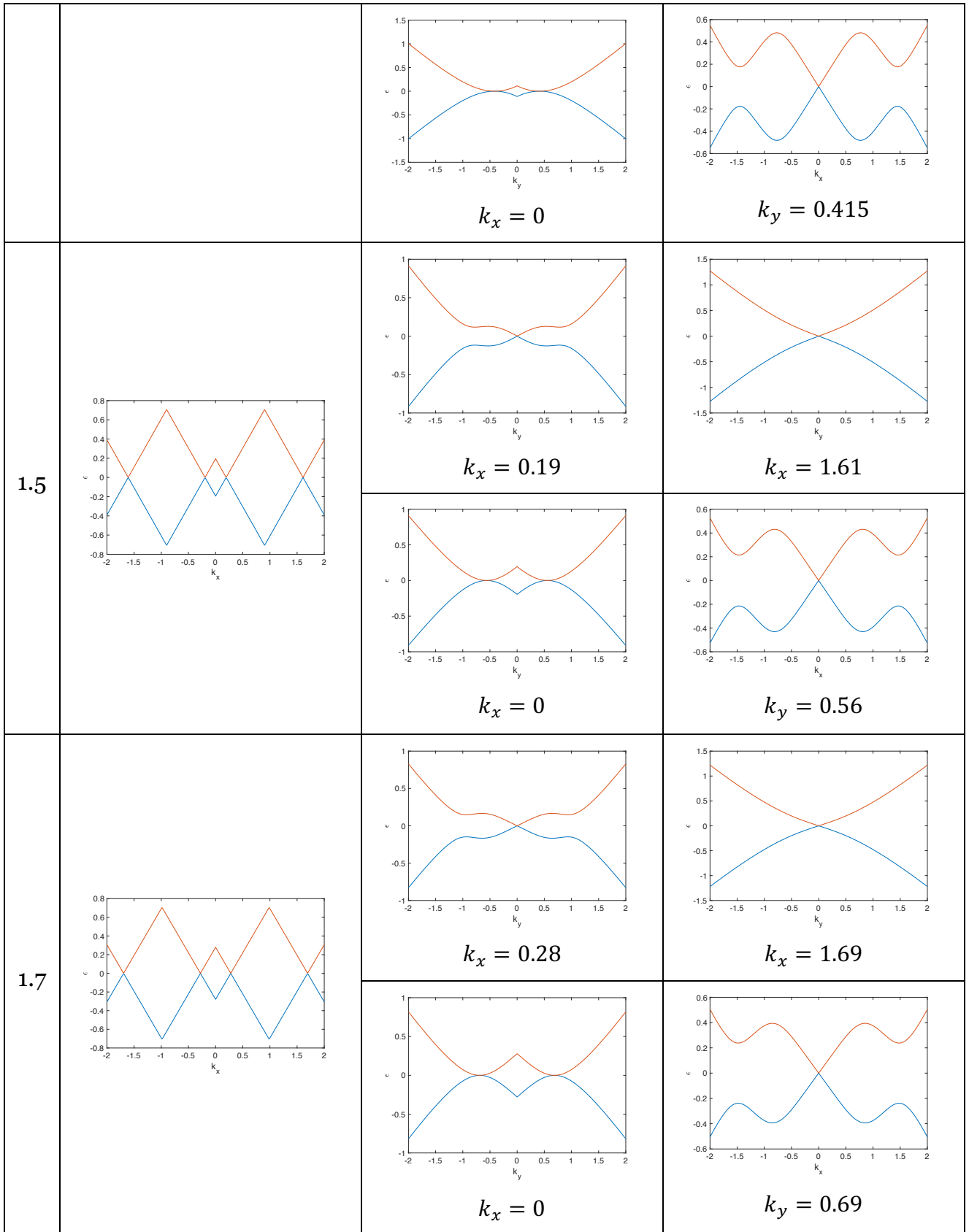<td></td>
<td>
$k_x = 0$</td>
<td>
$k_y = 0.87$</td>
</tr>
</table>

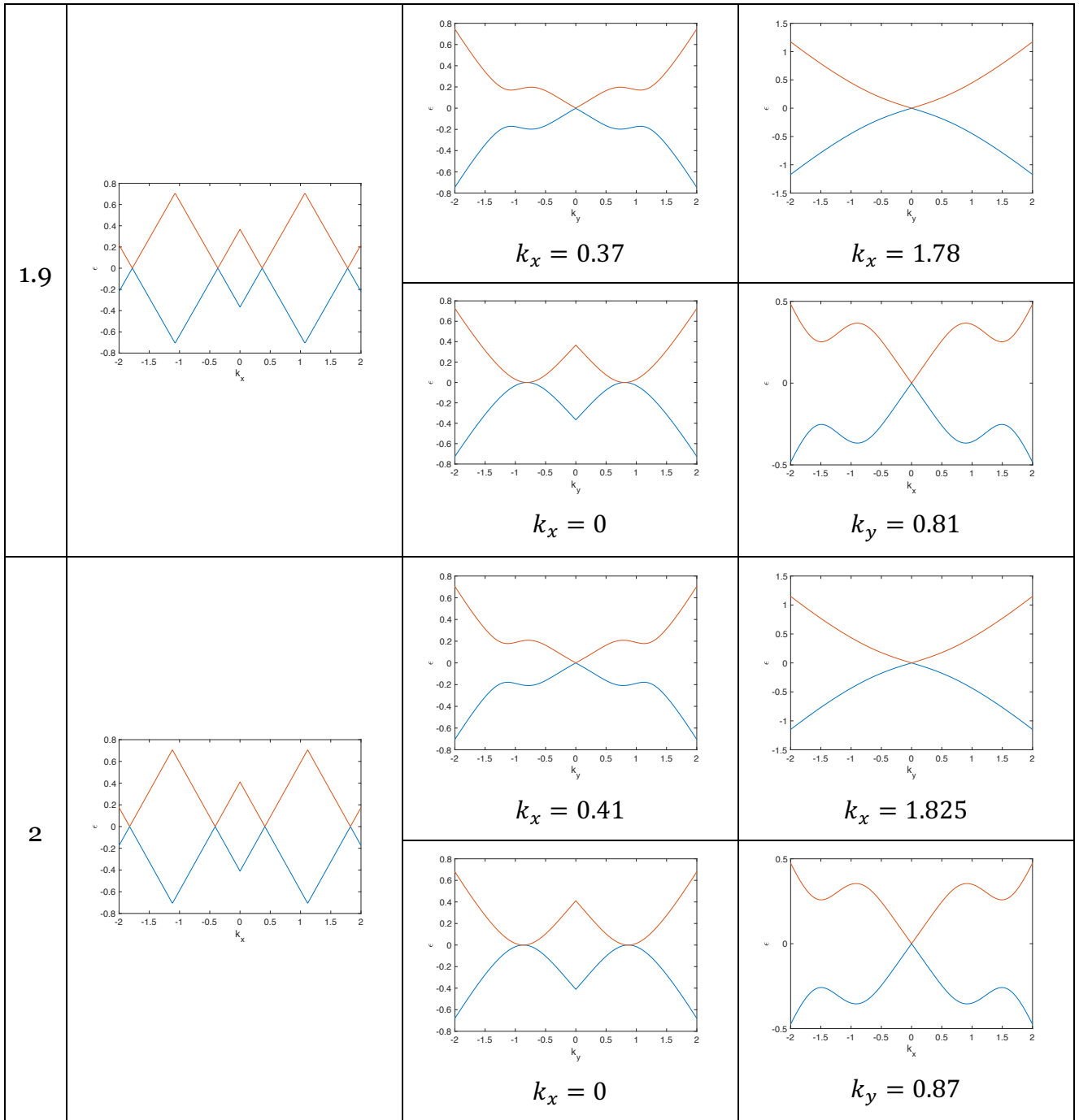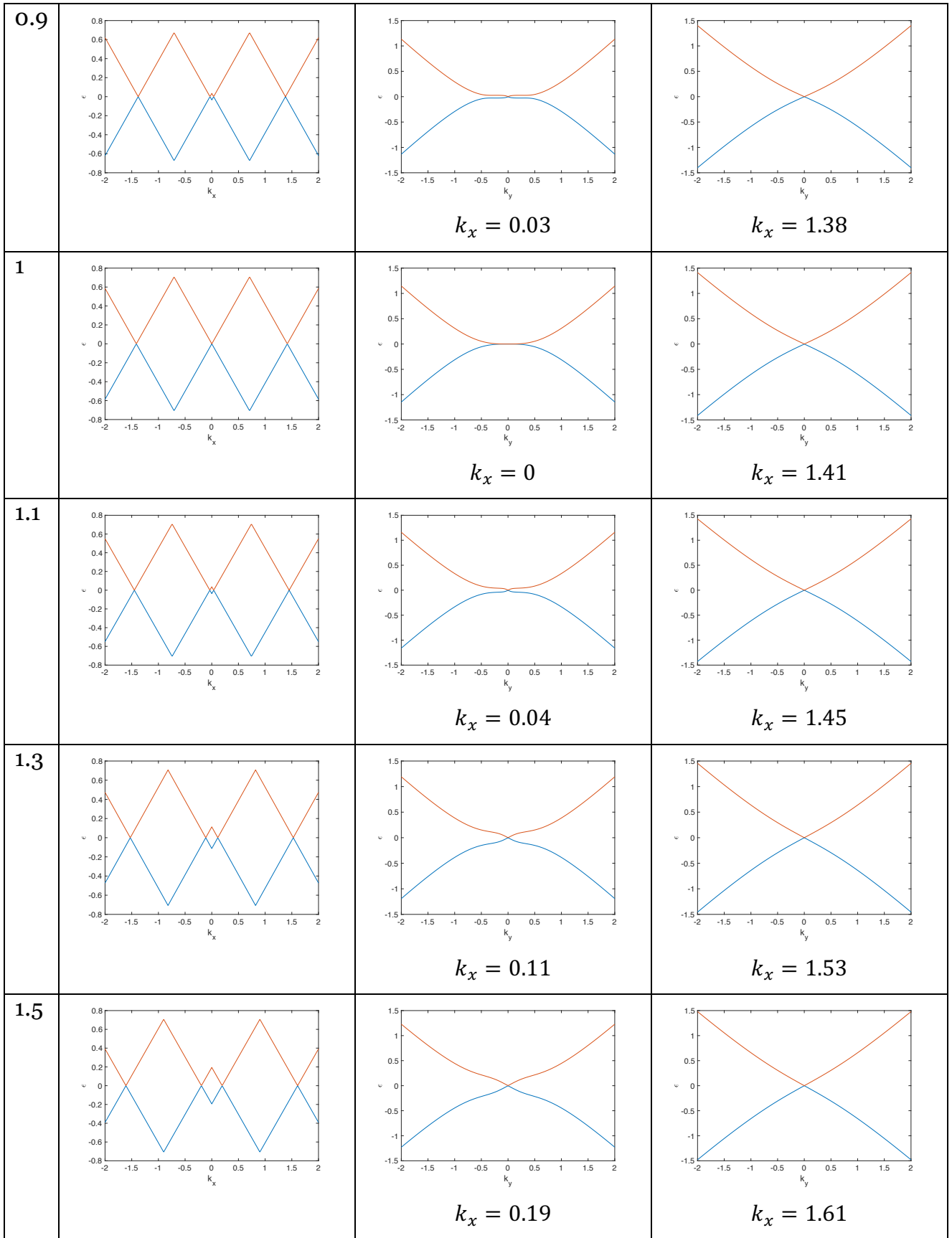4. Dirac cones in the energy spectrum of SLG in SPE and LPL with different amplitudes

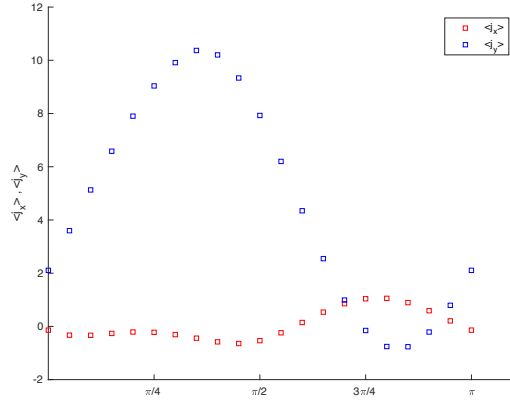| A_0	A	B	C
0.1		$k_x = 0.2$	$k_x = 1.21$
0.3		$k_x = 0.185$	$k_x = 1.23$
0.5		$k_x = 0.15$	$k_x = 1.27$
0.7		$k_x = 0.097$	$k_x = 1.32$

0.9		$k_x = 0.03$	$k_x = 1.38$
1		$k_x = 0$	$k_x = 1.41$
1.1		$k_x = 0.04$	$k_x = 1.45$
1.3		$k_x = 0.11$	$k_x = 1.53$
1.5		$k_x = 0.19$	$k_x = 1.61$

122

1.7		$k_x = 0.28$	$k_x = 1.69$
1.9		$k_x = 0.37$	$k_x = 1.78$
2		$k_x = 0.41$	$k_x = 1.825$

5. The mean current $< j_{x,y} >$ calculated for (a) an applied static electric field ($U_0 = 1, \mu = 1$) with the application of linearly polarised laser field at incident angles θ ($\omega = 1, \& A_0 = 1$) and the current is shown to be periodic asymmetric with no common peaks between j_x and j_y. (b) The mean current $< j_{x,y} >$ calculated for an applied static magnetic field ($A_0^H = 1 \& \mu_H = 1$) with the application of linearly polarised laser field at incident angles θ ($\omega = 1 \& A_0 = 1$). The current is shown to be asymmetric with peaks at $\alpha = \frac{\pi}{4}, \frac{3\pi}{4}$. The current is looks to be a direct current with peaks at $\frac{\pi}{4}, \frac{\pi}{2} \& \frac{3\pi}{4}$. The red curve represents j_x and the blue is j_y. The single particle currents are asymmetric.

Laser	Linear	Parameters
Static Electric	(a) no common peaks	$k_x = 1$, $k_y = 1$ $\theta = 0 \rightarrow \pi$ $\omega = 1$, $\mu = 1$ $A_0 = 1$
Static Magnetic	(b) peaks: $\frac{\pi}{4}, \frac{3\pi}{4}$	$\frac{U_0}{A_0^H} = 1$